

DISSERTATION

Measurement and Compensation of Betatron Resonances at the CERN PS Booster Synchrotron

ausgeführt zum Zwecke der Erlangung des akademischen Grades eines
Doktors der technischen Wissenschaften unter der Leitung von

Univ. Prof. Dr. H. Aiginger
E141
Atominstitut der Österreichischen Universitäten

durchgeführt am
Europäischen Kernforschungszentrum CERN
CH-1211 Genf 23

eingereicht an der Technischen Universität Wien
Fakultät für Physik

von
Dipl.Ing. Peter Urschütz
9425992
A-1230 Wien, Zangerlestraße 18

Diese Arbeit wurde unterstützt vom Österreichischen Bundesministerium
für Bildung, Wissenschaft und Kultur.

Wien, im September 2004



Kurzfassung

Das CERN PS Booster Synchrotron ist der erste Kreisbeschleuniger in der Proton-Injektorkette des zukünftigen Large Hadron Colliders und verbindet den Linearbeschleuniger, Linac2, mit dem Proton Synchrotron. Der PS Booster dient einerseits als Vorbeschleuniger für den LHC und liefert andererseits Teilchenstrahlen mit hoher Intensität und Dichte an die ISOLDE Physikeinrichtungen, sowie an das Proton Synchrotron und dessen Experimentierzonen.

Der vom Linac2 kommende 50 MeV Protonenstrahl wird mittels einer mehrere Umläufe dauernden Injektion in den PS Booster eingespeist. Während der Injektion, des RF-Einfangvorganges und der frühen Beschleunigungsphase erfahren die einzelnen Teilchen im Strahl eine raumladungsbedingte Tune-Verschiebung, infolgedessen ein großer Bereich des "Tunedigramms" abgedeckt ist. Die Protonen verspüren daher die Wirkung zahlreicher Betatronresonanzen, die eine Vergrößerung der Schwingungsamplitude der Teilchen und in letzter Konsequenz Teilchenverluste, zur Folge hat. Um dies zu verhindern, ist eine effiziente Resonanzkompensation erforderlich. Das derzeit verwendete Kompensationsschema wurde vor rund 25 Jahren durch eine orthogonale Suche nach den die Strahlverluste minimierenden Magnetströmen, erstellt.

Die ständig steigende Nachfrage an Hochintensitätsstrahlen, machte eine Überprüfung des existierenden Kompensationsschemas und eine eingehende Analyse aller relevanten Betatronresonanzen wünschenswert. Die Kombination von schneller Elektronik, leistungsstarken Rechnern und der Normal Form Technik, ermöglicht heutzutage die Bestimmung von Stärken und Phasen transversaler Resonanzen auf der Basis von Strahlpositionsmessungen über viele aufeinanderfolgende Umläufe ("turn-by-turn").

Die Dissertation beginnt mit einer kurzen Einführung in die allgemeine Beschleunigerphysik, anschliessend wird die zur Analyse von Betatronresonanzen existierende Theorie erläutert. Es folgt die Beschreibung der für den Aufbau eines Meßsystems notwendigen praktischen Aspekte, unter Berücksichtigung der speziellen Betriebsbedingungen des PS Boosters. Diese Analyse diente als Grundlage für die Spezifizierung und den Aufbau des neuen turn-by-turn Meßsystems, das die Verarbeitung der Rohdaten bis hin zur FFT Analyse ermöglicht und somit die Grundlage für alle Messungen darstellt.

Das durchgeführte Meßprogramm gliedert sich im Wesentlichen in zwei Teile. Im Ersten wurden alle für die Standardoperation des PS Boosters relevanten Resonanzen zweiter und dritter Ordnung im Ring 1 vermessen. Die Stärken und Phasen der entsprechenden Resonanzen wurde bestimmt, die Wirkung von Kompensationsmagneten gemessen und mit Simulationen verglichen. Mit Kenntnis der intrinsischen Resonanzstärken, wurden entsprechende Kompensationsströme errechnet, angewandt und mit dem existierenden Kompensationsschema verglichen. Die erhaltenen Meßergebnisse bestätigten einerseits die Qualität des existierenden Kompensationsschemas, sowie andererseits die Stichhaltigkeit und Genauigkeit der neuen Methode.

Im zweiten Teil des Meßprogramms wurde die Effizienz und Leistungsfähigkeit des neuen Meßsystems ausgenutzt, um einen neuen Arbeitspunkt für den PS Booster zu analysieren. Die in diesem neuen Arbeitsbereich durchgeführten Messungen zeigten eine deutlich kleinere inhärente Resonanzanregung. Aufgrund dieser Resultate wurde der PS Booster 2004 mit dem neuen Arbeitspunkt gestartet und ein neues Kompensationsschema für diesen Arbeitspunkt entwickelt.

Acknowledgement

First I would like to express my entire and sincere thank to my parents, my family, my girlfriend and my friends for their support and encouragement throughout the whole PhD time.

I would like to thank my university supervisor Prof. H. Aiginger from the Atominstitut der Österreichischen Universitäten and my CERN supervisor, Dr. M. Benedikt of the AB Department for their help and commitment shown during the last three years. I am pleased to have the opportunity to also thank C. Carli, M. Chanel, K. Schindl, F. Schmidt and R. Tomás for numerous stimulating and interesting discussions. I am grateful for the help of M. E. Angoletta during the installation and configuration of the acquisition system, the assistance of J. Tan concerning modifications of the PSB pick-up electronics and the continuous support of S. Baird and the whole PSB operations crew during the measurement campaign. Furthermore I would like to thank A. Fabich for advices in informatics.

This work was performed within the Austrian Doctoral Student Programme at CERN, instituted and financed by the Austrian Federal Ministry for Education, Science and Culture.

Contents

1	Introduction	1
2	Basic Accelerator Physics	3
2.1	Coordinate system	3
2.2	Accelerator magnets	3
2.3	Transverse optics	6
2.4	Transfer matrix formalism	9
2.5	Off-momentum particles and dispersion function	10
3	Theory on imperfections and resonances	13
3.1	General multipole expansion of the magnetic field	13
3.2	Overview on imperfections and resonances	16
3.2.1	Closed-Orbit distortions from dipole kicks	16
3.2.2	Quadrupole perturbations	17
3.2.3	Sextupole perturbations	20
3.3	General numerology of resonances	22
3.3.1	Linear coupling	22
3.4	Taylor maps	23
3.4.1	Representation of a multipole kick with Lie operators	23
3.4.2	Properties of the exponential Lie operator	24
3.4.3	The one turn map	24
3.4.4	Normal Form	26
3.4.5	The non-linear motion and its spectrum	27
3.5	Spectral response to particle distributions	30
4	The CERN PS Booster Synchrotron	33
4.1	General layout of the PS Booster	33
4.2	Operation of the PS Booster	35
4.3	The new acquisition system	38
4.4	Measurement set-up	41
4.5	Basic procedure to determine resonance driving terms	42

4.6	Basic considerations on beam position signals	43
5	Measurement and compensation of second order resonance driving terms	47
5.1	Second order contributions to the Fourier spectra	47
5.2	Linear coupling resonances	48
5.2.1	Measurement of the bare machine excitation	50
5.2.2	Reference measurements	53
5.2.3	Compensation of the linear coupling difference resonance	56
5.2.4	Measurements with different chromaticities	62
5.3	The normal quadrupole resonance $2Q_y = 11$	64
5.3.1	Measurement of the bare machine excitation	65
5.3.2	Reference measurements	67
5.3.3	Compensation of the resonance	68
6	Measurement and compensation of third order resonance driving terms	71
6.1	Third order contributions to the Fourier spectra	71
6.2	The systematic resonance $3Q_y = 16$	73
6.2.1	Measurement of the bare machine excitation	73
6.2.2	Reference measurements	77
6.2.3	Compensation of the resonance	78
6.3	Third order coupling resonance driving terms	81
6.3.1	Difference coupling resonance $2Q_x - Q_y = 3$	81
6.3.2	Sum coupling resonance $2Q_x + Q_y = 14$	85
6.3.3	Sum coupling resonance $Q_x + 2Q_y = 15$	89
7	Alternative working point for the PS Booster	93
7.1	Linear coupling	95
7.2	Second order resonance $2Q_y = 9$	97
7.2.1	Measurement of the bare machine excitation	97
7.2.2	Compensation of the resonance	98
7.3	Third order resonance $3Q_y = 13$	102
7.3.1	Measurement of the bare machine excitation	102
7.3.2	Compensation of the resonance	103
7.4	Conclusions for the new working point	103
8	Conclusions	104
	Bibliography	106

Notation

LHC	Large Hadron Collider
Linac	Linear accelerator
PS	Proton Synchrotron
PSB	PS Booster
PU	Pick-Up
FFT	Fast Fourier Transformation
SUSSIX	Code for Frequency Analysis of Non-Linear Betatron Motion
SixTrack	Single Particle Tracking Code
x, y	transverse coordinates
s	longitudinal coordinate
z	represents x or y
X, Y	normalised transverse coordinates
Z	represents X or Y
ρ	local radius of curvature
p	particle momentum or azimuthal harmonic in the multipole error distribution
δ	momentum deviation
B	brightness
Q_x, Q_y	transverse tunes
q_x, q_y	non-integer part of the transverse tunes Q_x, Q_y
Q_s	synchrotron tune
ν_x, ν_y	transverse tunes including amplitude detuning
$Q'_{x,y}$	chromaticity
$\nu'_{xx}, \nu'_{xy}, \nu'_{yy}$	amplitude detuning coefficients
f_{rev}	revolution frequency
T_{ref}	revolution time
$\alpha_{x,y}, \beta_{x,y}, \gamma_{x,y}$	Twiss parameters
$\mu_{x,y}$	betatron phase
$\epsilon_{x,y}$	transverse geometrical emittance
$\epsilon_{n,x,y}$	normalised transverse emittance
$\beta_{rel}, \gamma_{rel}$	relativistic parameters
q	charge of the particle

\vec{v}	particle velocity
\vec{F}	force
\vec{B}	magnetic field
\vec{A}	vector potential
V	scalar potential
B_n, A_n	normal and skew coefficients
A	atomic mass number
$D(s)$	dispersion function
g	quadrupole gradient
k	normalised quadrupole gradient
k_n	n th order normalised gradient
$a_{x0,y0}$	amplitude of the tune line
$a_{x1,y1}$	amplitude of the resonance line
$\psi_{x0,y0}$	phase of the tune line
$\phi_{x1,y1}$	phase of the resonance line
H	Hamiltonian
h	non-linear Hamiltonian
h_{jklm}	Hamiltonian terms
F	generating function
f_{jklm}	generating function terms
J, ϕ	action-angle variables
I, ψ	action-angle variables in Normal Form basis
M	linear map
$M(s)$	linear one-turn map
\mathcal{M}	total one-turn map
R	linear one-turn map expressed as rotation
$h_{x,y}^{\pm}$	linearly normalised basis
$\zeta_{x,y}^{\pm}$	Normal Form basis
$e^{\cdot f}$	Lie operator with f as generating function

Chapter 1

Introduction

The CERN PS Booster Synchrotron is the first circular accelerator in the proton injector chain of the future Large Hadron Collider and links the linear accelerator, Linac2, with the Proton Synchrotron. Apart from serving as a pre-injector for the LHC, the PS Booster provides high intensity beams for the ISOLDE physics facility and various other beams for the Proton Synchrotron and its users.

The 50 MeV proton beam coming from Linac2 is accumulated in the PS Booster by means of a multi-turn-injection scheme. Throughout injection, rf-capture and early acceleration, the individual particles in the beam “see” large, fluctuating incoherent space-charge tune shifts, consequently sweeping a large area in the tune diagram and covering various resonances. Thus, the beam suffers amplitude blow-up from transverse betatron resonances and efficient compensation is required to avoid subsequent particle losses. The presently used resonance compensation scheme was established 25 years ago by orthogonal search of coupled magnet currents minimising beam losses.

With the increasing demands for higher intensities and higher brightness beams, a revision of the existing working point with a general analysis of all relevant betatron resonances was proposed for the thesis. The combination of fast electronics, powerful computing tools and Normal Form techniques now make it possible to evaluate amplitude and phase of resonance driving terms from turn-by-turn beam position measurements.

The specific goals of the thesis were:

- Defining an acquisition system for beam position measurement over many turns with storage and analysis.
- Implementation of the system as a tool for machine operation on the PS Booster.
- Measurement of resonance excitation and comparison to simulations.
- Verification and potential improvement of the existing compensation scheme.
- Search for an alternative new working point with lower intrinsic excitation and efficient compensation.

The measurement programme implemented in the thesis favoured the choice of a new working point for the PS Booster and culminated in a complete evaluation of the amplitude and phase of driving terms for all the resonances relevant to operation.

Chapter 2

Basic Accelerator Physics

The guiding and focusing of a charged particle beam in a circular accelerator rely on a series of magnetic elements, separated by field-free drift spaces, that form the accelerator lattice. The basic structure, consisting of dipole and quadrupole magnets, is referred to as the *linear lattice* and once it is determined by the accelerator designer the character of the machine is more or less fixed. In a separated function synchrotron, dipoles bend the particles onto circular trajectories and quadrupoles are needed for the focusing of particles with small deviations from the ideal trajectory. The *equilibrium orbit* itself can be defined as the orbit of a particle with the design momentum p_0 that closes upon itself after one turn and is stable. The motion of a particle in an accelerator is then conveniently described by the deviations of its trajectory with respect to this equilibrium orbit.

2.1 Coordinate system

In a synchrotron generally bending is foreseen in only one plane referred to as the horizontal plane which contains the equilibrium orbit. For the description of the particle motion a right handed curvilinear coordinate system (x, s, y) following the equilibrium orbit is used. The azimuthal coordinate s is directed along the tangent of the orbit. The radial transverse direction x is defined as normal to the orbit in the horizontal plane and the vertical transverse direction y is given by the cross product of the unit vectors \hat{x} and \hat{s} . The local radius of curvature ρ_0 and the bending angle s/ρ_0 are defined as positive for anticlockwise rotation when viewed from positive y . The coordinate system is shown in Fig. 2.1.

2.2 Accelerator magnets

For this study, the magnetic elements are considered as purely transverse, two-dimensional fields in the curvilinear coordinate system. The force experienced by a particle moving in a magnetic field is given by,

$$\vec{F} = \frac{d\vec{p}}{dt} = q \cdot \vec{v} \times \vec{B}, \quad (2.1)$$

where \vec{v} is the particle velocity, q the charge and \vec{B} the magnetic field. Since the Lorentz force always acts perpendicular to the particle velocity, only the direction of movement changes

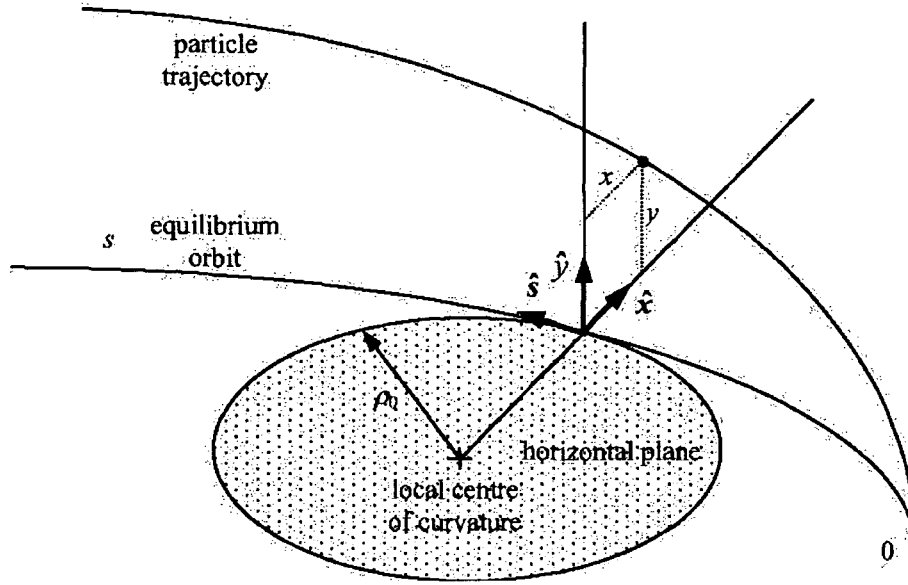


Figure 2.1: Curvilinear coordinate system.

while the magnitude of the velocity stays constant. The equilibrium orbit in a circular accelerator is defined by the main bending magnets which provide a dipolar field,

$$\vec{B} = B_0 \hat{y}. \quad (2.2)$$

Equating the magnetic deflection to the centrifugal force gives,

$$-nevB_0 = \frac{Am_{av}v^2}{\rho_0}, \quad (2.3)$$

where A is the atomic mass number, m_{av} is the average relativistic mass per nucleon, n is the charge state of the particle, e is the elementary charge and ρ_0 is the bending radius. Rearranging gives,

$$-B_0\rho_0 = \frac{A m_{av}v}{n e} = \frac{p_0}{q}. \quad (2.4)$$

This leads directly to the widely used numerical expression which relates the radius of gyration to the momentum,

$$|B[\text{T}]\rho[\text{m}]| \approx 3.3356 \frac{A}{n} p_{av}[\text{Gev}/c], \quad (2.5)$$

where p_{av} is the average momentum per nucleon. The quantity $|B\rho|$ is called *magnetic rigidity* and is a measure for the resistance of the particle to be bend. From Eq. 2.5 it can be seen that the higher the particle momentum, the higher the magnetic field needed to keep the particle on the nominal orbit. Therefore, the magnetic fields in an accelerator have to be continuously adjusted, according to the actual particle momentum during acceleration. In order to avoid the momentum dependency when characterising magnetic elements in an accelerator, the fields are

normalised with respect to the magnetic rigidity of the design particle (particle momentum). For a dipole magnet the normalised strength h is given by,

$$h = \frac{1}{\rho_0}. \quad (2.6)$$

The equilibrium orbit in a synchrotron is defined by the main dipole magnets. In general particle trajectories will deviate slightly from this ideal design orbit. To maintain stability about the design orbit, focusing forces are needed. These are provided by quadrupole magnets. A quadrupole magnet has four poles with a hyperbolic contour and the magnetic field in the current-free region of the magnet gap can be derived from a scalar potential [2],

$$V(x, y) = -gxy, \quad (2.7)$$

where g is known as the quadrupole gradient, being defined as,

$$g = \left[\frac{dB_y}{dx} \right]_0. \quad (2.8)$$

The equipotential lines are the hyperbola $xy = \text{const}$ and the field lines are perpendicular to them. The horizontal and vertical magnetic fields in a quadrupole magnet are linear in the deviation from the magnet centre:

$$B_x = gy, \quad B_y = gx. \quad (2.9)$$

The transverse forces acting on the particle with a deviation (x, y) from the equilibrium orbit are obtained with Eq. 2.1 as,

$$\begin{aligned} F_x &= qvB_y(x, y) = qv gx, \\ F_y &= -qvB_x(x, y) = -qv gy. \end{aligned} \quad (2.10)$$

Depending on the sign of g , the force will be focusing in the horizontal direction and defocusing in the vertical direction or vice versa. A quadrupole that focuses horizontally is called *focusing quadrupole* and a quadrupole that defocuses horizontally is called *defocusing quadrupole*. By alternating focusing and defocusing quadrupoles an overall focusing effect can be obtained in both the horizontal and vertical planes (alternating gradient focusing).

An important property of a quadrupole magnet is that the horizontal force depends only on the horizontal position of the particle trajectory. Similarly, the vertical component of the Lorentz force depends only on the vertical position. The important consequence is that in a *linear machine*, containing only dipolar and quadrupolar fields, the horizontal and vertical motions are completely *decoupled*.

In analogy to the normalised bending strength of a dipole magnet (2.6), the quadrupole gradient can be normalised w.r.t. the magnetic rigidity, thus defining the normalised quadrupolar strength,

$$k = -\frac{g}{B_0 \rho_0}. \quad (2.11)$$

If l denotes the length of the quadrupole, its focal length f is given by,

$$\frac{1}{f} = kl. \quad (2.12)$$

In general, a lens with $f \gg l$ is referred to as a *thin lens* [2].

2.3 Transverse optics

When analysing the transverse motion in an accelerator, it is practical to use the distance s measured along the trajectory, instead of the time as independent variable:

$$\frac{d}{dt} = \frac{d}{ds} \frac{ds}{dt} = v \frac{d}{ds}. \quad (2.13)$$

It is usual to consider only dipole and quadrupole fields (linear lattice), which give the uncoupled motions in the two transverse planes. The equations of motion are obtained from Eq. 2.1 and have the following form under consideration of just small deviations from the reference orbit:

$$\frac{d^2x}{ds^2} - \left(k(s) - \frac{1}{\rho_0(s)^2} \right) x = 0, \quad (2.14)$$

$$\frac{d^2y}{ds^2} + k(s)y = 0, \quad (2.15)$$

where $k(s)$ is the normalised field gradient and $\rho_0(s)$ is the local curvature of the reference orbit at the position s . The term $\frac{1}{\rho_0^2}$ describes the “weak focusing” of a bending magnet and the term $k(s)$ the “strong focusing” of a quadrupole [2]. Eqs. 2.14 and 2.15 are the so called *Hill's equations* and can be written in the form

$$\frac{d^2z}{ds^2} + K_z(s)z = 0, \quad (2.16)$$

where z stands for either x or y and $K_z(s)$ represents the horizontal or vertical focusing forces. The focusing function $K_z(s)$ is piecewise constant along the orbit and has for a circular machine the periodicity of the lattice

$$K_z(s + L) = K_z(s), \quad (2.17)$$

where the accelerator is composed of N identical sections or cells, with $C = N \cdot L$ and C being the circumference of the machine.

The motion of mono-energetic particles about their equilibrium orbit is known as the *betatron motion*. The solution of Eq. 2.16 is written in a pseudo-harmonic oscillator form introduced by Courant and Snyder [3],

$$z(s) = \sqrt{\epsilon_z \beta_z(s)} \cos(\mu_z(s) + \phi_z), \quad (2.18)$$

where ϵ_z and ϕ_z are constants given by the initial conditions of the particle, $\beta_z(s)$ is the *betatron function* (dimension length) and $\mu_z(s)$ the phase of the pseudo oscillation given as,

$$\mu_z(s) = \int_0^s \frac{d\sigma}{\beta_z(\sigma)}. \quad (2.19)$$

To complete the description, the derivative of $\beta_z(s)$ is added in the relations,

$$\alpha_z(s) = -\frac{1}{2} \frac{d\beta_z(s)}{ds} \quad (2.20)$$

and

$$\gamma_z(s) = \frac{1 + \alpha_z(s)^2}{\beta_z(s)}. \quad (2.21)$$

The expressions Eqs. 2.18 - 2.21 depend on the knowledge of $\beta_z(s)$. Although the analytic solution for $\beta(s)$ is more complicated than the original equations of motion, it is reasonably easy to evaluate this function numerically and to tabulate it for any lattice. The parameters $\alpha(s)$, $\beta(s)$ and $\gamma(s)$ are collectively known as the *Courant and Snyder parameters* or as *Twiss parameters*. The above parameterisation is now so commonplace that it is the starting point for nearly all lattice design.

A further very important machine parameter is the *tune* Q_z . It is defined by the number of betatron oscillations in one revolution and is expressed as,

$$Q_z = \frac{1}{2\pi} \int_s^{s+C} \frac{d\sigma}{\beta_z(\sigma)}. \quad (2.22)$$

The pseudo-harmonic motion (Eq. 2.18) can be further transformed into a simple harmonic motion by differentiating, to obtain

$$z'(s) = -\sqrt{\epsilon_z} \frac{\alpha_z}{\sqrt{\beta_z}} \cos(\mu_z + \phi_z) - \sqrt{\epsilon_z} \frac{1}{\sqrt{\beta_z}} \sin(\mu_z + \phi_z). \quad (2.23)$$

The phase terms of Eqs. 2.18 and 2.23 can be extracted and used to define so called *normalised coordinates* $Z(\mu)$ and $Z'(\mu)$ as,

$$Z(\mu) = \sqrt{\epsilon_z} \cos(\mu_z + \phi_z) = z(s) \frac{1}{\sqrt{\beta_z}}, \quad (2.24)$$

$$Z'(\mu) = -\sqrt{\epsilon_z} \sin(\mu_z + \phi_z) = z'(s) \sqrt{\beta_z} + z(s) \frac{\alpha_z}{\sqrt{\beta_z}}. \quad (2.25)$$

It is useful to represent real-space coordinates by lower case symbols and normalised coordinates by upper case symbols. Normalised coordinates use the phase advance μ as independent variable, real-space coordinates use the distance s . The transformations between the two systems are conveniently expressed in matrix form. The normalised coordinates are obtained from the real coordinates with

$$\begin{pmatrix} Z \\ Z' \end{pmatrix} = \begin{pmatrix} 1/\sqrt{\beta_z} & 0 \\ \alpha_z/\sqrt{\beta_z} & \sqrt{\beta_z} \end{pmatrix} \begin{pmatrix} z \\ z' \end{pmatrix} \quad (2.26)$$

and vice versa the real coordinates from the normalised

$$\begin{pmatrix} z \\ z' \end{pmatrix} = \begin{pmatrix} \sqrt{\beta_z} & 0 \\ -\alpha_z/\sqrt{\beta_z} & 1/\sqrt{\beta_z} \end{pmatrix} \begin{pmatrix} Z \\ Z' \end{pmatrix}. \quad (2.27)$$

The elimination of the phase advance from Eqs. 2.24 and 2.25 yields an invariant of the motion

$$\epsilon_z = Z^2 + Z'^2 = \gamma_z z^2 + 2\alpha_z z z' + \beta_z z'^2 \quad (= \text{constant}). \quad (2.28)$$

Eq. 2.28 is in fact the equation of an ellipse in (z, z') phase space. The constant ϵ_z is referred to as the *emittance* of the beam and is equal to the area of this ellipse divided by π .

The form of the ellipse will vary from point to point in the lattice, but its area will remain unchanged. When referring to a particle beam, the size of the emittance is normally related to a number of standard deviations of the particle distribution. It is worth mentioning that the emittance is equal in real and normalised phase space and can be expressed in terms of the maximum excursions \hat{z} and \hat{Z} in real and normalised phase spaces (Fig. 2.2) that define the beam-size at the observer's position:

$$\epsilon_z = \frac{\hat{z}^2}{\beta_z} = \hat{Z}^2. \quad (2.29)$$

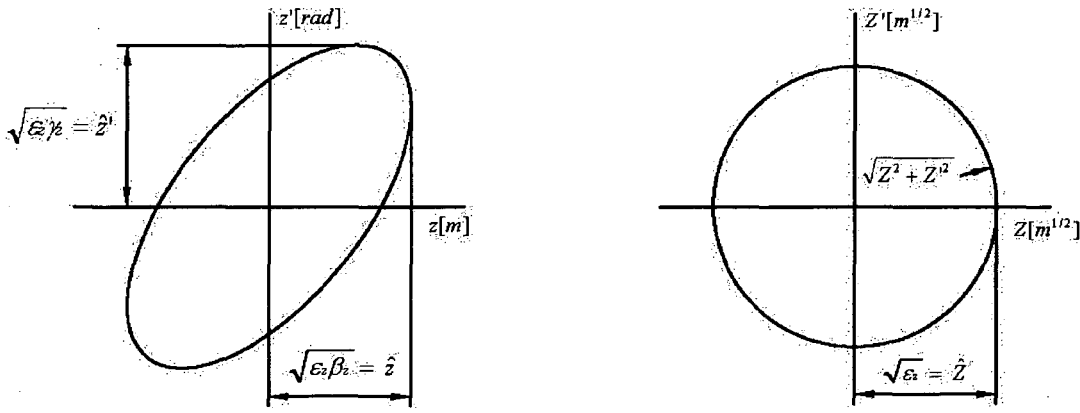


Figure 2.2: Phase space ellipses in real and normalised phase space.

It should be noted that during acceleration the emittance decreases and therefore the phase space density changes. This is not against Liouville's theorem, but due to the definition of the transverse phase space. The z' coordinate describes the divergence of a particle with respect to the nominal orbit

$$z' = \frac{dz}{ds} = \frac{1}{v} \frac{dz}{dt} = \frac{v_z}{v} \quad (2.30)$$

and does not represent the generalised momentum as defined in classical mechanics. As long as the momentum is constant, the difference is just a scaling factor, but during acceleration this factor changes and so does the emittance. This can be understood from the observation that only the longitudinal component of the momentum vector is increased in the accelerating cavities whereas the transverse components remain invariant, so that the divergence shrinks. This phenomenon is known as *adiabatic damping*. Normalising the emittance w. r. t. the particle momentum gives a constant of motion, the so called *normalised emittance* [2],

$$\epsilon_{n,z} = \beta_{rel} \gamma_{rel} \epsilon_z, \quad (2.31)$$

where β_{rel} and γ_{rel} are the relativistic parameters.

2.4 Transfer matrix formalism

To transfer particles from position s_1 to position s_2 in an accelerator it is convenient to use a transfer matrix formalism. The *general transfer matrix* is derived by expanding Eq. 2.18 into two terms

$$z(s) = A\sqrt{\beta_z(s)}\cos(\mu_z(s)) + B\sqrt{\beta_z(s)}\sin(\mu_z(s)) \quad (2.32)$$

and replacing the constants A and B with the initial conditions $s = s_1$ ($\mu_z(s_1) = 0$) [4]. The general transfer matrix from position s_1 to position s_2 is then expressed as,

$$M(s_1 \rightarrow s_2) = \begin{pmatrix} \sqrt{\frac{\beta_2}{\beta_1}}(\cos\Delta\mu + \alpha_1\sin\Delta\mu) & \sqrt{\beta_1\beta_2}\sin\Delta\mu \\ -\frac{1}{\sqrt{\beta_1\beta_2}}[(1 + \alpha_1\alpha_2)\sin\Delta\mu] + (\alpha_2 - \alpha_1)\cos\Delta\mu & \sqrt{\frac{\beta_1}{\beta_2}}(\cos\Delta\mu - \alpha_2\sin\Delta\mu) \end{pmatrix}, \quad (2.33)$$

where $\Delta\mu$ is the phase advance between s_1 and s_2 . The phase space coordinates at position s_2 are then given by the *map*

$$\begin{pmatrix} z_2 \\ z'_2 \end{pmatrix} = M(s_1 \rightarrow s_2) \begin{pmatrix} z_1 \\ z'_1 \end{pmatrix}. \quad (2.34)$$

Since in a circular machine the general focusing forces are periodic, i. e. $K(s) = K(s + L)$, where L is the length of the period (or the whole circumference of the ring), the conditions of periodicity are imposed for β ($\beta_1 = \beta_2$) and α ($\alpha_1 = \alpha_2$), leading to a simplified transfer matrix

$$M(s \rightarrow s + L) = \begin{pmatrix} \cos\mu_0 + \alpha\sin\mu_0 & \beta\sin\mu_0 \\ -\gamma\sin\mu_0 & \cos\mu_0 - \alpha\sin\mu_0 \end{pmatrix}, \quad (2.35)$$

where μ_0 is the phase advance per period.

To complete the presentation of transfer matrices, the general transfer matrix for normalised coordinates, which is simply a 2 times 2 rotation matrix, is given as,

$$M_n(s_1 \rightarrow s_2) = \begin{pmatrix} \cos\Delta\mu & \sin\Delta\mu \\ -\sin\Delta\mu & \cos\Delta\mu \end{pmatrix}. \quad (2.36)$$

The matrix notation of the solution of the equations of motion is particularly useful if the focusing forces $K_z(s)$ are piecewise constant, because the matrix elements can then be expressed analytically. The solution for the complete accelerator lattice is then just the product of the individual matrices in the desired sequence and hence the matrix for one period (Eq. 2.35) is obtained by multiplying all these individual matrices. The transfer matrices of all elements in an accelerator are used as building bricks to assemble the complete lattice. In the following the maps of the most important linear elements are given [2]:

- Drift space:

The simplest element in an accelerator is a field free region or drift space. The linear map that describes a drift space of length L is given by,

$$\begin{pmatrix} z \\ z' \end{pmatrix}_{s+L} = \begin{pmatrix} 1 & L \\ 0 & 1 \end{pmatrix} \cdot \begin{pmatrix} z \\ z' \end{pmatrix}_s. \quad (2.37)$$

- Dipole:

A sector dipole with a constant vertical magnetic field over a length L and edges perpendicular to the central trajectory is represented as,

$$\begin{pmatrix} x \\ x' \end{pmatrix}_{s+L} = \begin{pmatrix} \cos(L/\rho_0) & \rho_0 \sin(L/\rho_0) \\ -(1/\rho_0) \sin(L/\rho_0) & \cos(L/\rho_0) \end{pmatrix} \cdot \begin{pmatrix} x \\ x' \end{pmatrix}_s, \quad (2.38)$$

where x stands for the horizontal plane. Vertically the motion is equivalent to a drift space of length L .

- Quadrupole:

The map for a focusing quadrupole with a normalised quadrupolar strength k and length L can be written as,

$$\begin{pmatrix} z \\ z' \end{pmatrix}_{s+L} = \begin{pmatrix} \cos\psi & (1/\sqrt{|k|}) \sin\psi \\ -\sqrt{|k|} \sin\psi & \cos\psi \end{pmatrix} \cdot \begin{pmatrix} z \\ z' \end{pmatrix}_s, \quad (2.39)$$

where $\psi = L\sqrt{|k|}$. Similarly, a defocusing quadrupole is described as,

$$\begin{pmatrix} z \\ z' \end{pmatrix}_{s+L} = \begin{pmatrix} \cosh\psi & (1/\sqrt{|k|}) \sinh\psi \\ \sqrt{|k|} \sinh\psi & \cosh\psi \end{pmatrix} \cdot \begin{pmatrix} z \\ z' \end{pmatrix}_s. \quad (2.40)$$

For simplicity these expressions are given for a particle with the design momentum p_0 . The advantage of this formalism is that particles can be propagated through sections of several magnets by multiplying 2×2 matrices. The one turn matrix $M(s)$ for a circular accelerator is the transfer matrix that propagates the particle through all the elements back to the starting location. It is constructed by multiplying all the elements in the form

$$M(s_1) = M_N \cdots M_2 M_1, \quad (2.41)$$

where M_i are the matrices of the corresponding linear elements.

2.5 Off-momentum particles and dispersion function

Particles with a momentum p different from the “design” momentum p_0 will not follow the design orbit, i. e. particles with a larger momentum need a circle with a larger radius on which they can move indefinitely. The horizontal equation of motion (2.14) can be expanded by adding a driving term $F(s)$ to obtain

$$\frac{d^2x}{ds^2} - \left(k(s) - \frac{1}{\rho_0(s)^2} \right) x = F(s), \quad (2.42)$$

where $F(s) = (1/\rho_0) \cdot (\delta p/p_0)$. The particle momentum deviation δp is given by $p - p_0$.

The solution of the equation above is then simply an extension of Eq. 2.18, including the solution for the inhomogeneous differential equation

$$x(s) = \sqrt{\epsilon_x \beta_x(s)} \cos(\mu_x(s) + \phi_x) + D(s) \frac{\delta p}{p_0}, \quad (2.43)$$

where $D(s)$ is known as the *dispersion function*. The dispersion is created by the momentum dependency of the bending radius in dipole magnets and appears therefore only in the plane of bending (generally the horizontal plane). The equilibrium orbit for an off-momentum particle is to first order displaced from the central orbit by the product of the dispersion function and the relative momentum deviation. The dispersion function is given as,

$$D(s) = \frac{\sqrt{\beta(s)}}{2s \sin(\pi Q)} \int_s^{s+C} \frac{\sqrt{\beta(\sigma)}}{\rho_0(\sigma)} \cos[\mu(\sigma) - \mu(s) - \pi Q] d\sigma. \quad (2.44)$$

A derivation of the dispersion function can be found in [4]. From the equation above one notes that a finite dispersion only exists if the number of betatron oscillations per revolution is different from an integer. For an integer tune, off-momentum particles would be lost after a small number of turns due to resonance effects.

A more detailed and complete introduction to accelerator physics can be found in [2, 4, 5].

Chapter 3

Theory on imperfections and resonances

This chapter treats the action of imperfections and resonances on the beam in a synchrotron. So far only the linear lattice (including the main dipoles and main quadrupoles) was considered. When talking about imperfections in a machine, one generally refers to additional dipole or quadrupole kicks which excite first or second order resonances respectively. Resonances of higher order (excited with contributions from sextupoles onwards) are called non-linear resonances. Imperfections lead to linear inhomogeneous differential equations for the transverse particle motion. The general solution of these equations is found by adding the solution of the homogeneous and inhomogeneous equations. To describe non-linear resonances a perturbative treatment of the Hamiltonian has to be done.

First a general multipole expansion of the magnetic field is given, leading to a Hamiltonian H including all contributions of non-linear elements. Then a more descriptive insight about imperfections and resonances is presented. Finally principles about maps in accelerators and the Normal Form technique are described to link the spectral decomposition of the particle motion to resonance strength and phase.

3.1 General multipole expansion of the magnetic field

In good approximation, the magnetic field in accelerator magnets consists only of transverse field components. Thus the vector potential \vec{A} only has a component in the longitudinal direction s . In current-free regions one can furthermore consider that the Maxwell equations in vacuum for the magnetic field \vec{B} are given by [2],

$$\operatorname{div}\vec{B} = 0, \quad (3.1)$$

$$\operatorname{rot}\vec{B} = 0. \quad (3.2)$$

The magnetic field \vec{B} can then be written as,

$$\vec{B} = \operatorname{rot}\vec{A} \quad (3.3)$$

or as gradient of a scalar potential V :

$$\vec{B} = -\operatorname{grad}V. \quad (3.4)$$

Combining equations 3.3 and 3.4 yields,

$$B_x = -\frac{\partial V}{\partial x} = \frac{\partial A_s}{\partial y}, \quad (3.5)$$

$$B_y = -\frac{\partial V}{\partial y} = -\frac{\partial A_s}{\partial x}. \quad (3.6)$$

Equations 3.5 and 3.6 are just the Cauchy-Riemann conditions for the real and imaginary part of an analytic function. Thus, one can define a complex potential function

$$\tilde{A}(z) = A_s(x, y) + iV(x, y), \quad (3.7)$$

where $z = x + iy$ and $\tilde{A}(z)$ can be expanded in a power series

$$\tilde{A}(z) = \sum_{n=1}^{\infty} \frac{1}{n} [B_n(s) + iA_n(s)] \cdot (x + iy)^n. \quad (3.8)$$

The terms $B_n(s)$ and $A_n(s)$ are called the normal and skew coefficients of the field expansion respectively and are given by the expressions

$$B_n(s) = \frac{1}{(n-1)!} \left[\frac{\partial^{n-1} B_y}{\partial x^{n-1}} \right]_{y=0}, \quad (3.9)$$

$$A_n(s) = \frac{1}{(n-1)!} \left[\frac{\partial^{n-1} B_x}{\partial x^{n-1}} \right]_{y=0}. \quad (3.10)$$

Then the magnetic field can be expressed as,

$$B(x, y, s) = B_y(x, y, s) + iB_x(x, y, s) = -\frac{\partial}{\partial x} (A_s + iV) = -\sum_{n=1}^{\infty} [B_n(s) + iA_n(s)] \cdot (x + iy)^{n-1} \quad (3.11)$$

For a perturbative treatment of the transverse particle motion, the linear equations of motion (Hills equations, Eqs. 2.14 and 2.15) have to be extended to,

$$x'' + \left(\frac{1}{\rho_0(s)^2} - k(s) \right) x = -\frac{q}{p_0} A_2 y + \frac{q}{p_0} \operatorname{Re} \left[\sum_{n=3}^{\infty} [B_n(s) + iA_n(s)] \cdot (x + iy)^{n-1} \right] \quad (3.12)$$

$$y'' + k(s)y = -\frac{q}{p_0} A_2 x - \frac{q}{p_0} \operatorname{Im} \left[\sum_{n=3}^{\infty} [B_n(s) + iA_n(s)] \cdot (x + iy)^{n-1} \right] \quad (3.13)$$

where the prime denotes the derivative w.r.t. the longitudinal coordinate s . No off-momentum particles are considered and the coefficients B_1 and B_2 are already contained in the normalised dipole and quadrupole strengths $\rho_0(s)$ and $k(s)$. The vertical dipole component A_1 is set to zero. The right hand side of the equations shows first the coefficient A_2 due to skew quadrupoles, leading to linear coupling between the two transverse planes. All the higher order multipole contributions are represented within the sum, starting with sextupolar terms ($n=3$, second order in x and y). Higher order multipoles are, for example, the octupole ($n=4$, third order in x and y) and the decapole ($n=5$, fourth order in x and y).

In presence of these non-linear terms, the equations of motion are no longer integrable and a perturbative approach has to be used.

The map theory (Section 3.4) can be used to obtain approximate expressions to describe the transverse particle motion in the presence of non-linearities. The map theory is based on the Hamiltonian formalism and the exponential Lie operator (Section 3.4.2). Therefore it is necessary to construct Hamiltonians that generate the linear and non-linear equations of motion. The linear Hamiltonian $H_0(x, p_x, y, p_y, s)$ that generates Eqs. 2.14 and 2.15 is given by [6],

$$H_0 = \frac{1}{2} \left[\left(\frac{1}{\rho_0(s)^2} - k(s) \right) \cdot x^2 + k(s) \cdot y^2 + p_x^2 + p_y^2 \right]. \quad (3.14)$$

The total Hamiltonian can be expressed as the sum of $H_0 + H_1$ where H_1 contains the contributions of all the non-linear elements. H_1 is proportional to A_s , the longitudinal component of the vector potential \vec{A} . Hence H_1 is proportional to the real part of Eq. 3.8 and the total Hamiltonian is given by,

$$H = H_0 - \frac{q}{p_0} \text{Re} \left[\sum_{n=3}^{\infty} \frac{1}{n} [B_n(s) + iA_n(s)] \cdot (x + iy)^n \right]. \quad (3.15)$$

H_1 is assumed to be a perturbation to the integrable Hamiltonian H_0 . The perturbative approach used in this work consists of the following steps:

- The construction of the one-turn-map including non-linear elements. Basically the one-turn-map is a composition of successive element maps to relate the initial position of the particle in the phase space to the final position after one turn (Section 3.4.3).
- A change of coordinates into *Normal Form* coordinates with a generating function F to obtain a simpler one-turn-map (Section 3.4.4).
- The initial phase space coordinates are expressed in terms of Normal Form coordinates and related to the spectral decomposition of the particle motion (Section 3.4.5).

Before discussing the perturbative approach, a descriptive insight on imperfections and resonances is presented.

3.2 Overview on imperfections and resonances

For a brief introduction to imperfections and resonances, the particle motion is limited to the horizontal plane, $y = 0$. Then only the real part of the multipole expansion of the magnetic field is of interest and Eq. 3.11 can be written as,

$$B(x, y, s) = - \sum_{n=1}^{\infty} B_n(s) \cdot x^{n-1}. \quad (3.16)$$

In Eq. 3.12 the coefficients B_1 and B_2 are already contained in the normalised dipole and quadrupole strengths $\rho_0(s)$ and $k(s)$. As additional dipole and quadrupole contributions are considered, the perturbing dipole and quadrupole terms, ΔB and B_2^* , are introduced. Eq. 3.12 then yields:

$$x'' + \left(\frac{1}{\rho_0(s)^2} - k(s) \right) x = - \frac{1}{B_0 \rho_0} [\Delta B + B_2^* \cdot x + B_3 \cdot x^2 + \dots]. \quad (3.17)$$

The first term on the right hand side represents the perturbation due to dipolar field errors, the second term comes from quadrupole contributions and the third term represents perturbations due to sextupolar fields. Each term is discussed in more detail in the following sections.

3.2.1 Closed-Orbit distortions from dipole kicks

Dipole field errors introduce sinusoidal oscillations about the design orbit in the normalised phase space. Eg. 3.17 yields for dipole perturbations only,

$$x'' + \left(\frac{1}{\rho_0(s)^2} - k(s) \right) x = - \frac{\Delta B}{B_0 \rho_0}. \quad (3.18)$$

The solution of above equation is similar to the one obtained for off-momentum particles (Section 2.5) and is given by,

$$x(s) = \sqrt{\epsilon_x \beta_x(s)} \cos(\mu_x(s) + \phi_x) + x_p(s). \quad (3.19)$$

Similar to the expression for the dispersion function (2.44), the particular solution $x_p(s)$ is expressed as [4],

$$x_p(s) = - \frac{\sqrt{\beta_x(s)}}{2 \sin(\pi Q_x)} \int_s^{s+C} \sqrt{\beta_x(\sigma)} \frac{\Delta B(\sigma)}{B_0 \rho_0} \cos[\mu_x(\sigma) - \mu_x(s) - \pi Q_x] d\sigma. \quad (3.20)$$

This equation gives the *closed-orbit distortion* with respect to the ideal orbit without errors, i. e. $x_p(s) = 0$. Inspection of Eq. 3.20 reveals that the closed orbit will become unstable as the tune Q approaches an integer. This condition is known as *integer resonance* or *first order resonance*. The situation for two different tunes is shown in Fig. 3.1. For Q being an integer, the oscillations induced by a dipole kick grows on each turn and the particle will be lost after a few turns. Since the dipole deflection is independent of the transverse particle position one notes that for a residual fractional part q of the tune, i. e. $q = 0.5$, the motion remains stable.

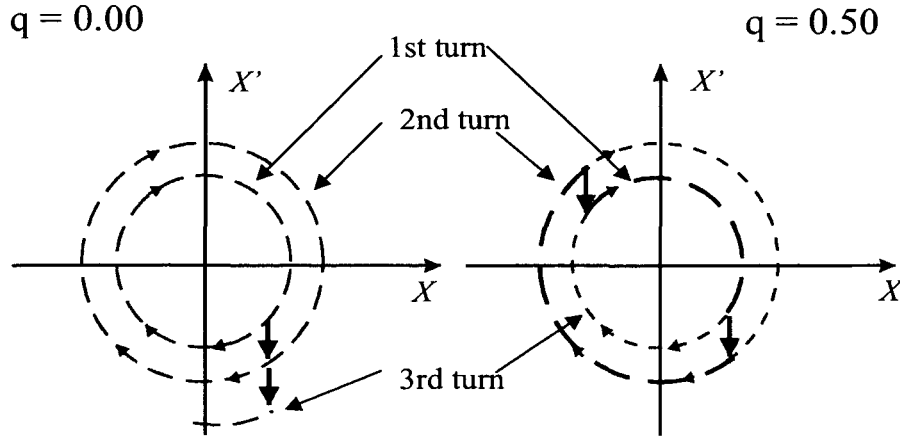


Figure 3.1: Normalised phase space representation of a dipole kick for integer and half-integer tunes.

3.2.2 Quadrupole perturbations

Eq. 3.17 yields for quadrupole perturbations,

$$x'' + \left(\frac{1}{\rho_0(s)^2} - k(s) \right) x = -\frac{B_2^*}{B_0 \rho_0} x. \quad (3.21)$$

The right hand side can be re-written as,

$$-\frac{B_2^*}{B_0 \rho_0} x = -\underbrace{\frac{1}{B_0 \rho_0} \frac{\partial B_y}{\partial x}}_{k_2} x = F_2(x), \quad (3.22)$$

where $F_2(x)$ is the driving term for quadrupole perturbations. For the following explanations some general considerations are of importance and are briefly discussed.

Multipole kicks described in the normalised phase space

The driving term $F_2(x)$ can be generalised for multipoles having $2n$ poles [7]:

$$F_n(x) = \frac{1}{(n-1)!} k_n(s) x^{n-1}, \quad (3.23)$$

where k_n represents the normalised field gradient $-1/(B_0 \rho_0) \cdot (\partial^{n-1} B_y / \partial x^{n-1})$. The driving term $F_n(x)$ acts over a length l of the field error and for the following considerations the thin lens approximation is used for the perturbation. When a particle passes through such a thin magnetic lens, the position remains constant, whereas the divergence changes because of the kick, as represented in Fig. 3.2. The normalised coordinates (X, X') of a particle in the horizontal plane before applying the perturbation can be expressed as,

$$X = r \cos(\theta), \quad (3.24)$$

$$X' = -r \sin(\theta). \quad (3.25)$$

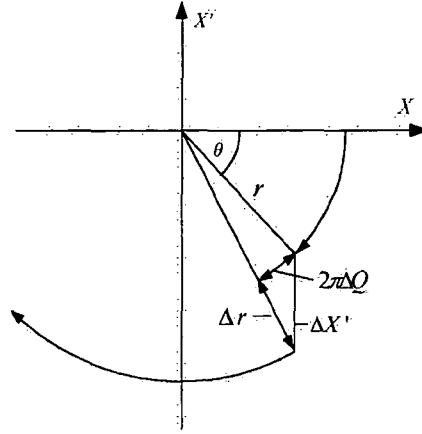


Figure 3.2: Phase space perturbation due to a multipole kick.

The change $\Delta X'$ is given through,

$$\Delta X' = \Delta x' \sqrt{\beta_x} = F_n(x) l \sqrt{\beta_x}. \quad (3.26)$$

Hence the coordinates after the kick are given by,

$$X_{after.kick} = X, \quad (3.27)$$

$$X'_{after.kick} = X' + \underbrace{\frac{l}{(n-1)!} k_n(s) x^{(n-1)} \sqrt{\beta_x}}_{\Delta X'}, \quad (3.28)$$

or expressed in terms of the circular coordinates

$$X_{after.kick} = (r + \Delta r) \cos(\theta + \Delta\theta), \quad (3.29)$$

$$X'_{after.kick} = -(r + \Delta r) \sin(\theta + \Delta\theta), \quad (3.30)$$

where $\Delta\theta = 2\pi\Delta Q$. By substituting Eqs. 3.24 and 3.25 into Eqs. 3.27 and 3.28 and comparing these expressions with Eqs. 3.29 and 3.30 under the assumption of small deviations $\Delta\theta$, the final expressions for the shifts Δr and $\Delta\theta$ are calculated to,

$$\Delta r = \frac{l}{(n-1)!} k_n(s) x^{(n-1)} \sqrt{\beta_x} \sin(\theta), \quad (3.31)$$

$$\Delta\theta = \frac{\frac{l}{(n-1)!} k_n(s) x^{(n-1)} \sqrt{\beta_x} \cos(\theta)}{r + \Delta r}. \quad (3.32)$$

These general expressions are further discussed for quadrupolar and sextupolar perturbations.

According to Eqs. 3.31 the shift Δr due to quadrupolar field errors is expressed as,

$$\Delta r = l k_2 x \sqrt{\beta} \sin(\theta). \quad (3.33)$$

Substituting x with $x = \sqrt{\beta}r\cos(\theta)$ and with the use of the trigonometric expression $\sin(\theta)\cos(\theta) = 1/2\sin(2\theta)$ the shift Δr can be written as,

$$\Delta r = \frac{1}{2}lk_2r\beta\sin(2\theta). \quad (3.34)$$

If many turns are considered, above equation yields,

$$\Delta r = \frac{1}{2}lk_2r\beta \sum_{i=1}^{\infty} \sin(2(\theta + 2\pi Qi)). \quad (3.35)$$

From this expression one notes that Δr averages to zero over many turns unless $q = n \cdot 0.5$ (q being the fractional part of Q , n being an integer). For half-integer and integer tunes the phase term stays constant and therefore Δr will become infinite. A particle oscillating with $q = n \cdot 0.5$ will be lost after a finite number of turns and therefore these tunes have to be avoided. Quadrupoles excite *half-integer* or *second order resonances*. Fig. 3.3 shows on the left hand side the trajectory of a particle oscillating with a half-integer tune and on the right hand side a particle with $q = 0.33$. As expected the oscillation amplitude grows in the first case, while the phase space trajectory remains stable for tune values sufficiently far away from the resonance condition.

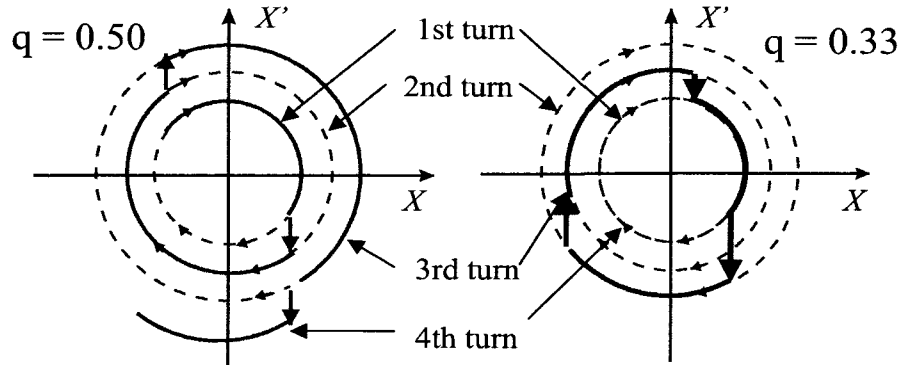


Figure 3.3: Normalised phase space representation of a quadrupole kick for half-integer and third-integer tunes.

The shift of the phase $\Delta\theta$ has to be analysed as well. With the numbers for quadrupoles and taking into account only first order perturbations, Eq. 3.32 yields,

$$\Delta\theta = \frac{1}{2}lk_2\beta[1 + \cos(2\theta)]. \quad (3.36)$$

The summation over many turns gives

$$\Delta\theta = \frac{1}{2}lk_2\beta \left[\sum_{i=1}^{\infty} \cos(2(\theta + 2\pi Qi)) + 1 \right]. \quad (3.37)$$

The sum over the \cos -term vanishes for $q \neq n \cdot 0.5$ and it remains

$$\Delta\theta = \frac{1}{2}lk_2\beta. \quad (3.38)$$

Therefore an average tune shift ΔQ per turn

$$\Delta Q = \frac{l k_2 \beta}{4\pi} \quad (3.39)$$

is obtained. From Eq. 3.36 it follows that the tune values vary within a range $\Delta Q = l k_2 \beta / (2\pi)$. So even if the tune is not a half-integer tune, it must not be too close to the resonance condition, or at some point the particle will find itself exactly at $n \cdot 0.5$ and will "lock" on to the resonance. This "forbidden" tune range is referred to as *stopband* of the resonance and has to be avoided.

3.2.3 Sextupole perturbations

The same considerations can also be applied to treat sextupolar field errors. Eqs. 3.31 and 3.32 yield for the normalised sextupole gradient k_3 a shift in r and θ :

$$\Delta r = \frac{l}{8} k_3 r^2 \beta^{3/2} [3 \sin(\theta) + \sin(3\theta)], \quad (3.40)$$

$$\Delta \theta = \frac{l}{8} k_3 r \beta^{3/2} [3 \cos(\theta) + \cos(3\theta)]. \quad (3.41)$$

Summing up Eq. 3.40 gives

$$\Delta r = \frac{l}{8} k_3 r^2 \beta^{3/2} \sum_{i=1}^{\infty} [3 \sin(\theta + 2\pi Q i) + \sin(3(\theta + 2\pi Q i))]. \quad (3.42)$$

Δr averages to zero unless $q = n \cdot 1/3$. For integer or third-integer tunes the phase term stays constant and Δr will become infinite. A particle oscillating with these tunes will be lost after a finite number of turns (Fig. 3.4). One concludes that sextupoles excite *third-integer* or *third order resonances* as well as integer resonances. The shift in θ averages to zero when many

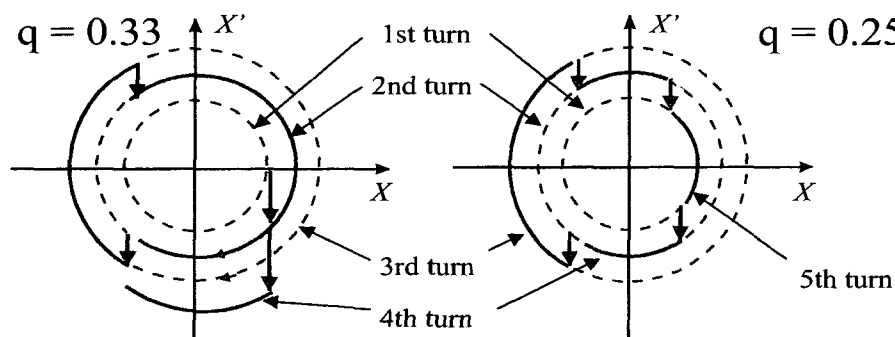


Figure 3.4: Normalised phase space representation of a sextupole kick for a tune fulfilling the resonance condition (left) and a stable tune value.

turns are considered unless Q is an integer or third-integer. If Q is close to a third-integer, the first term in Eq. 3.41 averages to zero and the equation is left with

$$2\pi \Delta Q = \Delta \theta = \frac{l}{8} k_3 r \beta^{3/2} \cos(3\theta). \quad (3.43)$$

Therefore Q has a range of values varying by,

$$\Delta Q = \pm \frac{lk_3 r \beta^{3/2}}{16\pi}. \quad (3.44)$$

Above expression represents the stopband of a third-integer resonance. Particles with tunes close to a third-integer resonances will lock on to the resonance and will be lost. Compared to the stopband for half-integer resonances, it is proportional to the amplitude r of the particle. The r dependence of ΔQ and the growth rate $\Delta r/r$ is used for the so called *slow resonant extraction*, where a third-integer resonance is excited to extract particles from a synchrotron during a large number of turns [23].

For tunes close to a third-integer the first term in Eq. 3.40 averages to zero over many turns and can be neglected. The remaining term is zero for $\theta = n \cdot \pi/3$, hence *fixed points* in the phase space exist, where the amplitude stays constant. A fixed point radius can be expressed by replacing ΔQ in Eq. 3.43 by $Q_0 - p/3$, where Q_0 and $p/3$ represent the unperturbed tune and the tune at resonance condition respectively (p being an integer),

$$r_{fixedpoint} = \frac{16\pi(Q_0 - p/3)}{lk_3\beta^{3/2}}. \quad (3.45)$$

Due to the symmetry of sextupoles, the phase space in vicinity of a third-integer resonance is triangular distorted as shown in Fig. 3.5. The *separatrices* define the boundaries between stable and unstable regions and their points of interception are the unstable fixed points calculated above. The stable fixed point is given by the equilibrium orbit. Particles within the triangle move on stable trajectories, while particles outside will be lost after a sufficient number of turns. One notes from Eq. 3.45 that for particles moving exactly with the resonance tune, no stable trajectories exist. As illustrated a change in sign of either the tune distance to the resonance (particle tune above or below resonance) or the sextupole strength k_3 is equivalent to a rotation of the phase-space trajectories by 180° .

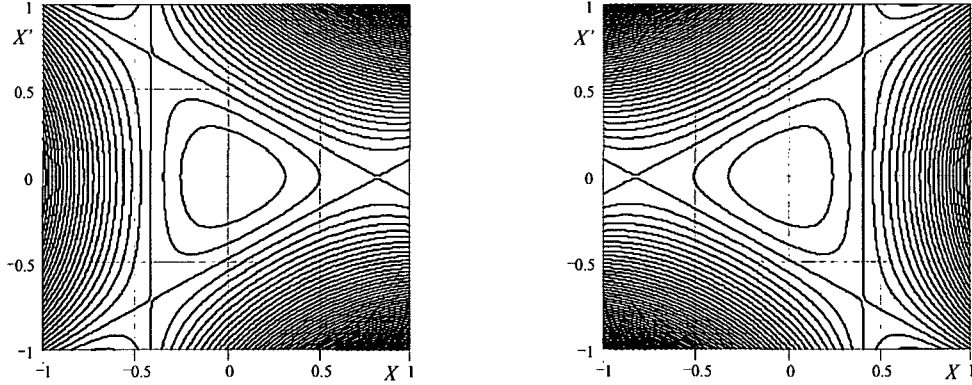


Figure 3.5: Normalised phase space in presence of sextupoles, a change in sign of either the tune distance to the resonance or the sextupole strength is equivalent to a rotation of the phase-space trajectories by 180° .

3.3 General numerology of resonances

So far only single multipole kicks were considered. In a real machine one has to assume an azimuthal distribution of the multipoles around the circumference of the accelerator which can be expressed as a Fourier series. Therefore the general resonance condition is given by,

$$n_x Q_x \pm n_y Q_y = p, \quad (3.46)$$

where $n_x + n_y = n$ represents the order of the resonance and defines the principal driving multipole, which has $2n$ poles. The integers n_x and n_y are positive and one may be zero. The azimuthal harmonic in the distribution of the $2n$ th multipole error is represented by p and drives the corresponding resonance of n th order. For a given order n there are $n + 1$ separate resonance conditions and each of them corresponds to a different term in the cartesian multipole expansion of the magnetic vector potential (see Section 3.1). Some resonances are excited by regular multipoles, others by skew multipoles. A skew multipole of order n is a normal multipole of order n rotated by $90^\circ/n$ in the transverse plane. The positive sign in the general resonance condition stands for resonances known as *sum resonances*, the negative sign is for *difference resonances*. Resonances where both n_x and n_y are positive are referred to as *coupling resonances*. Special attention has to be paid when the azimuthal harmonic p corresponds to a multiple of the machine superperiodicity. The resonance excitation is then sensitive to systematic errors in the accelerator lattice. These resonances are called *systematic* or *structure resonances* and are likely to be strong. The resonance lines are represented in the *tune diagram* (Fig. 4.5 shows the tune diagram for the CERN PS Booster synchrotron) and a *working point* free of low-order resonances has to be used for machine operation. During normal operation resonance compensation is mandatory to avoid an emittance increase (*beam blow-up*) or even beam losses.

3.3.1 Linear coupling

The lowest order coupling resonance is referred to as *linear coupling resonance*, with the resonance condition

$$Q_x \pm Q_y = p. \quad (3.47)$$

In general, coupling leads to an exchange of energy between the two transverse planes. The equations of motion (2.14 and 2.15) are no longer decoupled. The sources for linear coupling are quadrupole tilts, skew quadrupoles or solenoids. Horizontal betatron motion is transformed into vertical motion and vice versa. In fact an emittance exchange between both planes takes place, leading to a change of the particle amplitudes and eventually to particle losses.

3.4 Taylor maps

So far the behaviour of particles close to resonances was presented in a descriptive way. For a perturbative treatment of the Hamiltonian, a basic knowledge of maps in accelerators and the Normal Form technique are of importance and are explained in the following.

A Taylor map expresses a final set of coordinates as polynomial functions of an initial set of coordinates. One way to represent this kind of map is to use the exponential Lie operator. In this section the basic principles of Lie algebra are presented. A more detailed description can be found in Ref. [10].

The exponential Lie operator is written as $e^{:f:}$ and operates on differentiable functions. It is defined by,

$$e^{:f:}g = g + [f, g] + \frac{1}{2}[f, [f, g]] + \dots, \quad (3.48)$$

where $[f, g]$ is the Poisson bracket of any functions f and g of the phase space coordinates defined by,

$$[f, g] = \frac{\partial f}{\partial \vec{x}} \frac{\partial g}{\partial \vec{p}} - \frac{\partial f}{\partial \vec{p}} \frac{\partial g}{\partial \vec{x}}. \quad (3.49)$$

3.4.1 Representation of a multipole kick with Lie operators

When a particle passes through a thin magnetic lens the position coordinates stay unchanged. The map corresponding to this lens changes only the momentum coordinates and can be represented by a Hamiltonian which depends only on the position coordinates. Thus any thin magnetic multipole kick is given by [10, 8],

$$H(x, y) = -f(x, y) = -\frac{qL}{p}A_s(x, y), \quad (3.50)$$

where q is the charge of the particle, L is the length of the magnet, p is the momentum of the particle and A_s is the longitudinal component of the magnetic vector potential. According to Eq. 3.15, the Hamiltonian for a normal sextupole of length L is given by,

$$-\frac{qLB_3}{3p}(x^3 - 3xy^2). \quad (3.51)$$

Therefore the Lie operator, operating on the initial phase space coordinates x_0 , p_{x0} , y_0 and p_{y0} leads to,

$$\begin{aligned} x_f &= e^{\frac{qLB_3}{3p}(x_0^3 - 3x_0y_0^2)}x_0 = x_0, \\ p_{xf} &= e^{\frac{qLB_3}{3p}(x_0^3 - 3x_0y_0^2)}p_{x0} = p_{x0} + \frac{qLB_3}{p}(x_0^2 - y_0^2), \\ y_f &= e^{\frac{qLB_3}{3p}(x_0^3 - 3x_0y_0^2)}y_0 = y_0, \\ p_{yf} &= e^{\frac{qLB_3}{3p}(x_0^3 - 3x_0y_0^2)}p_{y0} = p_{y0} - \frac{qLB_3}{p}(2x_0y_0). \end{aligned} \quad (3.52)$$

One notices that only the momentum coordinates are changed by the map. This is known as a “multipole kick” and its Hamiltonian is called “kick Hamiltonian”. To construct the one-turn map of an accelerator, including multipole kicks represented by exponential Lie operators, specific properties of the operator are used and described in the following section.

3.4.2 Properties of the exponential Lie operator

Two properties of the exponential Lie operator are needed for the construction of the one-turn map including multipole kicks.

- **Composition of exponential Lie operators.** For two operators, $e^{:f_1(z_1):}$ mapping the phase space z_1 into the phase space z_2 and $e^{:f_2(z_2):}$ mapping z_2 into z_3 , the composition of the maps is expressed as,

$$z_3 = e^{:f_2(z_2):} e^{:f_1(z_1):} z_1 = e^{:f_2(z_2):} z_2 = g(z_2). \quad (3.53)$$

For polynomial functions $g(z)$ it can be shown that

$$g(e^{:f:} z) = e^{:f:} g(z). \quad (3.54)$$

With this equation, the composition of the maps is given by,

$$z_3 = g(z_2) = g(e^{:f_1(z_1):}) z_1 = e^{:f_1(z_1):} g(z_1) = e^{:f_1(z_1):} e^{:f_2(z_1):} z_1. \quad (3.55)$$

This equation shows the very important property that a succession of Lie operators can be expressed in the initial coordinates only. This is indispensable for the construction of the one-turn map of an accelerator.

- **The Campbell-Baker-Hausdorff theorem.** The product of two exponential Lie operators can be expressed by another exponential Lie operator:

$$e^{:f_2:} e^{:f_1:} = e^{:f:} \quad (3.56)$$

with the function f given by,

$$f = f_2 + f_1 + [f_2, f_1] + \dots \quad (3.57)$$

The functions f_1 and f_2 are considered to be small. The proof of this theorem is given in Ref. [11].

3.4.3 The one turn map

The one-turn map of a circular accelerator consists of a set of functions that relate the initial coordinates of the particle to the final coordinates after one turn. The one-turn map, including non-linear elements, is given by the composition of successive element maps in the form,

$$\mathcal{M} = e^{:h_I:} M_I e^{:h_{I-1}:} \dots e^{:h_2:} M_2 e^{:h_1:} M_1, \quad (3.58)$$

where M_i represents the maps of the linear elements (see Section 2.4) and the $h_i = h_i(x_i, y_i)$ are the kick Hamiltonians of the non-linear thin lenses at the longitudinal coordinate $s = s_i$. According to first property of Lie operators (Eq. 3.55) the product \mathcal{M} can be written in terms of the initial coordinates by simply reversing the order of the elements leading to,

$$\mathcal{M} = M_1 e^{:h_1:} M_2 e^{:h_2:} \dots M_I e^{:h_I:}. \quad (3.59)$$

With the definition $\bar{M}_i = M_1 M_2 \dots M_i$ and the insertion of the identities $M_i^{-1} M_i$ into Eq. 3.59, the non-linear kicks can be transferred to the front of the lattice [10]:

$$\mathcal{M} = e^{:\bar{M}_1 h_1:} e^{:\bar{M}_2 h_2:} \dots e^{:\bar{M}_I h_I:} \bar{M}_I. \quad (3.60)$$

\bar{M}_I is the linear one turn map and can be expressed by the similarity transformation,

$$\bar{M}_I = A R A^{-1}, \quad (3.61)$$

where A represents a transformation and R a rotation. When only pure rotation is left, Eq. 3.60 yields:

$$\mathcal{M} = e^{:\tilde{h}_1:} e^{:\tilde{h}_2:} \dots e^{:\tilde{h}_I:} R. \quad (3.62)$$

Using the second property of Lie operators, the Campbell-Baker-Hausdorf theorem, the equation above simplifies to,

$$\mathcal{M} = e^{:h:} R, \quad (3.63)$$

where,

$$h = \sum_{i=1}^I \tilde{h}_i + \sum_{i,j < i} [\tilde{h}_j, \tilde{h}_i] + \dots \quad (3.64)$$

In the following only first order terms in \tilde{h}_i are kept, i. e. the second summation on the right hand side will be neglected.

Eq. 2.18 can be rewritten for both transverse planes as,

$$\begin{aligned} x_i &= \sqrt{2\beta_{x_i} J_x} \cos(\phi_x + \phi_{x_i}), \\ y_i &= \sqrt{2\beta_{y_i} J_y} \cos(\phi_y + \phi_{y_i}), \end{aligned} \quad (3.65)$$

where β_{zi} , ϕ_{zi} are the beta function and the phase advance at the location $s = s_i$ in both transverse planes. J_z and ϕ_z are the action-angle variables defined by the initial conditions. Compared to Eq. 2.18 J_z corresponds to half of the transverse emittance. Using the perturbative part H_1 of Eq. 3.15 and inserting Eqs. 3.65 in the modified form

$$\begin{aligned} x_i &= \sqrt{2\beta_{x_i} J_x} \frac{e^{i(\phi_x + \phi_{x_i})} + e^{-i(\phi_x + \phi_{x_i})}}{2} \\ y_i &= \sqrt{2\beta_{y_i} J_y} \frac{e^{i(\phi_y + \phi_{y_i})} + e^{-i(\phi_y + \phi_{y_i})}}{2} \end{aligned} \quad (3.66)$$

yields

$$h = \sum_{jklm} h_{jklm} (2J_x)^{\frac{j+k}{2}} (2J_y)^{\frac{l+m}{2}} e^{i[(j-k)\phi_x + (l-m)\phi_y]}, \quad (3.67)$$

where h_{jklm} are the Hamiltonian coefficients containing the contributions from all the multi-poles of order $n = j + k + l + m$. They are represented as,

$$h_{jklm} = -\frac{q}{p_0} \frac{1}{2^n} \frac{1}{n} \binom{n}{l+m} \binom{j+k}{j} \binom{l+m}{l} \sum_i L_i \beta_{x_i}^{\frac{j+k}{2}} \beta_{y_i}^{\frac{l+m}{2}} V_{ni} e^{i[(j-k)\phi_{x_i} + (l-m)\phi_{y_i}]}, \quad (3.68)$$

where the summation is done over all the existing multipoles in the machine. The perturbation term V_n stands for the multipole coefficients A_n (in case $l + m$ is an odd number) and B_n (in case $l + m$ is an even number) respectively.

As an example the h_{3000} Hamiltonian coefficient in presence of normal sextupoles is given by,

$$h_{3000} = -\frac{q}{p_0} \frac{1}{24} \sum_i L_i \beta_{xi}^{\frac{3}{2}} B_{3i} e^{i3\phi_{xi}}. \quad (3.69)$$

3.4.4 Normal Form

The basic principle of the Normal Form approach is to introduce a coordinate system, where the Hamiltonian H depends on action variables only. Since the new Hamiltonian will be independent of angle variables, the action is a constant of motion. For this transformation a generating function F is needed. Fig. 3.6 shows the principle of this idea.

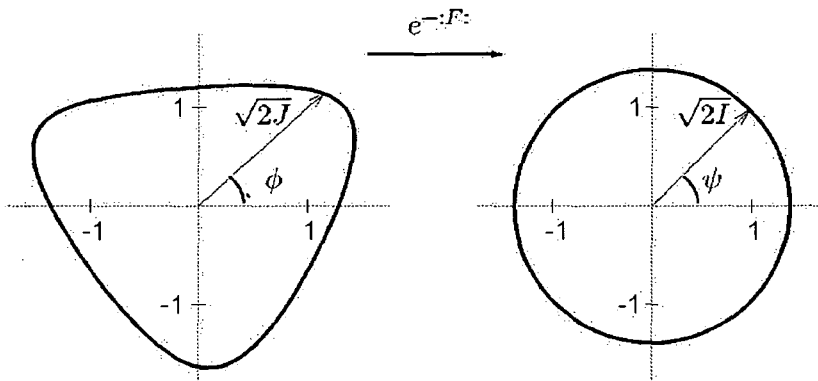


Figure 3.6: Normalised phase space portraits in initial coordinates (left) and in Normal Form coordinates (right) [20].

On the left hand side the phase space trajectory of a particle in presence of strong sextupolar fields is shown. After applying the transformation e^{-iF} , the action stays constant as visible on the right hand side. The one-turn map in Normal Form coordinates is an amplitude dependent rotation (the rotation angle in phase space depends on the oscillation amplitude of the particles) represented by,

$$e^{iH(I)} R, \quad (3.70)$$

where $H(I)$ is the new Hamiltonian depending on the action I only and R is the rotation matrix. The generating function F is expressed in the form [16]

$$F = \sum_{jklm} f_{jklm} (2I_x)^{\frac{j+k}{2}} (2I_y)^{\frac{l+m}{2}} e^{i[(j-k)(\psi_x + \psi_{x0}) + (l-m)(\psi_y + \psi_{y0})]}, \quad (3.71)$$

where I_z and ψ_z are the new action and angle variables. The generating function terms f_{jklm}

are related to the Hamiltonian coefficients h_{jklm} by the relation

$$f_{jklm} = \frac{h_{jklm}}{1 - e^{i2\pi[(j-k)Q_x + (l-m)Q_y]}}, \quad (3.72)$$

where Q_x and Q_y are the horizontal and vertical tunes respectively. The generating function terms diverge when the general resonance condition

$$(j - k)Q_x + (l - m)Q_y = p \quad (3.73)$$

is fulfilled, where $j - k = n_x$ and $l - m = n_y$ compared to expression 3.46. The order of resonance is given by $n = j + k + l + m$ and p is any integer representing the azimuthal harmonic in the distribution of the multipole errors around the ring. Every generating function and Hamiltonian term is associated to a certain resonance and excites all the appertaining harmonics. For this reason these terms are referred to as resonance driving terms.

3.4.5 The non-linear motion and its spectrum

In the linear case the relations between the action angle variables $(J_x, \phi_x, J_y, \phi_y)$ and the normalised Courant-Snyder variables (X, X', Y, Y') are given by the formula (Z stands for X and Y):

$$Z = \sqrt{2J_z} \cos(\phi_z + \phi_{z0}), \quad (3.74)$$

$$Z' = -\sqrt{2J_z} \sin(\phi_z + \phi_{z0}), \quad (3.75)$$

where ϕ_{z0} is the initial phase. It is convenient to express the linearly normalised variables in the so called resonance basis $\mathbf{h} = (h_x^+, h_x^-, h_y^+, h_y^-)$ defined by [16],

$$h_z^\pm = Z \pm iZ' = \sqrt{2J_z} e^{\mp i(\phi_z + \phi_{z0})}. \quad (3.76)$$

The transformation to the new set of canonical coordinates $\zeta = (\zeta_x^+, \zeta_x^-, \zeta_y^+, \zeta_y^-)$ which brings the map into the Normal Form is given by the operator $e^{-:F:}$ and is expressed as,

$$\zeta_z^\pm = \sqrt{2I_z} e^{\mp i(\psi_z + \psi_{z0})} = e^{-:F:} h_z^\pm, \quad (3.77)$$

where I_z is the invariant of the motion in the new frame and represents together with ψ_z the nonlinear action-angle variables. The generating function was introduced in Eq. 3.71 and can be rewritten in terms of the new canonical coordinates ζ as,

$$F = \sum_{jklm} f_{jklm} \zeta_x^{+j} \zeta_x^{-k} \zeta_y^{+l} \zeta_y^{-m}. \quad (3.78)$$

The last step is to express the initial phase space coordinates in terms of Normal Form coordinates and to relate this expression to the spectral decomposition of the particle motion. The transformation from the set of canonical coordinates ζ back to the linearly normalised variables is given by,

$$h = e^{:F:} \zeta = \zeta + [F, \zeta] + \dots, \quad (3.79)$$

where $[F, \zeta]$ denotes the Poisson bracket of F and ζ . To first order the transformation to h_x^- is expressed as,

$$h_x^- \approx \zeta_x^- + [F, \zeta_x^-] = \zeta_x^- - 2i \sum_{jklm} j f_{jklm} \zeta_x^{+j-1} \zeta_x^{-k} \zeta_y^{+l} \zeta_y^{-m}. \quad (3.80)$$

The evolution of the coordinates in Normal Form after N turns is given by,

$$\zeta_z^\pm(N) = \sqrt{2I_z} e^{\mp i(2\pi\nu_z N + \psi_{z0})}, \quad (3.81)$$

where ν_z represents the horizontal or vertical tune of the particle including the amplitude dependent detuning.

Using the last two equations the turn-by-turn motion in linearly normalised coordinates is obtained. The evolution after N turns is expressed in the form [16]:

$$\begin{aligned} h_x^-(N) = & \sqrt{2I_x} e^{i(2\pi\nu_x N + \psi_{x0})} \\ & - 2i \sum_{jklm} j f_{jklm} (2I_x)^{\frac{j+k-1}{2}} (2I_y)^{\frac{l+m}{2}} \\ & e^{i[(1-j+k)(2\pi\nu_x N + \psi_{x0}) + (m-l)(2\pi\nu_y N + \psi_{y0})]}. \end{aligned} \quad (3.82)$$

This equation describes the motion of the particle in the presence of non-linearities. It is equivalent to the spectral decomposition of the particle motion represented by,

$$h_x^-(N) = \sum_{j=1}^{\infty} a_j e^{i[2\pi(m_j\nu_x N + n_j\nu_y N) + \psi_j]}, \quad (3.83)$$

where a_j and ψ_j are the amplitude and phase of the corresponding spectral lines.

The amplitudes and phases of the spectral lines can be compared with those of the generating function terms and Hamiltonian terms. Normally one is interested in the strength $|h_{jklm}|$ and phase ψ_{jklm} of the Hamiltonian driving terms, because these are directly related to the multipole coefficients A_n and B_n . Table 3.1 shows the relation between the driving terms and the corresponding spectral lines in the horizontal spectrum. Similar relations are obtained for the vertical spectrum.

The initial phases of the fundamental tunes are represented by ψ_{x0} and ψ_{y0} and $\hat{\phi} = \pi[(j-k)\nu_x + (l-m)\nu_y]$ is a measure for the distance to the resonance. The frequencies of the spectral lines are the fundamental tunes ν_x and ν_y and their linear combinations, representing the resonance lines. Each spectral line in a Fourier spectrum of the horizontal phase space defined by $(1-j+k)\nu_x + (m-l)\nu_y$ is driven by a Hamiltonian coefficient h_{jklm} , which is responsible for the excitation of the $(j-k, l-m)$ resonance. For example the third order resonance (3,0) drives the spectral line (-2,0), i.e. $1-j+k = -2$ and $l-m = 0$. This also implies that several driving terms h_{jklm} can contribute to the same spectral line.

To measure resonance driving terms in a real accelerator a Fast Fourier Transform (FFT) is applied to the turn-by-turn complex signal $h_x^-(N)$. To construct this signal the beam position Z and the divergence Z' are needed. In an accelerator the positions are obtained from Pick-Ups (PUs). It is however possible to reconstruct the divergence using two adjacent PUs.

If the phase advance between the two PUs is exactly $\pi/2$ the first one gives the position and the second one allows to reconstruct the divergence at the first PU from Eq. 3.75. A detailed description on how to derive the phase space and subsequently the driving terms in the PS Booster is given in Section 4.5.

Driving Term		Horizontal Spectral Line
Line		$(1 - j + k, m - l)$
Amplitude	$ h_{jklm} $	$(2I_x)^{\frac{j+k-1}{2}} (2I_y)^{\frac{l+m}{2}} \frac{j \cdot h_{jklm} }{\sin(\hat{\phi})}$
Phase	ψ_{jklm}	$\psi_{jklm} + (1 - j + k)\psi_{x_0} - (l - m)\psi_{y_0} - \frac{\pi}{2} + \text{sgn}(\hat{\phi})(\frac{\pi}{2} - \hat{\phi})$
where $\hat{\phi} = \pi[(j - k)\nu_x + (l - m)\nu_y]$		

Table 3.1: Relation between the horizontal spectral lines and the amplitude and phase of the resonant Hamiltonian term [16].

Driving Term		Vertical Spectral Line
Line		$(k - j, 1 - l + m)$
Amplitude	$ h_{jklm} $	$(2I_x)^{\frac{j+k}{2}} (2I_y)^{\frac{l+m-1}{2}} \frac{l \cdot h_{jklm} }{\sin(\hat{\phi})}$
Phase	ψ_{jklm}	$\psi_{jklm} - (j - k)\psi_{x_0} + (1 - l + m)\psi_{y_0} - \frac{\pi}{2} + \text{sgn}(\hat{\phi})(\frac{\pi}{2} - \hat{\phi})$
where $\hat{\phi} = \pi[(j - k)\nu_x + (l - m)\nu_y]$		

Table 3.2: Relation between the vertical spectral lines and the amplitude and phase of the resonant Hamiltonian term.

A data acquisition system including several PUs, uniformly distributed around the ring would provide a powerful tool to determine not only strengths and phases of resonances, but also to localise the longitudinal positions of multipolar kicks. In this case, the Hamiltonian and the generating function terms vary around the ring [20]. The change in amplitude from one PU to another then signals the physical presence of a multipole perturbation in between these two PUs. In the PS Booster only one pair of PUs was available, leading to a local determination and compensation of resonance driving terms.

3.5 Spectral response to particle distributions

So far the relation between the spectral lines of the single particle motion and the resonance driving terms was established by means of $h_x^-(N)$ (Eqs. 3.82 and 3.83). However the PUs in a real accelerator record the turn-by-turn transverse position of the centroid of the beam, hence the particle distribution has to be taken into account. For the following summary, a Gaussian distribution of particles that do not interact with each other was considered. The most important effects that influence the centroid motion are decoherence processes, i.e. when the different particles do not oscillate with the same frequency or tune. The two main sources of tune spread are amplitude detuning and chromaticity.

Amplitude detuning is caused by the presence of non-linear magnetic fields. The tunes are functions of the betatron amplitude of the particles. Thus particles with different oscillation amplitudes have different tunes and hence cause a decoherence of the beam. The oscillations of the centroid are completely damped after a certain number of turns. The effect is of first order in strength of octupoles and of second order in strength of sextupoles. The tune spread ν' is written as,

$$\begin{aligned} \nu'_{xx} &= \frac{\partial \nu_x}{\partial \epsilon_x}, & \nu'_{xy} &= \frac{\partial \nu_x}{\partial \epsilon_y}, \\ \nu'_{yx} &= \frac{\partial \nu_y}{\partial \epsilon_x}, & \nu'_{yy} &= \frac{\partial \nu_y}{\partial \epsilon_y}, \end{aligned} \quad (3.84)$$

with $\epsilon_z = 2I_z$. The tunes ν including the amplitude depending detuning and are expressed as:

$$\begin{aligned} \nu_x &= Q_x + \nu'_{xx} 2I_x + \nu'_{xy} 2I_y, \\ \nu_y &= Q_y + \nu'_{yx} 2I_x + \nu'_{yy} 2I_y. \end{aligned} \quad (3.85)$$

The tunes of the particle depend on its momentum as well. For an off-momentum particle with a momentum deviation δp , the change in tune ΔQ is given by,

$$\Delta Q = Q' \cdot \frac{\delta p}{p_0}, \quad (3.86)$$

where Q' is referred to as the *chromaticity*. Chromaticity leads to a tune shift proportional to the momentum spread. This is explained by the fact that particles with different momentum are focused differently by the quadrupoles. In addition, off-momentum particles perform harmonic oscillations around the *synchronous particle* in the longitudinal phase space due to the effect of the rf cavities. The frequency of these oscillations is the *synchrotron tune* Q_s . Therefore the transverse tunes are modulated with the synchrotron tune with the modulation amplitude given by the chromaticity.

These two decoherence effects lead to a reduction in the signal quality and hence increase the difficulty to measure resonance driving terms. The decrease of the amplitude a_j of a spectral line due to amplitude detuning is given by [20],

$$A_{x,jklm} \propto \frac{1}{(1-j+k)\nu'_{xx} + (m-l)\nu'_{yx}} \cdot a_j, \quad (3.87)$$

where $A_{x,jklm}$ represents the reduced amplitude of the spectral line.

If the chromaticity is not corrected the amplitude is further reduced to,

$$H_{x,jklm} \propto A_{x,jklm} \cdot e^{\gamma_{(1-j+k),(m-l)}^2} I_0(\gamma_{(1-j+k),(m-l)}), \quad (3.88)$$

where $\gamma_{(1-j+k),(m-l)} = [(1-j+k)Q'_x + (m-l)Q'_y]\sigma_s/Q_s$ and I_0 is the modified Bessel function of order zero. σ_s is the sigma of the longitudinal distribution.

Chapter 4

The CERN PS Booster Synchrotron

4.1 General layout of the PS Booster

The PS Booster (PSB) is the first synchrotron in the CERN accelerator chain (Fig. 4.1) and links the linear accelerators (Linacs) with the Proton Synchrotron (PS). During standard operation either 50 MeV protons, coming from Linac2 or ions (4.2 MeV/u lead ions (Pb_{208}^{54+}) or 5.5 MeV/u indium ions (In_{115}^{37+})) coming from Linac3, are accelerated and further transferred to the PS. The PSB plays additionally an important role as direct beam supplier for the On-line Isotope Mass Separator facility (ISOLDE).

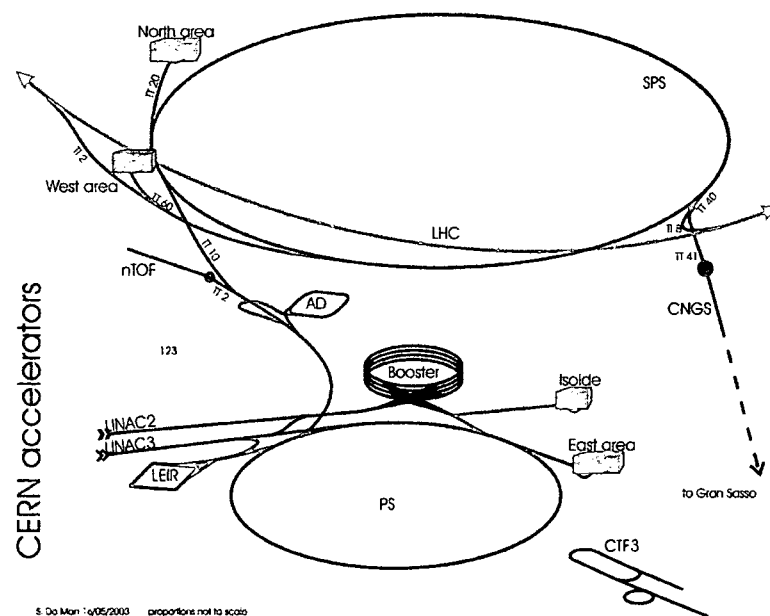


Figure 4.1: The CERN accelerator chain.

The PSB consists of four parallel, superimposed rings, which are filled one after each other. The 4 PSB rings together have exactly the length of the PS ($4 \cdot 25 \text{ m} \cdot 2\pi$), so it is exactly filled when the 4 rings are ejected after each other.

The PSB lattice type is a *regular triplet*. The main lattice elements are placed in the order *bending magnet (BHZ) - focusing quadrupole (QFO) - defocusing quadrupole (QDE) - focusing quadrupole - bending magnet* and are separated by drift spaces. The bending magnets are made from single yokes with four 'C'-type gaps. Fig. 4.2 shows the assembly of period 5. The lattice functions for one period with the standard working point (4.17/5.23) are shown in Fig. 4.3. The PSB consists of 16 identical periods (Fig. 4.4).

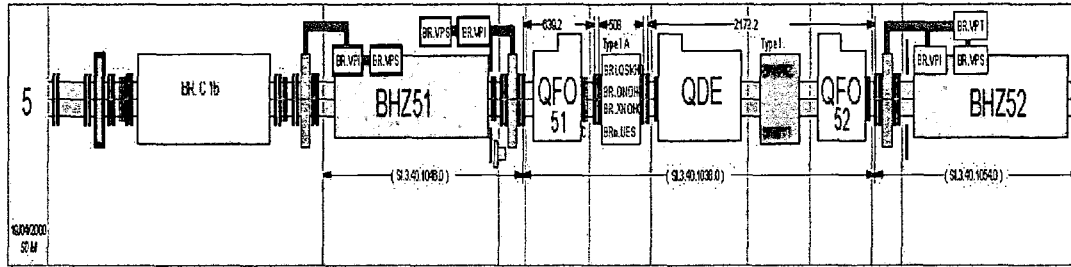


Figure 4.2: Assembly of period 5.

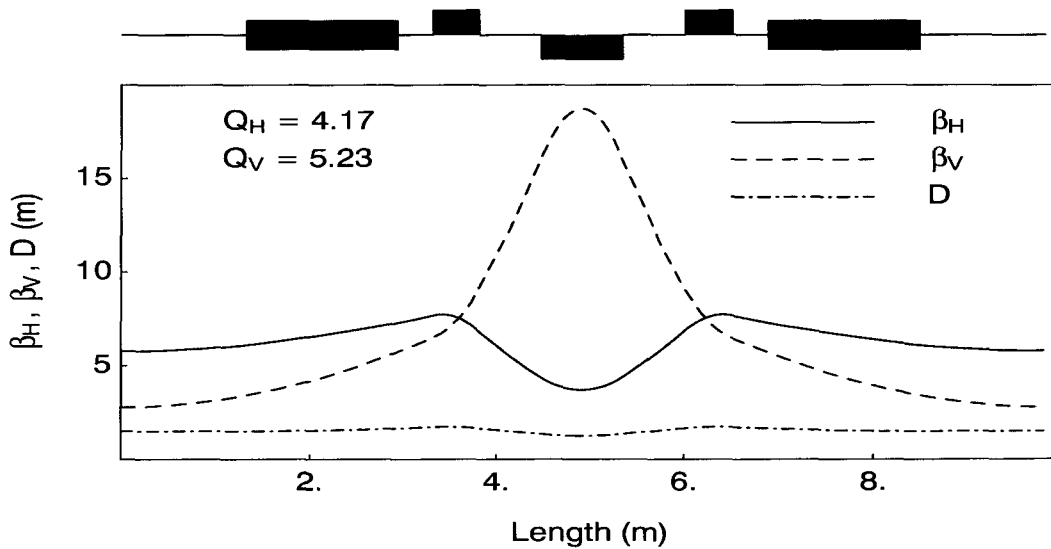


Figure 4.3: Horizontal and vertical beta function and dispersion function for one period.

For the resonance driving term experiments only proton beams and their acceleration and behaviour in the PSB were considered. The 50 MeV protons are fed into the PSB with a so called *multi-turn injection scheme*, meaning that protons are continuously injected during up to 13 turns into the machine. A maximum of $3.5 \cdot 10^{13}$ protons can be injected in the four rings. The particles are then further accelerated in approximately 0.6 s to a top energy of 1.4 GeV and ejected towards the PS or send to the ISOLDE facility. The whole time needed for a complete PSB cycle is 1.2 s.

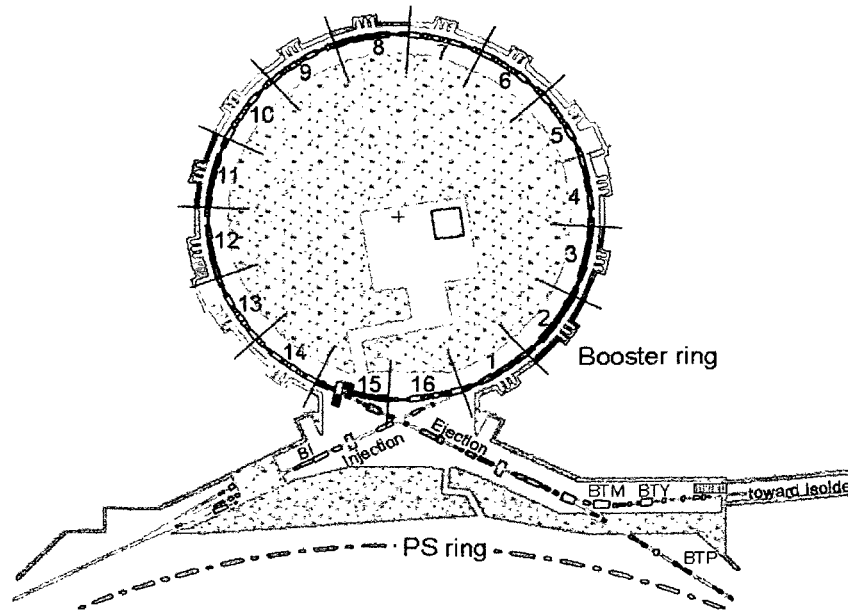


Figure 4.4: Layout of the CERN PS Booster showing the 16 periods.

4.2 Operation of the PS Booster

The PS Booster provides various kinds of beams for its different clients. The range of requirements reaches from low intensity beams (e.g.: Pilot beam for the Large Hadron Collider (LHC) commissioning, single bunch, $5 \cdot 10^9$ protons) up to high intensity and high brightness¹ beams for the LHC, the CERN Neutrinos to Gran Sasso (CNCS) experiment or the ISOLDE facility.

The PSB is operated at the nominal tune values $Q_x = 4.17$ and $Q_y = 5.23$. Due to large incoherent space charge tune spreads [12] associated with high intensity and high brightness beams, especially at injection, the tunes have to be moved towards higher values to prevent particles from crossing the integer resonances $Q_x = 4$ and $Q_y = 5$, as mentioned in Section 3.2.1. Therefore the working point of the PSB is displaced from the nominal tune values up to $Q_x \approx 4.26$ and $Q_y \approx 5.58$. Figure 4.5 shows the so called *Tune Diagram* for the PSB with the resonance pattern up to third order.

The large “necktie” shaped area ($\Delta Q_x \approx 0.25$, $\Delta Q_y \approx 0.5$ due to incoherent space charge tune spread) in the diagram contains all the individual particles of the beam and covers several resonances. Note that individual particles do not stay at constant tunes, but move up and down in this area and repetitively cross the resonances. Fortunately ΔQ shrinks proportionally to $1/\beta\gamma^2$ as the beam is accelerated. The working point is lowered towards the nominal values in an area clear of resonances (*dynamic working point*).

¹The brightness B is an important beam parameter defined by $B = I/\epsilon_x\epsilon_z$, where I is the beam current.

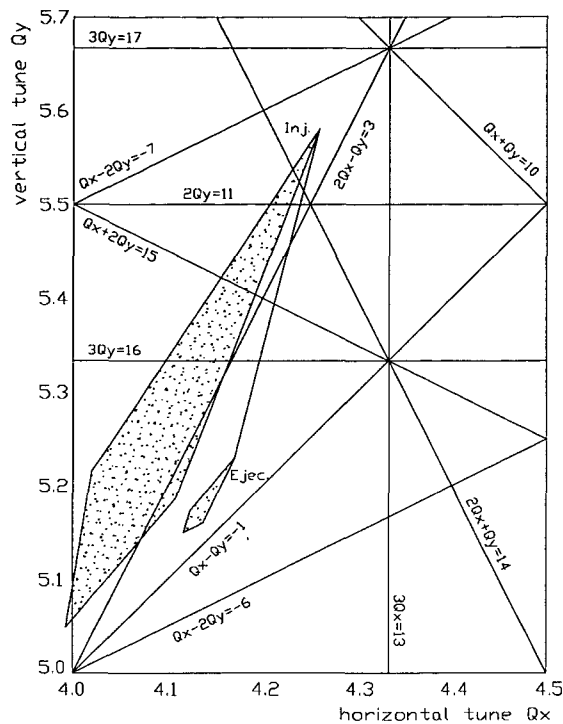


Figure 4.5: PSB Tune diagram for high intensity beams.

It is essential for the performance of the PSB to compensate the concerned resonances. The presently used resonance compensation scheme was established 25 years ago by an orthogonal search for multipole currents minimising beam losses [13]. In view of the increasing demand of high intensity proton cycles, a revisit of the resonance compensation scheme and a resonance analysis was needed.

To compensate betatron resonances, multipole magnets of the corresponding order have to be properly placed in the lattice. With the knowledge of strength and phase of a particular resonance of the bare (uncorrected) machine from measurements, one can deduce the necessary currents for two independent multipoles (multipole families), to compensate the influence of the bare machine, thus stabilising the particle motion. Table 4.1 shows all additional multipole magnets to compensate resonances up to third order and their location in the PSB.

The first three letters of the name indicate the type of the multipole, the number afterwards the period and the "Lx" the drift space in this period where the multipole is located. Two numbers for the period (e.g. 4 and 12 in QNO412L3) indicate that two multipoles located in these two periods are connected in series and fed by one power supply. It is important to power all magnets in a family with the correct polarity with respect to each other. To underline this, one example is stated: For the compensation of the $2Q_y = 11$ resonance, normal quadrupoles are needed. There are two corrector quadrupoles placed exactly opposite in the machine in sections 4L3 and 12L3. The resonance phase advance over the whole circumference is 11 times 2π ,

Type	n	Name	Nom. current [A]	Strength [T/m^{n-1}]	Length [m]
Quadrupole normal	2	QNO311L1	85	0.1724	0.287
		QNO412L3			
		QNO816L1			
		QNO816L3			
Quadrupole skew	2	QSK210L3	85	0.1724	0.287
		QSK614L3			
Sextupole normal	3	XNO311L1	270	6.37	0.322
		XNO4L1		7.35	0.306
		XNO6L1		7.35	0.306
		XNO816L1		6.37	0.322
		XNO9L1		7.35	0.306
		XNO12L1		7.35	0.306
Sextupole skew	3	XSK2L4	270	8.39	0.358
		XSK4L1		7.56	0.308
		XSK6L1		7.56	0.308
		XSK6L4		8.39	0.358
		XSK9L1		7.56	0.308
		XSK11L4		8.39	0.358
		XSK12L1		7.56	0.308
		XSK12L4		8.39	0.358

Table 4.1: Additional quadrupoles and sextupoles in the PS Booster.

hence between the two quadrupoles it is 5.5 times 2π . If these two quadrupoles were powered with the same polarity, the two compensation vectors would cancel out and no overall effect on the beam would be obtained. Therefore the polarity of these two elements has to be opposite.

The following list completes the description of multipole magnets in the PSB:

- One sextupole family for chromaticity correction (one sextupole per period located in drift space L3) represented by XNOH0. Since the natural chromaticity of the machine ($Q'_x \approx -3.5$ and $Q'_y \approx -9.3$) is not corrected during standard operation these sextupoles are not used.
- One zero harmonic skew quadrupole family (QSKH0, one element in every second period in L3). This family was considered for a deliberate emittance exchange between the two transverse planes or for compensation of the linear coupling resonance, under the assumption of equal integer tunes, when the PSB was built. It can not be used for compensation at the working point $Q_x = 4.17$ and $Q_y = 5.23$, because the sum compensation vector vanishes. However, the results of the first resonance driving term measurement campaign strongly influenced the decision to restart the PSB in 2004 with a new working point in a working area as initially foreseen ($Q_x = 4.17$ and $Q_y = 4.23$). This skew quadrupole family is now in use.

- One zero harmonic octupole family (ONOH0, one element per period in L3) for *Landau Damping* [15]. Since this is not an issue in the PSB, the zero harmonic octupoles are not powered.
- Normal and skew octupoles: These multipoles are not used in standard operation. In the existing compensation scheme only resonances up to third order are considered and compensated, thus octupoles are not required.

4.3 The new acquisition system

The beam position signals from two PUs are needed to construct the turn-by-turn complex signal. For this purpose a new acquisition system was installed to record transverse turn-by-turn beam position over typically 1000 consecutive turns in the PSB.

During the shutdown 2002/03 the standard closed orbit PUs in rings 1 and 2, periods 5 and 6 were equipped with new head amplifiers to increase the bandwidth², thus leading to proper beam position signals in both planes. The five electrode signals from each of the two PUs are amplified and passed onto a passive hybrid circuit to match the impedances and to build the horizontal and vertical delta signals. The signals are further transferred to the fast digitiser on separate channels. The digitiser simultaneously samples all selected input channels following a trigger coming from the control system. Data were recorded with two 8-bit 4 channel Acqiris digitiser modules [17]. The use of a memory extension of 2 MS/channel enabled data taking over 4 ms at a sampling frequency of 500 MS/s. Hence approximately 2500 turns could be stored at a revolution time $\tau_{rev} \approx 1.6 \mu s$ at injection. Fig. 4.6 gives an overview of the whole acquisition system.

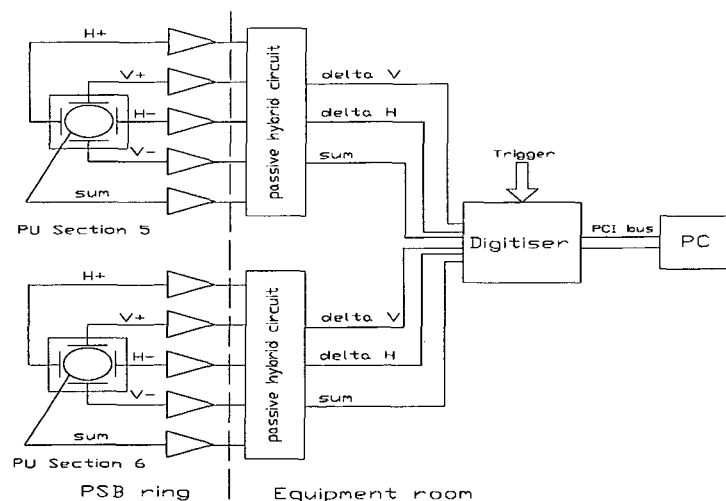


Figure 4.6: Schematic view of the multi-turn beam position acquisition system.

²The standard closed orbit PUs are designed only for orbit measurements and not for turn-by-turn beam position acquisition.

The Acqiris digitiser with the two modules is shown in Fig. 4.7.

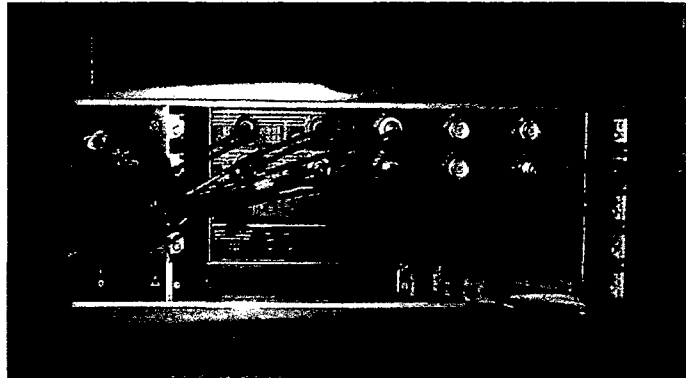


Figure 4.7: *Crate with two Acqiris digitiser modules.*

The typical appearance of the digitised raw data sum signal and the corresponding vertical delta signal is presented in Figs. 4.8 and 4.9. One notes from the vertical delta signal that the tune is close to a third integer value.

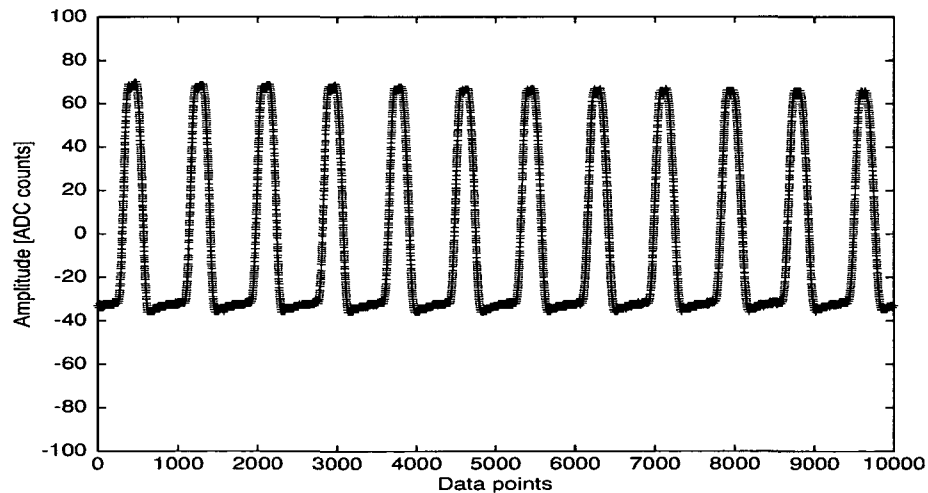


Figure 4.8: *Sum signal over 10000 data points, corresponding to 12 turns.*

The digitised signals are further processed with the so called Control and Processing Program (CaP) [18]. This program controls the digitiser, provides a graphical user interface and converts the digital data into real beam position. The user has to define the position of the first bunch and determine an observation window. This is done with the sum signal. The same window is then applied to the horizontal and vertical delta signals. The summation over all digitised data points within this window (corrected by a calculated offset) yields the sum and

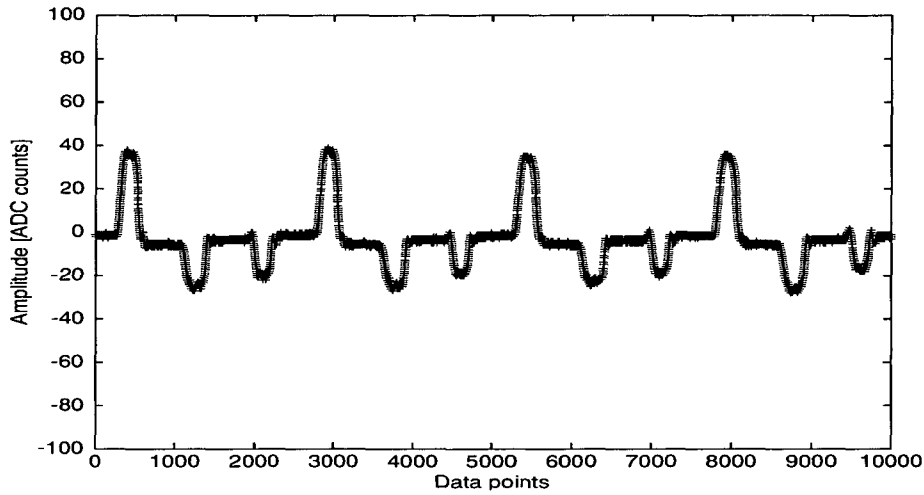


Figure 4.9: Vertical delta signal for 12 turns.

delta values for each turn. The relation Δ/Σ will then give the final beam position. Fig. 4.10 shows a typical transverse beam position signal over 1000 turns. The normalised oscillation amplitude is plotted against the number of turns. The observation period corresponds to approximately 1.6 ms. At injection the amplitude is large, the signal becomes smaller with time due to decoherence processes.

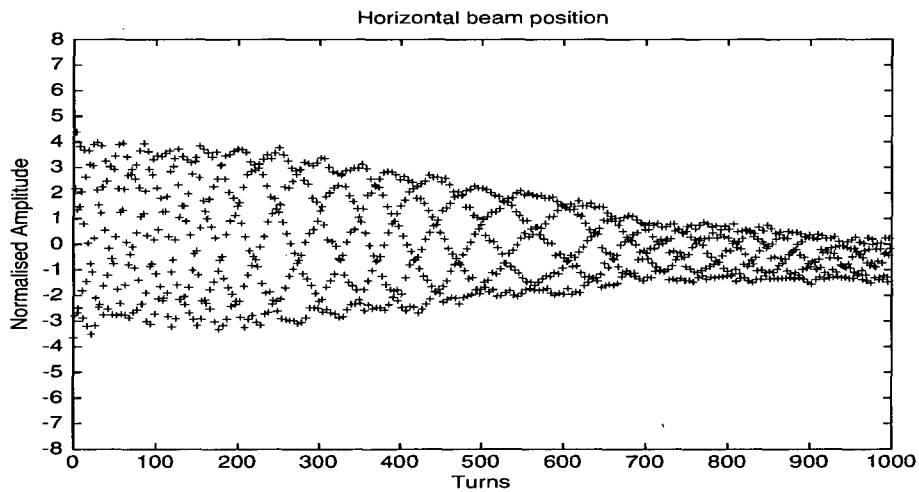


Figure 4.10: Characteristic beam position signal over 1000 turns.

4.4 Measurement set-up

For the measurement of resonance driving terms, the quality of the transverse beam position signals plays an important role. In principle two basic measurement conditions are necessary for the analysis of the transverse particle motion:

1. The oscillation amplitude of the beam has to be reasonably large (some mm).
2. The decoherence of the signal has to be avoided.

The former is normally achieved with a kicker, the latter with chromaticity correction in both planes.

In the case of the PSB, no proper kicker is available, hence *injection mis-steering* (a deliberate deflection of the beam at injection) has to be used to excite the beam. As a consequence only the first few thousand turns after injection into the machine could be analysed, limiting the studies to injection energy (50 MeV).

The decoherence of the beam position signals in both planes due to chromaticity (see Section 3.5) is normally avoided by properly correcting the chromaticities with two independent sextupole families. The PSB is equipped with only one such a family, thus the signal decoherence in one of the transverse planes is unavoidable. The compensation in one plane leads to a degradation of the signal quality in the other plane. This is a further important restriction for the measurement of resonance driving terms, especially if coupling resonances are considered, where high signal quality in both planes is needed.

To obtain proper signals, despite these limitations, the following adjustments on a special 50 MeV flat (no acceleration) machine development (MD) cycle were done:

1. Only one third of the ring was filled to obtain a quasi-bunched beam containing 1 to $2 \cdot 10^{11}$ protons.
2. In order to conserve the bunch and consequently avoid longitudinal debunching³, the RF was already switched on at injection and the beam was injected into the “waiting” bucket.
3. Horizontal and/or vertical injection mis-steering was used to obtain a sufficiently large oscillation amplitude.
4. The chromaticity was adjusted either to zero in one plane or to reasonably low values in both planes when coupling resonances were considered.

³Without RF, the particles would be distributed around the whole circumference of the ring after a small number of turns due to the particles' momentum spread.

4.5 Basic procedure to determine resonance driving terms

With the above mentioned set-up for the PSB the following procedure was applied to measure and compensate the bare machine resonance driving terms:

1. For each measurement only a single resonance was considered. Therefore the tunes were set close to this specific resonance condition. The chromaticities were adjusted to support the determination of the corresponding resonance driving term. Up to five measurements were done to obtain a useful statistic.
2. The measured normalised beam positions Z_2 allowed to reconstruct the divergence Z'_1 using the general transfer matrix for normalised coordinates (Eq. 2.36),

$$\begin{pmatrix} Z_2 \\ Z'_2 \end{pmatrix} = \begin{pmatrix} \cos(\Delta\mu) & \sin(\Delta\mu) \\ -\sin(\Delta\mu) & \cos(\Delta\mu) \end{pmatrix} \cdot \begin{pmatrix} Z_1 \\ Z'_1 \end{pmatrix}, \quad (4.1)$$

where $\Delta\mu$ is the phase advance between the two PUs. With the experimental set-up in the Booster, the phase advance is around 95° and 120° in the horizontal and vertical plane respectively.

3. *SUSSIX*, a computer code for frequency analysis of non-linear betatron motion [9], was used to perform a FFT of the normalised phase space. By means of interpolation a high precision tune determination is achieved [22]. The accuracy of the tune corresponds to $1/N^2$, where N is the number of analysed turns.
4. Resonance strength and phase were calculated using the relations in Tables 3.1 and 3.2.
5. Reference measurements with a defined multipole excitation were done for two reasons:
 - To verify that the whole acquisition system is working properly and provides the right results.
To exceed the bare machine component, a multipole located in a high β_z region was excited. If the bare machine contribution is then subtracted, the obtained resonance phase has to agree with theoretical predictions and simulations for the given multipole excitation.
 - For calibration purposes.
Reference measurements with a known multipole excitation are mandatory to deduce the correct strength of the bare machine excitation and subsequently the proper compensation currents.
6. With the knowledge of the strength $|h_{jklm}|$ and the phase ψ_{jklm} of the resonance driving term, the compensation settings for two independent multipoles were calculated. A general matrix for two compensation elements is derived from Eq. 3.68,

$$M = -\frac{q}{p} \frac{1}{2^n} \frac{1}{n!} \begin{pmatrix} n \\ l+m \end{pmatrix} \begin{pmatrix} j+k \\ j \end{pmatrix} \begin{pmatrix} l+m \\ l \end{pmatrix} \cdot \begin{pmatrix} \tilde{g}_{n(1)} \cdot l_{(1)} \cdot \beta_{x1}^{\frac{j+k}{2}} \beta_{y1}^{\frac{l+m}{2}} \cdot \cos \psi_{(1)} & \tilde{g}_{n(2)} \cdot l_{(2)} \cdot \beta_{x2}^{\frac{j+k}{2}} \beta_{y2}^{\frac{l+m}{2}} \cdot \cos \psi_{(2)} \\ \tilde{g}_{n(1)} \cdot l_{(1)} \cdot \beta_{x1}^{\frac{j+k}{2}} \beta_{y1}^{\frac{l+m}{2}} \cdot \sin \psi_{(1)} & \tilde{g}_{n(2)} \cdot l_{(2)} \cdot \beta_{x2}^{\frac{j+k}{2}} \beta_{y2}^{\frac{l+m}{2}} \cdot \sin \psi_{(2)} \end{pmatrix} \quad (4.2)$$

where \tilde{g}_n represents the n th order gradient of the multipole magnets per ampère. The suffixes (1) and (2) indicate the two compensation elements. The angles ψ , obtained with the single particle tracking code SixTrack [19] and SUSSIX, represent the resonance phases of the correction elements with respect to the position of the PU. The compensation currents I_1 and I_2 for two independent multipoles were then calculated with:

$$\begin{pmatrix} I_1 \\ I_2 \end{pmatrix} = M^{-1} \cdot \begin{pmatrix} |h_{jklm}| \cdot \cos \psi_{jklm} \\ |h_{jklm}| \cdot \sin \psi_{jklm} \end{pmatrix}. \quad (4.3)$$

7. To verify the correctness of the calculated compensation currents, the measurements were repeated. In case of not fully satisfying results (resonance line still visible), the procedure was repeated in an iterative way to reveal the most efficient compensation values.

4.6 Basic considerations on beam position signals

As mentioned earlier, the signal quality plays an important role for resonance driving term studies. In this section, phenomena like decoherence processes and tune instabilities observed at the PSB are discussed. These effects make the measurements and the compensation of resonance driving terms more difficult.

Influence of chromaticity PUs record the turn-by-turn transverse beam position of the centroid of the beam. As introduced in Section 3.5 the beam position signals are influenced by decoherence processes. The two main sources are amplitude detuning and chromaticity. In this paragraph, the consequences of chromaticity are presented. The horizontal beam position signal was considered. To reduce coupling effects between the transverse planes, the vertical injection mis-steering was set to zero. The tunes were placed into an area free of low order resonances ($Q_x \approx 4.21$, $Q_y \approx 5.29$). To see the influence of chromaticity on the signals, the sextupole family for chromaticity correction (XNOH0) was powered with different currents. First the situation for the bare machine ($Q'_x \approx -3.5$ and $Q'_y \approx -9.3$) was investigated. Fig. 4.11 shows the observed horizontal beam position signal.

The fast decoherence of the signal and the re-bunching after approximately 300 turns is clearly visible and indicates a synchrotron tune of $Q_s \approx 1/300$. The signal totally decays after about 2000 turns. Fig. 4.12 illustrates the case when the XNOH0s are powered with +40 A, leading to a small remaining horizontal chromaticity of $Q'_x \approx -0.7$. The amplitude of the signal remains constant. No decoherence, neither due to chromaticity nor due to amplitude detuning, takes place.

The situation for a vertically corrected chromaticity is presented in Fig. 4.13. For this the XNOH0s were powered with -50 A. As a consequence, the horizontal chromaticity increases to $Q'_x \approx -7.1$. Decoherence and re-bunching due to the combined effect of chromaticity and synchrotron motion are observed. The signal totally decoheres after approximately 1000 turns.

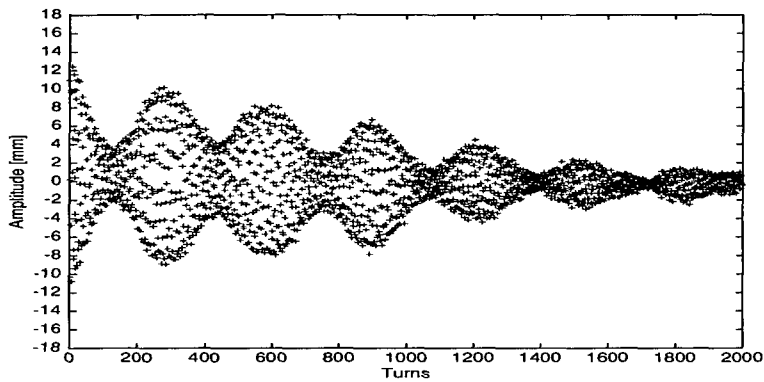


Figure 4.11: Horizontal beam position signal for 2000 turns with natural chromaticity, $Q'_x \approx -3.5$.

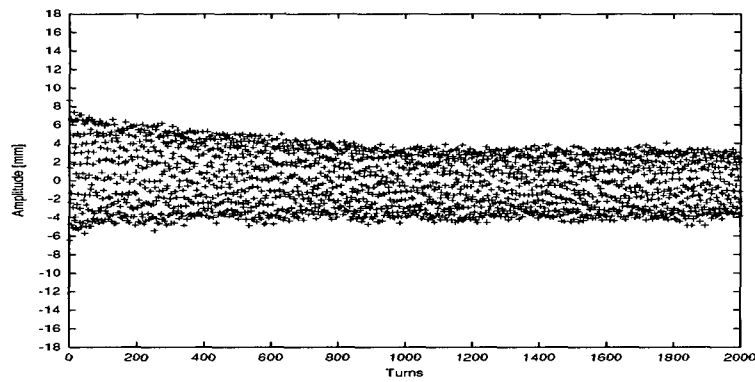


Figure 4.12: Horizontal beam position signal for 2000 turns with $Q'_x \approx -0.7$ ($I_{XNOH0} = +40$ A).

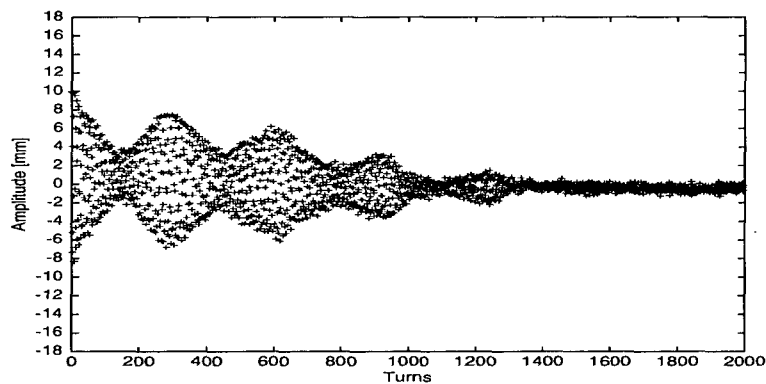


Figure 4.13: Horizontal beam position signal for 2000 turns with $Q'_x \approx -7.1$ ($I_{XNOH0} = -50$ A).

Decoherence of the PU signal The vertical beam position signal obtained for natural chromaticities is shown in Fig. 4.14.

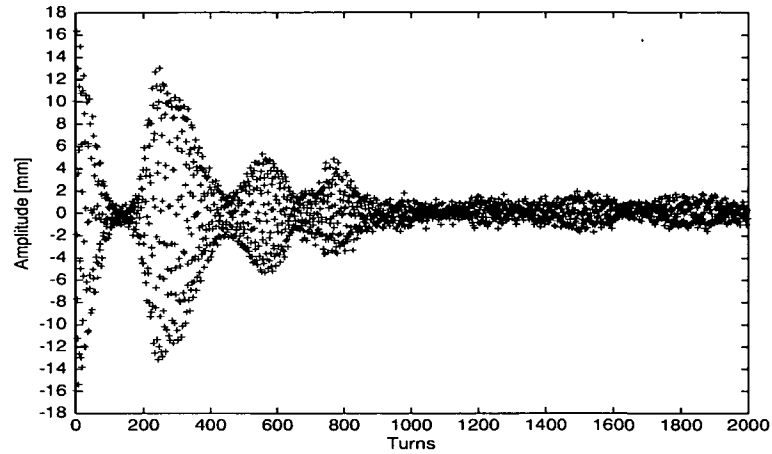


Figure 4.14: Vertical beam position signal for 2000 turns with natural chromaticity $Q'_y \approx -9.3$.

Without synchrotron motion the re-bunching of the once decohered transverse beam position signal does not take place. Fig. 4.15 presents the decoherence process during the first 150 Turns of Fig. 4.14 in more detail.

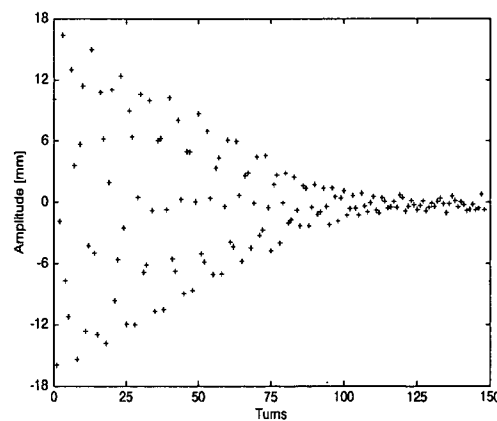


Figure 4.15: Decoherence of the vertical beam position signal for $Q'_y \approx -9.3$.

The decoherence time is expressed as [4]:

$$t_{decoh} = \frac{t_{rev}}{\Delta Q} \quad (4.4)$$

For a natural chromaticity of $Q'_y \approx -9.3$ and a momentum deviation of $\Delta p/p = \pm 0.001$ the number of turns corresponding to the decoherence time yields 108 turns and therefore fits the observations very well.

Instability of the tunes in the PS Booster For the analysis of resonance driving terms, the tune stability over a sufficient number of turns is of importance. Fluctuations of the tune widen and lower the tune peak in the Fourier spectra. A comparison of measured and simulated amplitudes of spectral lines is therefore problematic and small resonance lines tend to disappear in the background noise.

After injection into the PSB, the tunes are not entirely stable. However, these fluctuations do not harm machine operation. For the determination of resonance driving terms, in general the first 200 turns after injection⁴ were considered as a proper observation period. Within this period the tunes tend to be stable and the number of turns is sufficiently large to obtain Fourier spectra with an adequate resolution. Fig 4.16 shows typical tune fluctuations over an observation period of 2000 turns. The tune was determined in 10 steps of 200 turns. The deviation for the tune was estimated to $\sigma \approx 0.002$ in both planes.

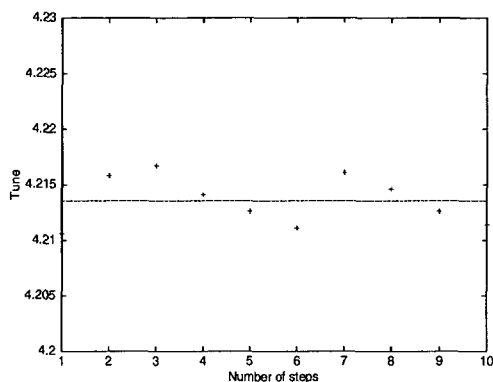


Figure 4.16: *Tune values over an observation period of 2000 turns, analysed in 10 steps of 200 turns.*

⁴In fact, the first 20 turns after injection were omitted because of transient effects of the PU electronics.

Chapter 5

Measurement and compensation of second order resonance driving terms

5.1 Second order contributions to the Fourier spectra

According to the perturbative treatment of the transverse particle motion (Section 3.1) the total Hamiltonian H (Eq. 3.15) is expressed as the sum of the linear Hamiltonian H_0 and H_1 , containing all the contributions from non-linear elements. It was assumed that the normal coefficients B_1 and B_2 are already contained in the normalised dipole strength $\rho_0(s)$ and normalised quadrupole strengths $k(s)$. The skew coefficient A_1 (vertical dipole) was set to zero. When second order resonances are considered, one refers to additional contributions from linear elements, like normal quadrupoles (introduced with coefficient B_2^* in Section 3.2) and skew quadrupoles (coefficient A_2), which couples the two transverse planes. The Hamiltonian H_1^* (perturbing term due to linear contributions) is then given by,

$$H_1^* = -\frac{q}{p_0} \text{Re} \left[\frac{1}{2} (B_2^* + iA_2) \cdot (x + iy)^2 \right], \quad (5.1)$$

and can be rewritten as,

$$H_1^* = -\frac{q}{2p_0} [B_2^*(x^2 - y^2) - 2A_2xy]. \quad (5.2)$$

For second order resonances, the Hamiltonian coefficients h_{jklm} (Eq. 3.68) which fulfill $n = j + k + l + m = 2$ are of interest. From Tables 3.1 and 3.2 the associated spectral lines are found. Horizontal lines appear for $j \neq 0$ and vertical lines for $l \neq 0$. Tables 5.1 and 5.2 show all the concerned Hamiltonian terms as well as the appendant spectral lines in the Fourier spectra due to normal quadrupole contributions.

Driving Term	Resonance	Lines Hor.	Lines Ver.
h_{2000}	(2,0)	(-1,0)	-
h_{0200}	(2,0)	-	-

Table 5.1: Driving terms, resonances and spectral lines due to the normal quadrupole term x^2 .

Driving Term	Resonance	Lines Hor.	Lines Ver.
h_{0020}	(0,2)	-	(0,-1)
h_{0002}	(0,2)	-	-

Table 5.2: Driving terms, resonances and spectral lines due to the normal quadrupole term y^2 .

The Hamiltonian terms related to skew quadrupoles and the corresponding spectral lines are presented in Tab. 5.3.

Driving Term	Resonance	Lines Hor.	Lines Ver.
h_{1010}	(1,1)	(0,-1)	(-1,0)
h_{0101}	(1,1)	-	-
h_{1001}	(1,-1)	(0,1)	-
h_{0110}	(1,-1)	-	(1,0)

Table 5.3: Driving terms, resonances and spectral lines due to the skew quadrupole term xy .

From the tune diagram of the PSB for high intensity beams (Fig. 4.5) one notes that the vertical second order resonance $2Q_y = 11$, driven by the Hamiltonian term h_{0020} , is covered by particles. In standard operation, this resonance has to be compensated at the start of the acceleration for a satisfactory performance of the PSB.

The linear coupling difference resonance $Q_x - Q_y = -1$ is not compensated in normal operation. Instead, it is deliberately excited during the multi-turn injection to transfer some of the horizontal oscillation to vertical to avoid beam losses. Thus, the knowledge of the bare machine driving term is of importance to adjust the skew quadrupoles for the emittance exchange properly. This resonance tends to be strong and offers a good possibility to gain experience with the whole acquisition system. Therefore it was intensively treated at the beginning of the measurement campaign [25].

The presented results of the following sections refer to ring 1 of the PSB. No measurements were performed at ring 2 during the run 2003 due to hardware problems with the PU electronics.

5.2 Linear coupling resonances

For the investigation of linear coupling, difference and sum resonances have to be taken into account. For simultaneous compensation of both types of resonances, four independent skew quadrupoles are required. The tune diagram of the PSB reveals, that the difference resonance $Q_x - Q_y = -1$ is more important than the sum resonances $Q_x + Q_y = 9$ or 10 . Since the PSB is equipped with only two skew quadrupole families, it is reasonable to concentrate on and compensate the difference resonance. Effects of e.g. calculated compensation currents on the sum resonance, were considered too.

To determine the linear coupling difference resonance driving term h_{1001} , the tunes were set close to resonance condition: $Q_x \approx 4.20$, $Q_y \approx 5.14$. The chromaticities were adjusted to be equal ($Q'_x \approx Q'_y \approx -5.3$) because both, the horizontal and vertical particle motion are of interest if linear coupling is considered.

According to Tab. 3.1 the strength $|h_{1001}|$ and phase ψ_{1001} of the resonance driving term are related to the horizontal spectral line (0, 1) as presented in Tab. 5.4.

Driving Term		Horizontal Spectral Line
Line		(0, 1)
Amplitude	$ h_{1001} $	$\sqrt{2I_y} \frac{ h_{1001} }{\sin(\hat{\phi})} = a_{x1}$
Phase	ψ_{1001}	$\psi_{1001} + \psi_{y0} - \frac{\pi}{2} + \text{sgn}(\hat{\phi})\left(\frac{\pi}{2} - \hat{\phi} \right) = \phi_{x1}$
where $\hat{\phi} = \pi[\nu_x - \nu_y]$		

Table 5.4: Relation between the (0,1) spectral line and amplitude and phase of the h_{1001} Hamiltonian term.

The vertical Fourier spectrum offers as well the opportunity to deduce the driving terms. According to Tab. 5.3 the driving term h_{0110} (being the complex conjugate of h_{1001}) is related to the spectral line (1, 0). Strength $|h_{0110}|$ and phase ψ_{0110} are linked to the measured amplitude a_{y1} and phase ϕ_{y1} as shown in Tab. 5.5.

Driving Term		Vertical Spectral Line
Line		(1, 0)
Amplitude	$ h_{0110} $	$\sqrt{2I_x} \frac{ h_{0110} }{\sin(\hat{\phi})} = a_{y1}$
Phase	ψ_{0110}	$\psi_{0110} + \psi_{x0} - \frac{\pi}{2} + \text{sgn}(\hat{\phi})\left(\frac{\pi}{2} - \hat{\phi} \right) = \phi_{y1}$
where $\hat{\phi} = \pi[\nu_y - \nu_x]$		

Table 5.5: Relation between the (1,0) spectral line and amplitude and phase of the h_{0110} Hamiltonian term.

From Tables 5.4 and 5.5 one concludes:

$$|h_{1001}| = \frac{a_{x1}}{a_{y0}} \sin(|\hat{\phi}|), \quad (5.3)$$

$$|h_{0110}| = \frac{a_{y1}}{a_{x0}} \sin(|\hat{\phi}|), \quad (5.4)$$

$$\psi_{1001} = \phi_{x1} - \psi_{y0} + \frac{\pi}{2} - \text{sgn}(\hat{\phi})\left(\frac{\pi}{2} - |\hat{\phi}|\right), \quad (5.5)$$

$$\psi_{0110} = \phi_{y1} - \psi_{x0} + \frac{\pi}{2} - \text{sgn}(\hat{\phi})\left(\frac{\pi}{2} - |\hat{\phi}|\right), \quad (5.6)$$

where $a_{x0} = \sqrt{2I_x}$ and $a_{y0} = \sqrt{2I_y}$ are the amplitudes of the horizontal and the vertical tune line respectively. According to theory $\psi_{0110} = -\psi_{1001}$.

Multiplying Eqs. 5.3 and 5.4 with each other, extracting the square root and taking into account that $|h_{1001}| = |h_{0110}|$, one obtains a formula containing the amplitude information from both spectra:

$$|h_{1001}| = \sqrt{\frac{a_{x1} a_{y1}}{a_{y0} a_{x0}}} \cdot \sin(|\hat{\phi}|). \quad (5.7)$$

5.2.1 Measurement of the bare machine excitation

Fig. 5.1 shows the horizontal and vertical Fourier spectrum obtained from measurements of the bare machine. The spectra are normalised to the amplitude of the tune line (indicated by (1, 0) and (0, 1) in the horizontal and vertical spectrum respectively). In each Fourier spectrum two

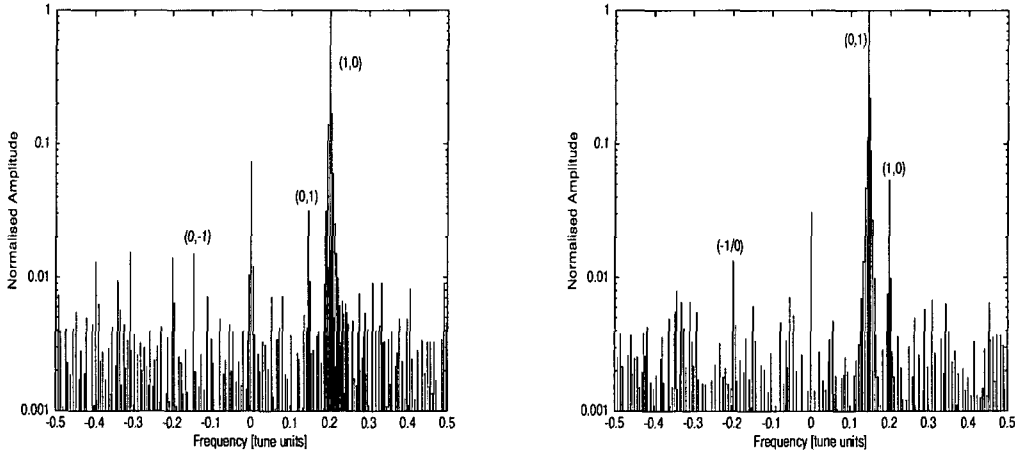


Figure 5.1: Horizontal and vertical Fourier spectrum for the bare machine with tunes close to the $Q_x - Q_y = -1$ resonance condition.

additional spectral lines are indicated. The spectral line (0, 1) in the horizontal spectrum and the line (1, 0) in the vertical correspond to the driving term h_{1001} . The lines (0, -1) and (-1, 0) are related to the sum resonance or the h_{1010} driving term. When analysing typically 200 turns, an accuracy of $1/N^2 = 2.5 \cdot 10^{-5}$ for the spectral lines in terms of tune units is obtained. The number of turns is a compromise between a satisfying accuracy and the decoherence of the beam position signals in time.

The line with zero frequency

The Fourier spectra always show a large line at the zero frequency position. The different effects that cause this line are:

- Beam off-sets. The off-set in both planes was subtracted from the beam position data, but slight drifts in the signal lead to remaining contributions.
- Hamiltonian terms h_{jklm} which fulfill the condition for the zero frequency line (e.g. for the horizontal plane, $1 - j + k = 0$ and $m - l = 0$). Therefore either dipoles or higher order multipoles (e.g. sextupoles, octupoles) contribute to this line.

According to theory [20], the line with zero frequency is not affected neither by amplitude detuning nor by chromaticity and therefore tends to be large compared to the other spectral lines.

With the results obtained from measurements¹, Eq. 5.7 yields for the difference resonance:

- $|h_{1001}| = 7.1 \pm 0.1 \cdot 10^{-3}$.

The resonance phase was calculated with the information from both spectra (Eqs. 5.5 and 5.6) yielding, $\psi_{1001} = 295.6^\circ \pm 5.9^\circ$ and $\psi_{0110} = 90.0^\circ \pm 2.0^\circ$. The difference of the two phases ($-\psi_{0110}$ and ψ_{1001}) is roughly 25° . The averaged resonance phase for the bare machine is then given by,

- $\psi_{1001} = 282.8^\circ \pm 5.2^\circ$.

Investigation of the linear coupling sum resonance driving term h_{1010} yields,

- $|h_{1010}| = 12.7 \pm 0.6 \cdot 10^{-3}$, $\psi_{1010} = 172.9^\circ \pm 6.9^\circ$.

One notes that the driving term of the sum resonance is larger than the one of the difference resonance. This does not disagree with fact that the observed spectral lines for the sum resonance appear smaller. The Hamiltonian terms consider already the distance of the tunes to the resonance condition. However, the real effect on the phase space and hence on the particle trajectory at this specific working point is indicated by the generating function term f_{jklm} . As shown in Section 3.4.4 the relation between the generating function term and the Hamiltonian term can be written as,

$$|f_{jklm}| = \frac{|h_{jklm}|}{2\sin(|\hat{\phi}|)}, \quad (5.8)$$

where $\hat{\phi} = \pi[(j - k)\nu_x + (l - m)\nu_y]$ is a measure for the distance of the working point to the resonance condition. The result $|f_{1001}|/|f_{1010}| \approx 3.15$ shows, that as expected the virtual impact of the difference resonance is more than a factor three larger due to the vicinity of the tunes to the difference resonance.

Fig.5.2 shows beam intensity against time (in ms) while crossing the $Q_x - Q_y = -1$ resonance without compensation. The corresponding tune line is presented in Fig. 5.3. The working point is moved from the upper left corner to the lower right corner and crosses additionally the third

¹Averaged resonance strength and phase, in general five measurements were performed for the bare machine.

order coupling resonance $2Q_x - Q_y = 3$. Injection into the machine takes place at 270 ms. The third order resonance is crossed 100 ms and the linear coupling resonance 330 ms after injection. No losses occur during the crossing of both resonances. The beam is then ejected at about 780 ms.

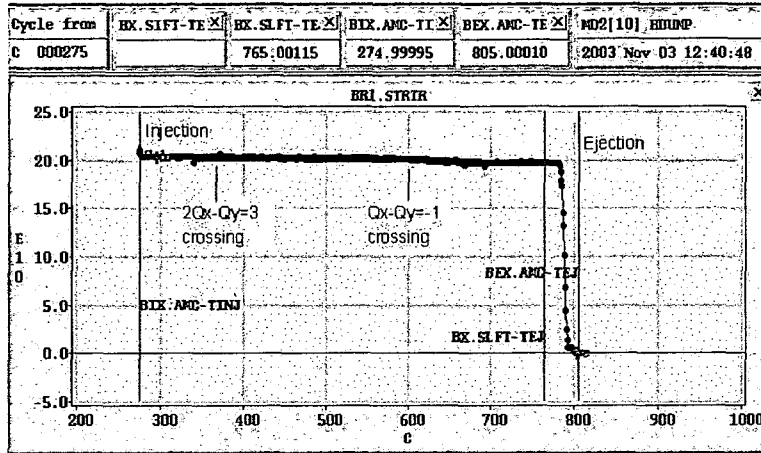


Figure 5.2: Beam intensity while crossing the coupling resonances $2Q_x - Q_y = 3$ and $Q_x - Q_y = -1$ without compensation.

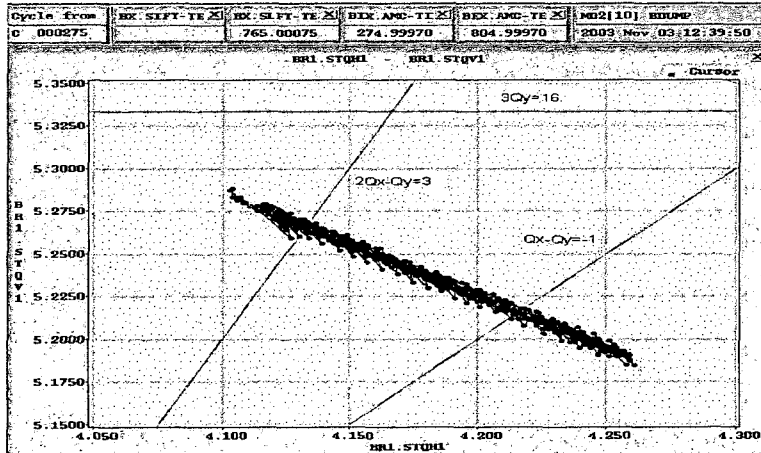


Figure 5.3: Tune line, the working point is moved from the upper left corner to the lower right corner, two coupling resonances are crossed.

5.2.2 Reference measurements

Reference measurements with defined skew quadrupoles were done to verify that the whole acquisition system is working properly. If the bare machine contribution is subtracted, the obtained resonance phase has to agree with theoretical predictions and simulations for the given multipole excitation. The measured and theoretical resonance strength can still be different because of the decoherence of the beam position signals.

The reference measurements are further used for calibration purposes to deduce the correct strength of the bare machine excitation and subsequently the proper compensation currents.

The PSB has two independent skew quadrupole families, each consisting of 2 elements, located in the straight sections L3 (Table 4.1). Measurements with both families were carried out.

Excitation with the skew quadrupole family QSK210L3

The skew quadrupoles were powered with $I_{QSK210L3} = 35A$. Fig. 5.4 shows the horizontal and vertical Fourier spectrum for the deliberate excitation. The enlargement of the resonance lines compared to the bare machine excitation is evident. One notes that the horizontal tune and the spectral line $(0, 1)$ have similar amplitudes. This is explained by the fact, that the vertical oscillation amplitude is larger than the horizontal one. Since the amplitude of the resonance spectral line is proportional to the oscillation amplitude of the other plane, the observed resonance line in the horizontal spectrum is larger than the one in the vertical spectrum.

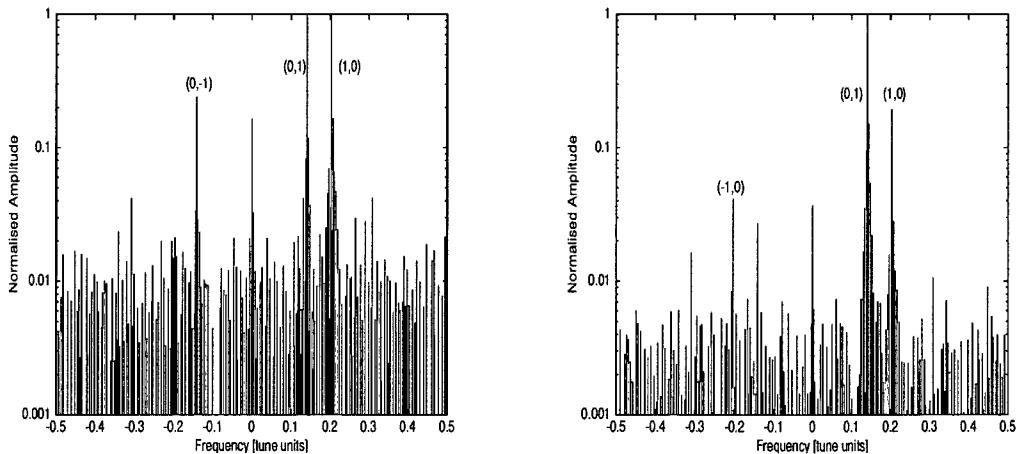


Figure 5.4: Horizontal and vertical Fourier spectrum for a deliberate excitation of the resonance with $I_{QSK210L3} = 35A$.

With the results from the measurements, Eqs. 5.5 to 5.7 yield,

- $|h_{1001}| = 8.33 \pm 0.03 \cdot 10^{-2}$,
- $\psi_{1001} = 123.5^\circ \pm 1.3^\circ$,
- $\psi_{0110} = 123.7^\circ \pm 2.1^\circ$.

In this case the measured resonance phases are similar. For the bare machine an agreement only within 25° was found. The resonance strength for the excitation is more than a factor ten larger than for the bare machine, hence noise contributions to the spectral lines are of less importance, leading to a better precision of the measurements.

To obtain the correct strength and phase for the skew quadrupole family, the bare machine excitation has to be subtracted. This result was then compared with simulations performed with the single particle tracking code SixTrack and SUSSIX²:

- Measurements: $|h_{1001}| = 9.00 \pm 0.02 \cdot 10^{-2}$, $\psi_{1001} = 122.0^\circ \pm 1.1^\circ$
- Simulation: $|h_{1001}| = 10.04 \cdot 10^{-2}$, $\psi_{1001} = 302.7^\circ$

Taking into account the decoherence processes, which are not considered in the simulations, the agreement in resonance strength is excellent. Furthermore the measured resonance phase is exactly opposite to expectations, indicating an inversed polarity of the magnets.

Table 5.6 summarises the obtained results for the linear coupling difference resonance.

	Bare machine	Reference measurements	Simulation
$ h_{1001} $	$0.71 \pm 0.01 \cdot 10^{-2}$	$9.00 \pm 0.02 \cdot 10^{-2}$	$10.04 \cdot 10^{-2}$
ψ_{1001}	$282.8^\circ \pm 5.2^\circ$	$122.0^\circ \pm 1.1^\circ$	302.7°

Table 5.6: Overview on resonance strengths and phases obtained for the bare machine and in case of excitation.

Fig. 5.5 shows the Fourier spectra obtained from the simulation. Compared to the measurements, the oscillation amplitude was considered to be equal in both planes. One notes that additional spectral lines, $(-1, 0)$ in the horizontal and $(0, -1)$ in the vertical spectrum, show up. These lines are driven by normal quadrupoles. The strong excitation of the skew quadrupoles leads to normal quadrupole contributions according to second order perturbation theory and therefore excite the corresponding resonances.

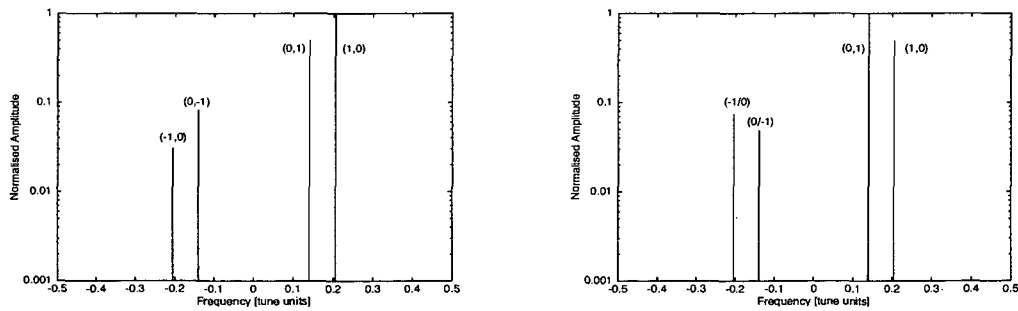


Figure 5.5: Horizontal and vertical Fourier spectra in case of the deliberate excitation with $I_{QSK210L3} = 35A$ obtained from the simulation.

²The simulation was done with $Q_x = 4.205$, $Q_y = 5.14$.

The evaluation of the sum resonance yields,

- Measurements³: $|h_{1010}| = 7.42 \pm 0.35 \cdot 10^{-2}$, $\psi_{1010} = 113.0^\circ \pm 1.1^\circ$
- Simulation: $|h_{1010}| = 7.03 \cdot 10^{-2}$, $\psi_{1010} = 300.8^\circ$

The agreement of the resonance strengths is convincing and the comparison of the resonance phases indicates again the inversed polarity of the skew quadrupoles.

Table 5.7 presents the results for the linear coupling sum resonance.

	Bare machine	Reference measurement	Simulation
$ h_{1010} $	$1.27 \pm 0.06 \cdot 10^{-2}$	$7.42 \pm 0.35 \cdot 10^{-2}$	$7.03 \cdot 10^{-2}$
ψ_{1010}	$172.9^\circ \pm 6.9^\circ$	$113.0^\circ \pm 1.1^\circ$	300.8°

Table 5.7: Overview on resonance strengths and phases obtained for the bare machine and in case of excitation.

Excitation with the skew quadrupole family QSK614L3

The linear coupling resonance was excited with the second skew quadrupole family *QSK614L3*. After subtraction of the bare machine excitation the following results were obtained for the difference resonance and compared to simulation:

- Measurements: $|h_{1001}| = 8.90 \pm 0.10 \cdot 10^{-2}$, $\psi_{1001} = 34.4^\circ \pm 1.3^\circ$
- Simulation: $|h_{1001}| = 10.04 \cdot 10^{-2}$, $\psi_{1001} = 38.6^\circ$

The results show again an excellent agreement in terms of resonance strength and phase. The measured and simulated phases agree within 5° . The polarity of this skew quadrupole family is as expected. During the shut down period the polarity of both families was verified and indeed confirmed the observations from the measurements.

The results presented so far, show that the acquisition system enables high precision determination of the linear coupling resonance driving terms. In the following section the way to derive the proper magnet currents for compensation is explained and the efficiency of these settings is discussed.

³The bare machine excitation is already subtracted.

5.2.3 Compensation of the linear coupling difference resonance

As the PSB has only two independent skew quadrupole families, the linear coupling difference resonance was compensated and the effects of the compensation currents on the sum resonance analysed. Rewriting Eq. 4.3 for the linear coupling resonance yields,

$$\begin{pmatrix} I_1 \\ I_2 \end{pmatrix} = M^{-1} \cdot \begin{pmatrix} |h_{1001}| \cdot \cos \psi_{1001} \\ |h_{1001}| \cdot \sin \psi_{1001} \end{pmatrix}, \quad (5.9)$$

where,

$$M = -\frac{q}{4p_0} \begin{pmatrix} \tilde{g}_{2(1)} \cdot l_{(1)} \cdot \beta_{x1}^{\frac{1}{2}} \beta_{y1}^{\frac{1}{2}} \cdot \cos \psi_{(1)} & \tilde{g}_{2(2)} \cdot l_{(2)} \cdot \beta_{x2}^{\frac{1}{2}} \beta_{y2}^{\frac{1}{2}} \cdot \cos \psi_{(2)} \\ \tilde{g}_{2(1)} \cdot l_{(1)} \cdot \beta_{x1}^{\frac{1}{2}} \beta_{y1}^{\frac{1}{2}} \cdot \sin \psi_{(1)} & \tilde{g}_{2(2)} \cdot l_{(2)} \cdot \beta_{x2}^{\frac{1}{2}} \beta_{y2}^{\frac{1}{2}} \cdot \sin \psi_{(2)} \end{pmatrix}. \quad (5.10)$$

The quantity \tilde{g}_2 represents the skew quadrupole gradient per ampère. The angles ψ are the resonance phases of the correction elements with respect to the PU in period 5, obtained from simulations.

Using the corresponding values for the skew quadrupoles and the measured resonance strength and phase of the bare machine excitation (under consideration of a scaling factor obtained from the reference measurements) leads to,

- $I_{QSK210L3} = +2.65 \pm 0.15$ A (the opposite polarity is already included)
- $I_{QSK614L3} = +0.88 \pm 0.22$ A

Measurements were redone after having applied the calculated currents. The resonance strength was indeed reduced to $|h_{1001}| = 2.1 \pm 0.1 \cdot 10^{-3}$ or 30% of its initial value. The phase remained unchanged ($\psi_{1001} = 277.1^\circ \pm 21.0^\circ$). Therefore both current values were increased proportional to each other. New measurements were carried out with

- $I_{QSK210L3} = +3.6$ A
- $I_{QSK614L3} = +1.2$ A

leading to a further decrease in resonance strength to $|h_{1001}| = 1.7 \pm 0.1 \cdot 10^{-3}$ or 24% of the initial bare machine excitation. Fig. 5.6 shows the Fourier spectra when the skew quadrupoles are powered with the above mentioned currents. Compared to the spectra of the bare machine (Fig. 5.1), the reduction of the resonance lines is clearly visible. The horizontal resonance line is covered by the background, whereas the vertical still sticks out. Further iterations to reduce the remaining strength were not successful. One should notice that a resonance strength smaller than $1.0 \cdot 10^{-3}$ is not detectable due to the background noise. Fig. 5.7 shows the vectors created by the two skew quadrupole families, the bare machine excitation vector and the opposed compensation vector.

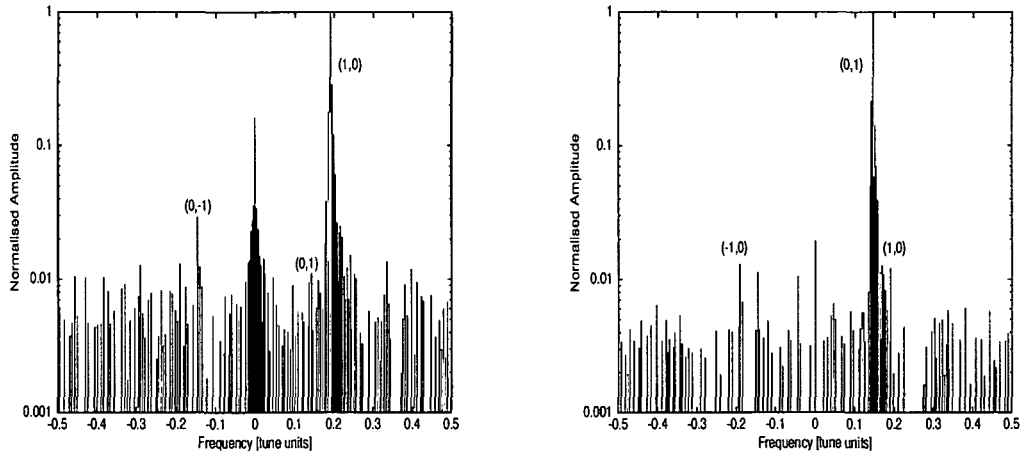


Figure 5.6: Horizontal and vertical Fourier spectrum with compensation currents $I_{QSK210L3} = 3.6$ A, $I_{QSK614L3} = 1.2$ A on.

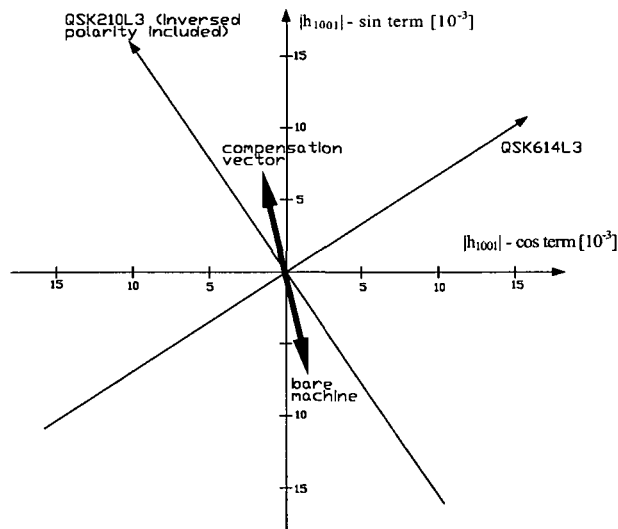


Figure 5.7: Excitation vectors for the skew quadrupole families $QSK210L3$ and $QSK614L3$ for the difference resonance, the bare machine and the opposed compensation (Tunes: $Q_x = 4.205$, $Q_y = 5.14$).

Effect of compensation settings on the sum resonance

From Fig. 5.8 one notes that the bare machine excitation and the compensation vector for the difference resonance add up to an increased driving term. In other words, the compensation of the difference resonance excites the sum resonance.

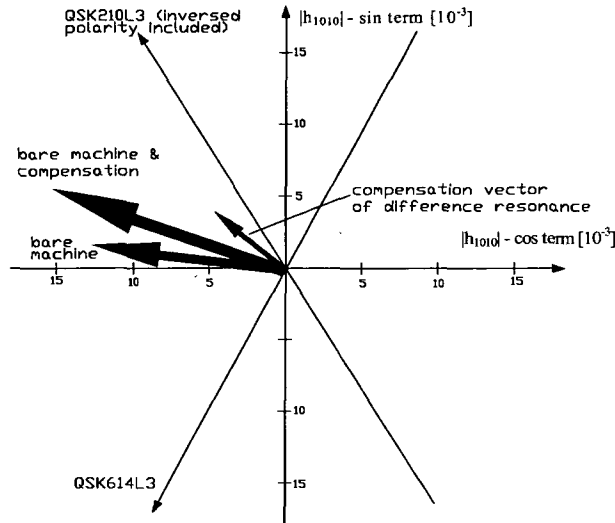


Figure 5.8: Excitation vectors of the skew quadrupoles for the sum resonance and the bare machine. The compensation vector of the difference resonance excites the sum resonance.

Fig. 5.6 clearly shows sum resonance spectral lines ((0,-1) and (-1,0)). The analysis of the data revealed an increase in resonance strength (from $|h_{1010}| = 1.27 \cdot 10^{-2}$ to $1.61 \cdot 10^{-2}$) and a change in resonance phase (from $\psi_{1010} = 172.9^\circ$ to 160.0°). The difference vector of these two results yields $|h_{1010}| = 0.47 \pm 0.14 \cdot 10^{-2}$ and $\psi_{1010} = 122.7^\circ \pm 17.8^\circ$ and has to agree with the simulation when the quadrupoles are powered with the compensation currents. Simulation gives $|h_{1010}| = 0.62 \cdot 10^{-2}$ and $\psi_{1010} = 140.0^\circ$ and therefore confirms the measurements.

Comparison of the beam position signals

Linear coupling leads to an energy exchange between the two transverse planes. The particle amplitude oscillates with an interchange frequency, depending on the separation of the uncoupled tunes and the coupling coefficient. Fig. 5.9 shows the horizontal (top) and vertical (bottom) beam position signal very close to the resonance condition for the bare machine. The vertical signal is shifted by -30 mm.

The amplitude exchange is clearly visible. It should be kept in mind that these signals are perturbed due to chromaticity in both planes and synchrotron motion of the particles.

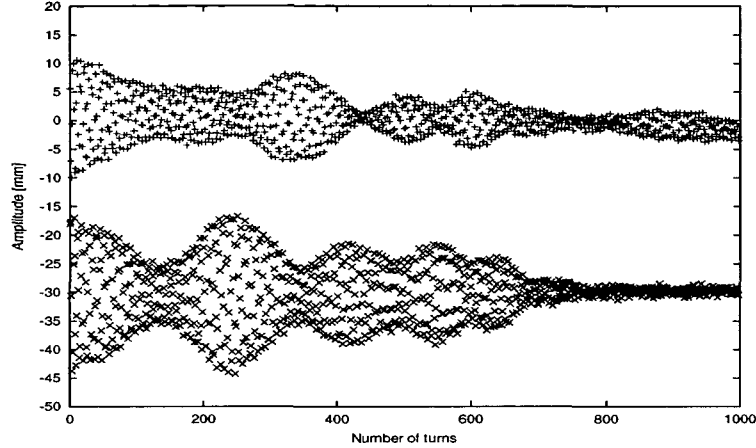


Figure 5.9: Horizontal (top) and vertical (bottom) beam position signal close to resonance condition for the bare machine.

The uncoupled tunes can not be measured directly in close vicinity to the coupling resonance, but two observable quantities can be determined, which depend on the tunes and on the coupling coefficient [21]. These quantities are the interchange period T , given by,

$$T = \frac{1}{f_{rev} \sqrt{\Delta^2 + |C|^2}} \quad (5.11)$$

and the modulation S , expressed as,

$$S = \frac{E_{min}}{E_{max}} = \frac{\Delta^2}{\Delta^2 + |C|^2}, \quad (5.12)$$

where f_{rev} is the revolution frequency, $\Delta = Q_x - Q_y$ is the separation of the uncoupled tunes and C is the coupling coefficient. E_{min} and E_{max} are the minimum and maximum excursions of the oscillation. The quantities T and S can be evaluated from Fig. 5.9. The interchange period corresponds to approximately 170 turns and the modulation can be assumed to 0.5 for the following estimations. Above equations can be transformed into,

$$|C| = \frac{1}{f_{rev} T} \sqrt{1 - S} \quad \text{and} \quad |\Delta| = \frac{\sqrt{S}}{f_{rev} T}, \quad (5.13)$$

to obtain expressions for the coupling coefficient and the tune separation.

With the mentioned assumptions and a revolution frequency $f_{rev} \approx 600$ kHz, above equations yield $|C| = |\Delta| = 4.2 \cdot 10^{-3}$. Operational difficulties for the tune measurement appear at around $|C/\Delta| = 1.0$. From the measurements, the tune separation was estimated to $|\Delta| = 5.5 \cdot 10^{-3}$.

The coupling coefficient is defined by,

$$|C| = \sqrt{C_q^2 + C_b^2}, \quad (5.14)$$

where C_q contains all the contributions from skew quadrupoles and C_b the contributions from axial fields. Since sources of axial fields are not expected in the PSB, this term is neglected. C_q is defined as,

$$C_q = \frac{R}{2\pi Q} \frac{1}{B\rho_0} \oint \left(\frac{\partial B_x}{\partial x} \right)_0 ds, \quad (5.15)$$

where R is the radius of the machine. If the perturbation is assumed to be from a single skew quadrupole, the integral can be replaced by the field gradient $(\partial B_x/\partial x)_0$ times the length l for this quadrupole. With the previous assumptions, the field gradient is calculated to,

$$\left(\frac{\partial B_x}{\partial x} \right)_0 = 1.6 \cdot 10^{-2} \frac{\text{T}}{\text{m}}. \quad (5.16)$$

This value corresponds to a skew quadrupole current, $I_{QSK} = 7.9$ A. Equating the absolute current for the calculated compensation settings yields $I_{QSK} = 7.6$ A. So even the rough estimation from the beam position behaviour agrees excellently with the results from the driving term measurements.

When the skew quadrupoles are powered with the compensation currents, no coupling between the planes should be left and therefore no amplitude exchange should be present. Fig. 5.10 shows the horizontal (top) and vertical (bottom) beam position signal in case of compensation. The observed oscillations are now due to the combined effect of chromaticity and synchrotron motion. Only at about 300 turns coupling is still observable, but in general no amplitude exchange is evident any more. The remaining coupling can be attributed to the remaining driving term after compensation and effects due to the linear coupling sum resonance.

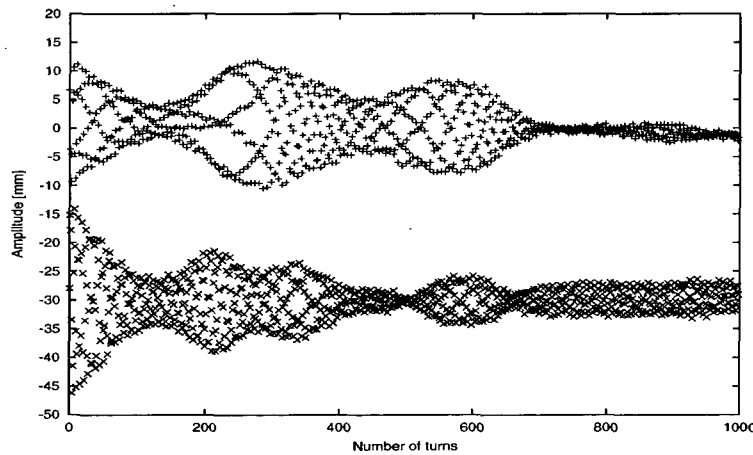


Figure 5.10: Horizontal (top) and vertical (bottom) beam position signal close to resonance condition with compensation settings turned on.

Stepwise compensation

With the knowledge of the resonance strength and phase of the bare machine excitation, the compensation currents for the skew quadrupoles were calculated. If the currents of these two families are changed stepwise in fractional amounts of the compensation values, the resonance phase has to remain constant. Fig. 5.11 shows the measured resonance strength over the skew quadrupole current (in fractional parts of the calculated compensation values; $I_{QSK210L3} = 3.6$ A and $I_{QSK614L3} = 1.2$ A correspond to 1 on the x axis). The “0” point on

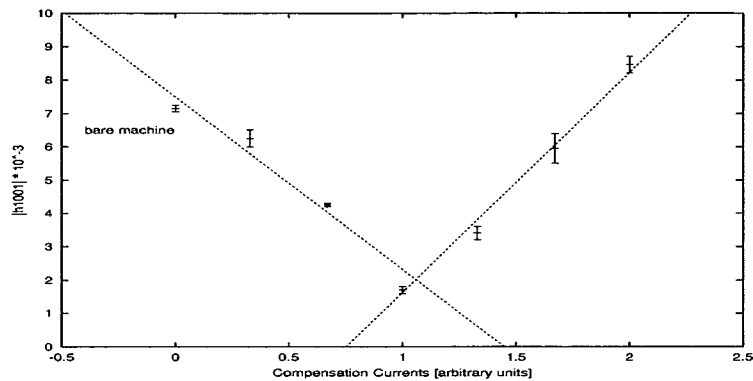


Figure 5.11: Stepwise compensation of the linear coupling difference resonance.

the x axis belongs to the bare machine condition. The drop in resonance strength is evident until the correct compensation values are reached. After passing these values the strength increases, representing “over compensation” of the resonance. The obtained results for the different adjustments are listed in Table 5.8. Reasonable strength and phase values were obtained from the

$I_{QSK210L3}$	$I_{QSK614L3}$	$ h_{1001} $	ψ_{1001}
0.0	0.0	$7.1 \pm 0.1 \cdot 10^{-3}$	$282.8^\circ \pm 5.2^\circ$
1.2	0.4	$6.3 \pm 0.3 \cdot 10^{-3}$	$266.2^\circ \pm 8.9^\circ$
2.4	0.8	$4.3 \pm 0.1 \cdot 10^{-3}$	$283.2^\circ \pm 24.4^\circ$
3.6	1.2	$1.7 \pm 0.1 \cdot 10^{-3}$	$158.6^\circ \pm 25.8^\circ$
4.8	1.6	$3.4 \pm 0.2 \cdot 10^{-3}$	$128.3^\circ \pm 12.2^\circ$
6.0	2.0	$6.0 \pm 0.5 \cdot 10^{-3}$	$110.1^\circ \pm 2.4^\circ$
7.2	2.4	$8.5 \pm 0.3 \cdot 10^{-3}$	$98.0^\circ \pm 4.7^\circ$

Table 5.8: Resonance strength and phase for different compensation current settings.

measurements. The resonance phase is expected to remain constant until the correct compensation currents are reached and to turn by 180° afterwards. Similar phases were measured for the first three current settings. Then for the compensation currents the phase is located in between the 180° phase jump with a high inaccuracy. Afterwards the compensation vector turns around and for $I_{QSK210L3} = 7.2$ A and $I_{QSK614L3} = 2.4$ A, twice the compensation currents, the phase has indeed changed by 180° .

5.2.4 Measurements with different chromaticities

To study the influence of decoherence due to chromaticity on the Fourier spectra, the measurements for the bare machine were done with different currents for the chromaticity sextupole family (XNOH0). The amplitude of the spectral lines are directly related to the decoherence processes (Section 3.5). For example, if the horizontal chromaticity Q'_x is zero, the horizontal tune line as well as the $(1, 0)$ resonance line in the vertical spectrum are not affected. In contrast, the vertical tune line and $(0, 1)$ resonance line in the horizontal plane are strongly reduced due to the increased vertical chromaticity. The following figures show the horizontal and vertical Fourier spectra for four different chromaticity adjustments. All figures are normalised to the largest spectral line (horizontal tune line in Fig. 5.12) to study the behaviour of the spectral lines for different chromaticities. Fig. 5.12 shows the situation when the chromaticity is corrected in the horizontal plane. The horizontal tune line is large, the vertical one is strongly affected by chromaticity. As expected, the resonance line is clearly visible in the vertical spectrum, but not in the horizontal one. If chromaticity is not corrected, Fig. 5.13, the horizontal tune amplitude is still larger than the vertical one. (The natural vertical chromaticity, $Q'_y \approx -9.3$, is bigger than the horizontal one, $Q'_x \approx -3.5$.) Resonance lines are visible in both spectra. For equal chromaticities, Fig. 5.14, tune and resonance lines have the same size. Fig. 5.15 presents the case for zero vertical chromaticity. The vertical tune line is bigger than the horizontal one. Resonance lines show up in both spectra.

(To demonstrate the influence of chromaticity on the transverse motion of the centroid of the beam, long observation periods (1000 turns) are required. As mentioned, the tunes undergo fluctuations over such long periods and so the peaks become broader even without chromaticity effects. Thus, specially in the last case, the influence of chromaticity on spectral lines is not that evident.)

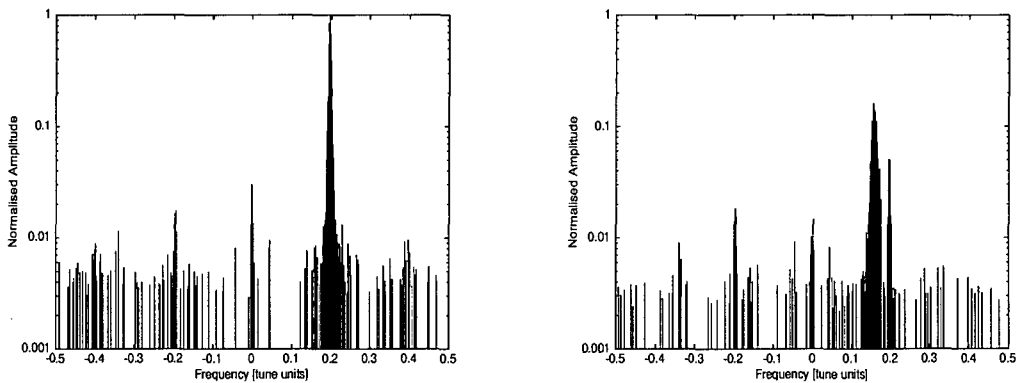


Figure 5.12: Horizontal (left) and vertical (right) Fourier spectrum for $Q'_x \approx 0$.

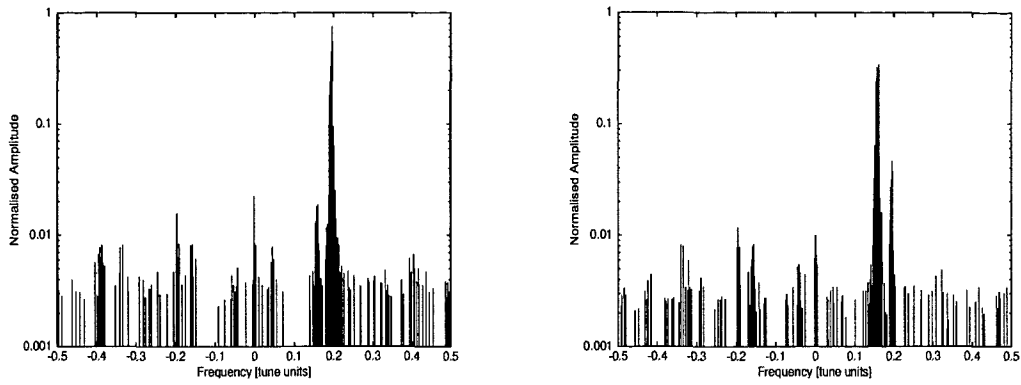


Figure 5.13: Horizontal (left) and vertical (right) Fourier spectrum for nat. chromaticities.

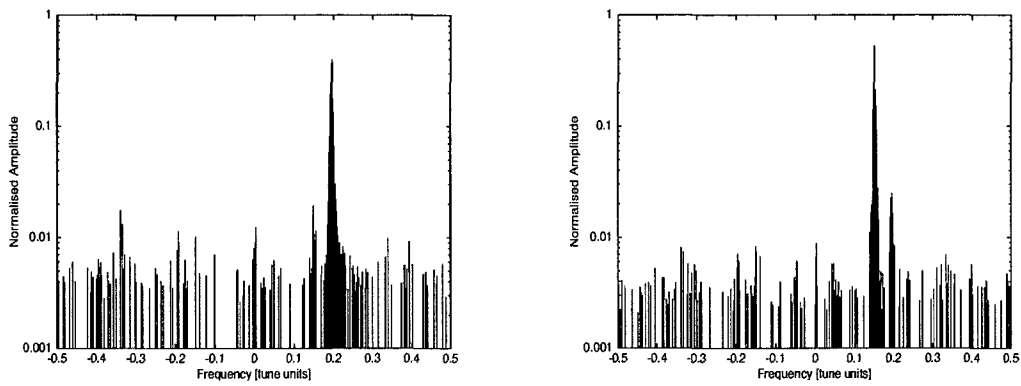


Figure 5.14: Horizontal (left) and vertical (right) Fourier spectrum for equal chromaticities.

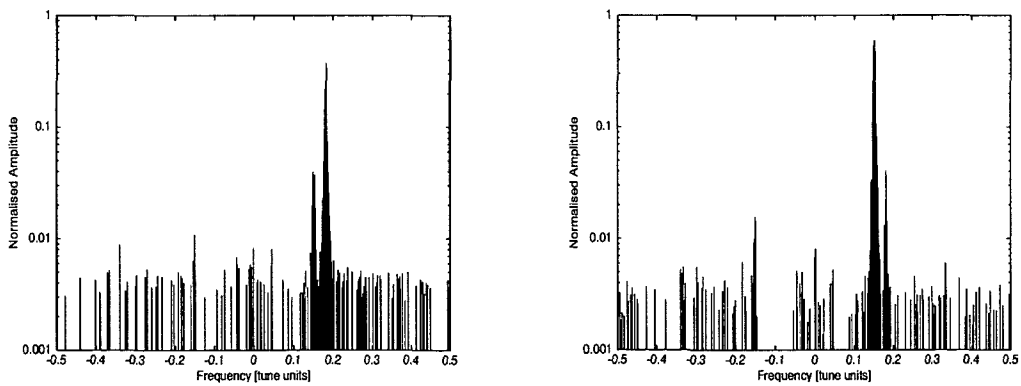


Figure 5.15: Horizontal (left) and vertical (right) Fourier spectrum for $Q_y^l \approx 0$.

5.3 The normal quadrupole resonance $2Q_y = 11$

The vertical second order resonance $2Q_y = 11$, driven by the Hamiltonian term h_{0020} , is covered by particles at injection and has to be compensated in standard operation. The corresponding resonance line is specified in Tab. 5.2. According to Tab. 3.2 the strength $|h_{0020}|$ and phase ψ_{0020} of the resonance driving term are related to the vertical $(0, -1)$ spectral line as presented in Tab. 5.9.

Driving Term		Vertical Spectral Line
Frequency		$(0, -1)$
Amplitude	$ h_{0020} $	$\sqrt{2I_y} \frac{2 \cdot h_{0020} }{\sin(\hat{\phi})} = a_{y1}$
Phase	ψ_{0020}	$\psi_{0020} - \psi_{y0} - \frac{\pi}{2} + \text{sgn}(\hat{\phi}) \left(\frac{\pi}{2} - \hat{\phi} \right) = \phi_{y1}$
where $\hat{\phi} = 2\pi\nu_y$		

Table 5.9: Relation between the $(0, -1)$ spectral line and the amplitude and phase of the h_{0020} Hamiltonian term.

From Tab. 5.9 strength and phase are given by,

$$|h_{0020}| = \frac{1}{2} \frac{a_{y1}}{a_{y0}} \sin(|\hat{\phi}|), \quad (5.17)$$

$$\psi_{0020} = \phi_{y1} + \psi_{y0} + \frac{\pi}{2} - \text{sgn}(\hat{\phi}) \left(\frac{\pi}{2} - |\hat{\phi}| \right), \quad (5.18)$$

where $a_{y0} = \sqrt{2I_y}$ is the vertical tune amplitude.

To determine this driving term, the vertical tune was placed close to resonance condition, $Q_y \approx 5.48$. For the measurements only the vertical particle motion is of interest, therefore the vertical chromaticity has to be corrected. In this case one important aspect has to be kept in mind. A beam off-set in one of the transverse planes at the location of a chromaticity correction sextupole gives rise to additional normal quadrupole contributions. Therefore it was decided to measure without chromaticity correction. Due to the large natural vertical chromaticity, the beam position signal decohered rapidly.

Another important point is the fact that β functions change in the presence of quadrupolar perturbations, leading to a different phase advance between the two acquisition PUs (known as “beta beating” [4]). For the analysis, the phase advance corresponding to the linear lattice without perturbations has to be used.

5.3.1 Measurement of the bare machine excitation

Fig. 5.16 shows the beam intensity over the first 500 turns after injection into the machine. The vertical tune couples to the resonance at about 300 turns, as visible from the beam position signal in Fig. 5.17. Immense losses occur in close vicinity to the resonance and after a few 100 turns almost no particles are left in the accelerator. The normalised phase space has the characteristic elliptical shape due to the quadrupole perturbations of the bare machine.

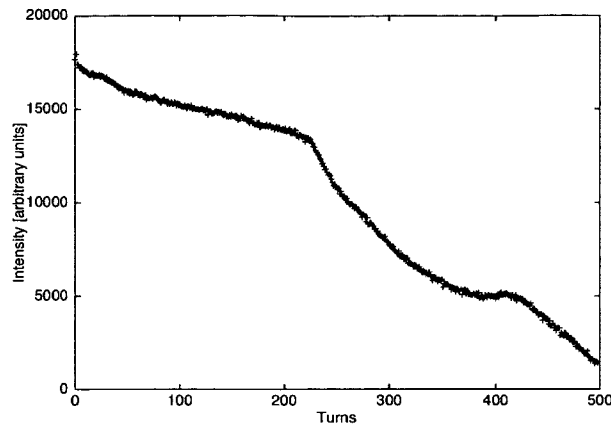


Figure 5.16: *Progression of beam intensity.*

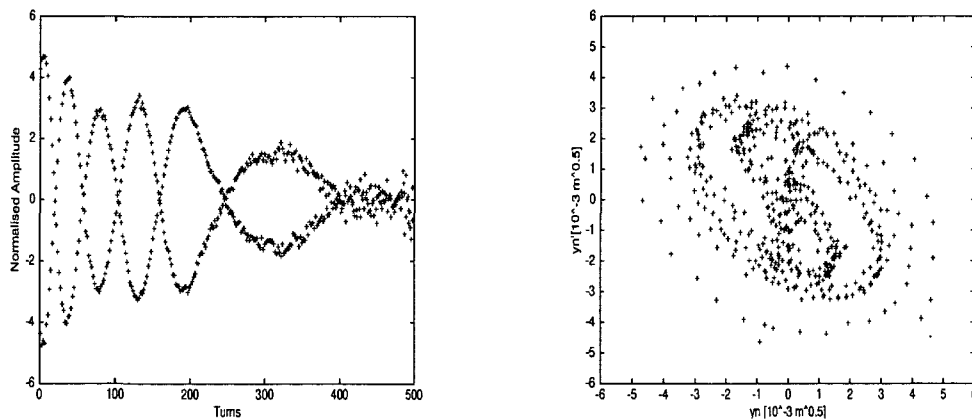


Figure 5.17: *Normalised vertical beam position and phase space for the first 500 turns after injection.*

The sequence of Figs. 5.18 to 5.23 shows the normalised vertical phase space for different vertical tunes. The tune range reaches from $Q_y=5.495$, close to the resonance condition, to $Q_y=5.454$, where almost no phase space perturbations are apparent any more (circular shape).

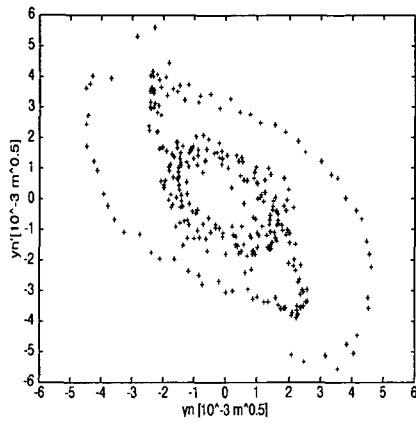


Figure 5.18: Norm. phase space, $Q_y=5.495$

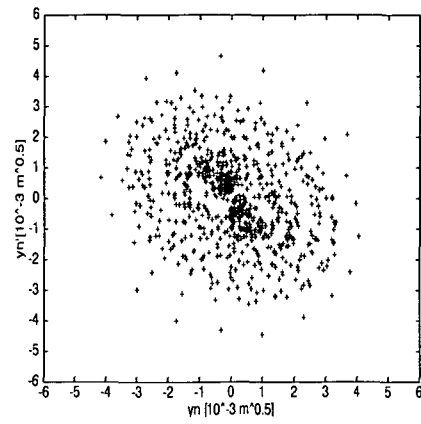


Figure 5.19: Norm. phase space, $Q_y=5.481$

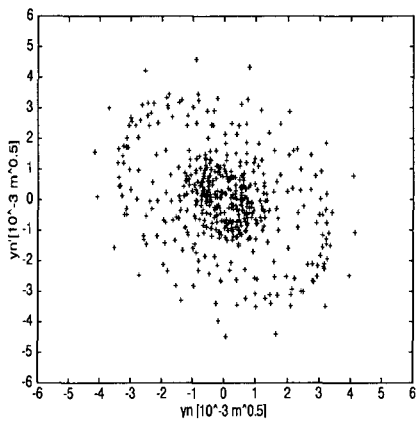


Figure 5.20: Norm. phase space, $Q_y=5.477$

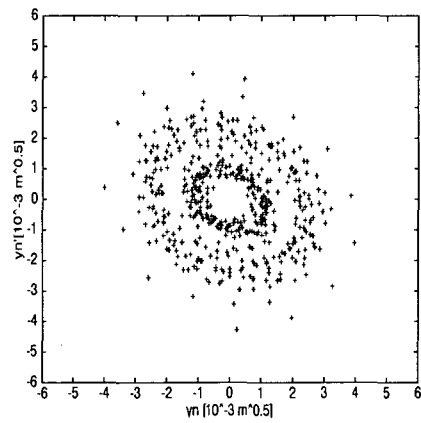


Figure 5.21: Norm. phase space, $Q_y=5.470$

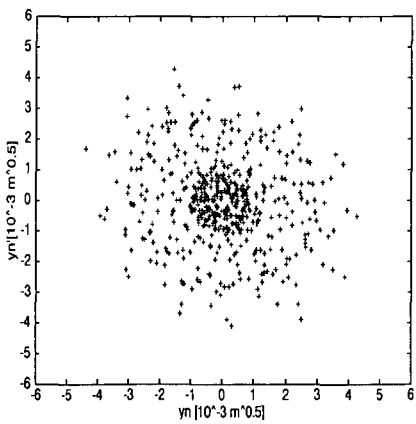


Figure 5.22: Norm. phase space, $Q_y=5.466$

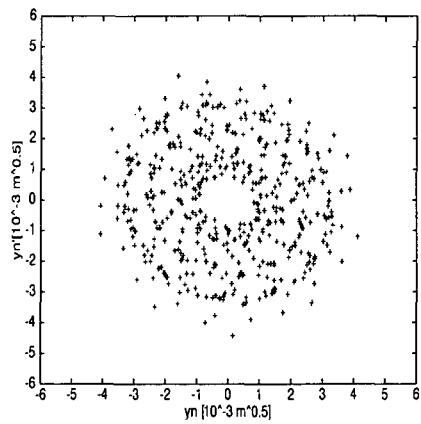


Figure 5.23: Norm. phase space, $Q_y=5.454$

Resonance strength and phase were calculated with Eqs. 5.17 and 5.18 and yield for the bare machine excitation,

- $|h_{0020}| = 7.0 \pm 0.4 \cdot 10^{-3}$, $\psi_{0020} = 269.8^\circ \pm 8.2^\circ$.

Fig. 5.24 shows the strong excitation of the resonance ((0,-1) spectral line).

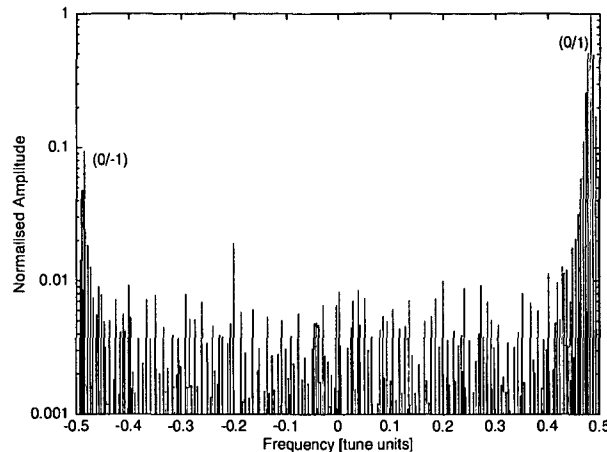


Figure 5.24: Vertical Fourier spectrum for the bare machine excitation, (0,-1) indicates the resonance line.

5.3.2 Reference measurements

The resonance was excited with both QNO quadrupole families to obtain a reference value for the strength and also to check the polarity of these elements for the compensation. After subtraction of the bare machine excitation, the following results were obtained and compared to simulations:

1. $I_{QNO412L3} = +15$ A:

- Measurements: $|h_{0020}| = 1.39 \pm 0.06 \cdot 10^{-2}$, $\psi_{0020} = 73.4 \pm 7.4^\circ$
- Simulation: $|h_{0020}| = 2.35 \cdot 10^{-2}$, $\psi_{0020} = 246.3^\circ$

2. $I_{QNO816L3} = -15$ A:

- Measurements: $|h_{0020}| = 1.68 \pm 0.1 \cdot 10^{-2}$, $\psi_{0020} = 141.1 \pm 4.3^\circ$
- Simulation: $|h_{0020}| = 2.35 \cdot 10^{-2}$, $\psi_{0020} = 153.3^\circ$

The measured phase of the first quadrupole family is opposite to expectations. For both families, the measured and simulated phases agree within 12° .

5.3.3 Compensation of the resonance

With the knowledge of the resonance strength and phase of the bare machine excitation and the resonance phases of the compensation elements from simulations, Eq. 4.3 yields for the h_{0020} driving term,

$$\begin{pmatrix} I_1 \\ I_2 \end{pmatrix} = M^{-1} \cdot \begin{pmatrix} |h_{0020}| \cdot \cos \psi_{0020} \\ |h_{0020}| \cdot \sin \psi_{0020} \end{pmatrix}, \quad (5.19)$$

where,

$$M = -\frac{q}{8p_0} \begin{pmatrix} \tilde{g}_{2(1)} \cdot l_{(1)} \cdot \beta_{y1} \cdot \cos \psi_{(1)} & \tilde{g}_{2(2)} \cdot l_{(2)} \cdot \beta_{y2} \cdot \cos \psi_{(2)} \\ \tilde{g}_{2(1)} \cdot l_{(1)} \cdot \beta_{y1} \cdot \sin \psi_{(1)} & \tilde{g}_{2(2)} \cdot l_{(2)} \cdot \beta_{y2} \cdot \sin \psi_{(2)} \end{pmatrix}. \quad (5.20)$$

The quantity \tilde{g}_2 represents the quadrupole gradient per ampère. The angles ψ are the resonance phases of the correction elements with respect to the PU in period 5.

Above equations yield,

- $I_{QNO412L3} = +6.27 \pm 0.55$ A (including the opposite polarity in the machine)
- $I_{QNO816L3} = -2.82 \pm 0.93$ A

Measurements were repeated with these currents. Fig. 5.25 shows the normalised phase space and the corresponding Fourier spectrum in case of compensation. The normalised phase space is quasi free from perturbations and the resonance line disappeared in the background noise.

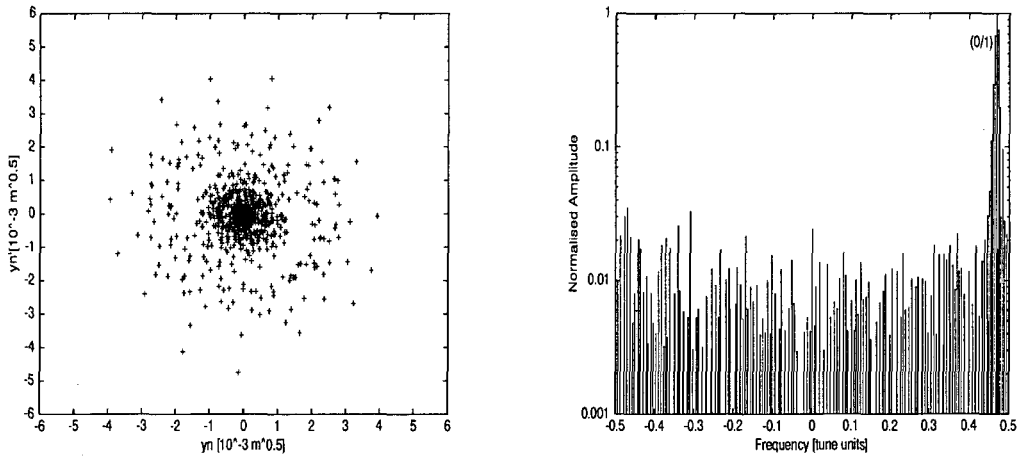


Figure 5.25: Normalised phase space and corresponding Fourier spectrum in case of compensation.

Figs. 5.26 and 5.27 show the beam intensity when the resonance is crossed in case of the bare machine and with compensation. The vertical tune was raised from 5.46 to 5.54 within 100 ms and then reduced within the same time back to 5.46, so the resonance was crossed twice. Without compensation total beam loss occur, whereas the situation significantly improved with compensation. Particle losses were reduced down to 15%. These losses can be explained by the fact that the resonance is crossed twice very slowly. In normal operation, no losses occur when the resonance is compensated.

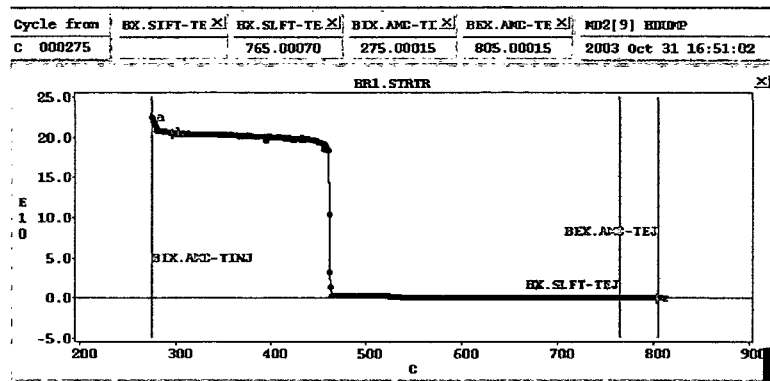


Figure 5.26: Beam intensity for the bare machine when the $2Q_y = 11$ resonance is crossed.

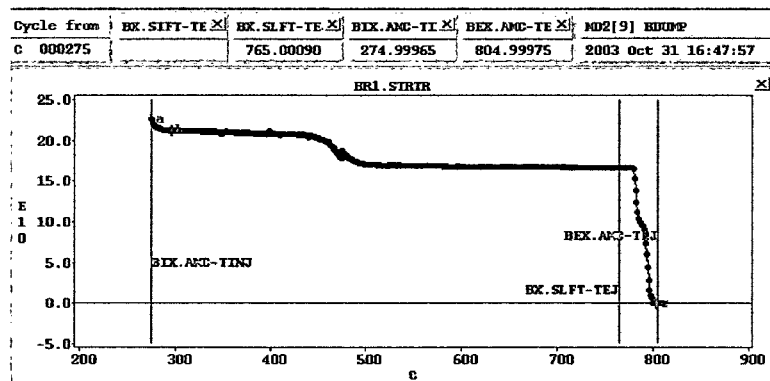


Figure 5.27: Beam intensity with the use of the compensation currents.

Table 5.10 compares the calculated compensation currents with those used in standard operation⁴. The agreement of the currents underlines the quality of the existing compensation scheme as well as the efficiency of the new method.

	Calculated currents	Currents used in operation
$I_{QNO412L3}$	+6.27 A	+7.1 A
$I_{QNO816L3}$	-2.82 A	-3.7 A

Table 5.10: Comparison of the calculated compensation currents and those used in standard operation.

⁴Current values for SFTPRO beam from August 2003.

Chapter 6

Measurement and compensation of third order resonance driving terms

6.1 Third order contributions to the Fourier spectra

The perturbative Hamiltonian term H_1 describing third order contributions (due to normal and skew sextupoles) is given by (Eq. 3.15),

$$H_1 = -\frac{q}{p_0} \text{Re} \left[\frac{1}{3} (B_3 + iA_3) \cdot (x + iy)^3 \right], \quad (6.1)$$

where B_3 and A_3 are the normal and skew coefficients respectively, as defined in Eqs. 3.9 and 3.10. H_1 can be re-written as:

$$H_1 = -\frac{q}{3p_0} [B_3(x^3 - 3xy^2) + A_3(y^3 - 3x^2y)]. \quad (6.2)$$

When considering third order resonances, the Hamiltonian coefficients h_{jklm} (Eq. 3.68) that fulfill $n = j + k + l + m = 3$ are of interest. From Tables 3.1 and 3.2 the associated spectral lines are found. Tables 6.1 and 6.2 show all concerned Hamiltonian terms and the appendant spectral lines due to normal sextupole contributions. From Tab. 6.1 one notes that the normal

Driving Term	Resonance	Lines Hor.	Lines Ver.
h_{3000}	(3,0)	(-2,0)	-
h_{2100}	(1,0)	(0,0)	-
h_{1200}	(1,0)	(2,0)	-
h_{0300}	(3,0)	-	-

Table 6.1: Driving terms, resonances and spectral lines due to the normal sextupole term x^3 .

sextupole term x^3 excites either horizontal third order or horizontal integer resonances. The term xy^2 excites third order coupling resonances and horizontal integer resonances.

The Hamiltonian terms related to skew sextupoles and the corresponding spectral lines are presented in Tables 6.3 and 6.4. Similar to the normal sextupole terms, the skew terms excite third and first order resonances.

Driving Term	Resonance	Lines Hor.	Lines Ver.
h_{1020}	(1,2)	(0,-2)	(-1,-1)
h_{1011}	(1,0)	(0,0)	(-1,1)
h_{1002}	(1,-2)	(0,2)	-
h_{0120}	(1,-2)	-	(1,-1)
h_{0111}	(1,0)	-	(1,1)
h_{0102}	(1,2)	-	-

Table 6.2: Driving terms, resonances and spectral lines due to the normal sextupole term xy^2 .

Driving Term	Resonance	Lines Hor.	Lines Ver.
h_{0030}	(0,3)	-	(0,-2)
h_{0021}	(0,1)	-	(0,0)
h_{0012}	(0,1)	-	(0,2)
h_{0003}	(0,3)	-	-

Table 6.3: Driving terms, resonances and spectral lines due to the skew sextupole term y^3 .

Driving Term	Resonance	Lines Hor.	Lines Ver.
h_{2010}	(2,1)	(-1,-1)	(-2,0)
h_{1110}	(0,1)	(1,-1)	(0,0)
h_{0210}	(2,-1)	-	(2,0)
h_{2001}	(2,-1)	(-1,1)	-
h_{1101}	(0,1)	(1,1)	-
h_{0201}	(2,1)	-	-

Table 6.4: Driving terms, resonances and spectral lines due to the skew sextupole term x^2y .

From the tune diagram of the PSB (Fig. 4.5) one notes that four third order resonances are covered by particles:

- $3Q_y = 16$, systematic skew sextupole resonance
- $2Q_x + Q_y = 14$, skew sextupole coupling resonance
- $2Q_x - Q_y = 3$, skew sextupole coupling resonance
- $Q_x + 2Q_y = 15$, normal sextupole coupling resonance

The most perturbing one is the systematic $3Q_y = 16$. It has to be compensated for a satisfactory performance of the PSB. For this two skew sextupoles are needed. However, switching on the compensation of $3Q_y = 16$ results in an excitation of the $2Q_x + Q_y = 14$ resonance and subsequent beam losses. Therefore a compensation scheme using four skew sextupoles is required.

The $2Q_x - Q_y = 3$ resonance does not cause beam losses and is not taken into account in the existing compensation scheme. The $Q_x + 2Q_y = 15$ resonance is compensated with two normal sextupoles. Detailed information on the compensation scheme used in standard operation is found in Ref. [13, 14].

6.2 The systematic resonance $3Q_y = 16$

Because of the importance of the systematic resonance $3Q_y = 16$, it was intensively studied [26]. For the determination of the corresponding resonance driving term h_{0030} , the vertical tune was adjusted close to resonance condition: $Q_y \approx 5.345$. The vertical chromaticity was corrected to zero (chromaticity sextupole family XNOH0 ≈ -52 A) because only the vertical particle motion was needed for the measurements.

According to Tab. 3.2 the strength $|h_{0030}|$ and phase ψ_{0030} of the resonance driving term are related to the vertical spectral line $(0, -2)$ as summarised in Tab. 6.5.

Driving Term		Vertical Spectral Line
Line		$(0, -2)$
Amplitude	$ h_{0030} $	$2I_y \frac{3 \cdot h_{0030} }{\sin(\hat{\phi})} = a_{y1}$
Phase	ψ_{0030}	$\psi_{0030} - 2\psi_{y0} - \frac{\pi}{2} + \text{sgn}(\hat{\phi})\left(\frac{\pi}{2} - \hat{\phi} \right) = \phi_{y1}$
where $\hat{\phi} = 2\pi\nu_y$		

Table 6.5: Relation between the spectral line $(0, -2)$ and the amplitude and phase of the h_{0030} Hamiltonian term.

Strength and phase are then expressed as:

$$|h_{0030}| = \frac{1}{3} \frac{a_{y1}}{a_{y0}^2} \sin(|\hat{\phi}|) \quad (6.3)$$

$$\psi_{0030} = \phi_{y1} + 2\psi_{y0} + \frac{\pi}{2} - \text{sgn}(\hat{\phi})\left(\frac{\pi}{2} - |\hat{\phi}|\right), \quad (6.4)$$

where $a_{y0} = \sqrt{2I_y}$ is the amplitude of the tune line.

6.2.1 Measurement of the bare machine excitation

Fig. 6.1 shows the normalised vertical beam position over the first 1000 turns after injection into the machine and the corresponding normalised phase space for a vertical tune close to the third integer resonance condition. In the beginning the tune is slightly below the resonance, then the resonance is crossed at approximately 250 turns and finally the tune is located in safe distance above the resonance (The change in tune is explained in Section 4.6.). The normalised phase

space shows the typical triangular distortion when sextupoles are present (see Section 3.2.3). The phase swaps by 180° at the moment of resonance crossing.

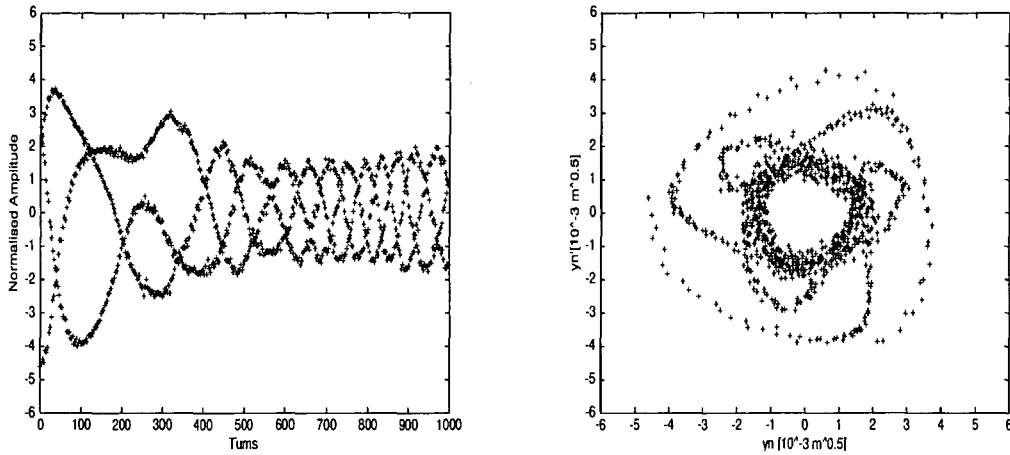


Figure 6.1: Normalised vertical beam position and corresponding phase space for the bare machine with Q_y close to the resonance condition.

Fig. 6.2 shows the beam intensity and the vertical Fourier spectrum. As visible, 60% of the particles are lost within the first 300 turns. The losses occur in close vicinity to the resonance. Once the tune is at a certain distance from the resonance, the remaining intensity stays constant. The Fourier spectrum shows the corresponding resonance line (0,-2).

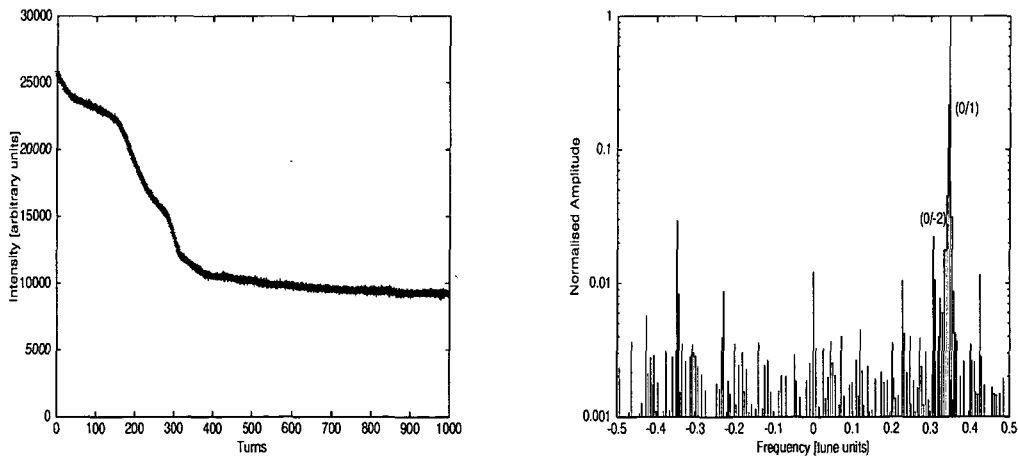


Figure 6.2: Beam intensity and vertical Fourier spectrum for the bare machine.

Eqs. 6.3 and 6.4 yield for the bare machine measurements:

$$|h_{0030}| = 9.0 \pm 0.6 \cdot 10^{-3} \text{mm}^{-\frac{1}{2}} \quad \text{and} \quad \psi_{0030} = -21.4^\circ \pm 13.9^\circ.$$

Different vertical injection mis-steering

From Table 6.5 one notes that the normalised amplitude of the resonance spectral line (a_{y1}/a_{y0}) is proportional to the amplitude of the transverse particle motion:

$$\frac{a_{y1}}{a_{y0}} = \sqrt{2I_y} \frac{3 \cdot |h_{0030}|}{\sin(|\hat{\phi}|)}. \quad (6.5)$$

This offers the opportunity to determine the resonance strength from a set of measurements with different particle oscillation amplitudes. If the normalised amplitude (multiplied by $\sin(\hat{\theta})$ to consider the slightly changing distance from the tune to the resonance condition) is plotted against the normalised oscillation amplitude and a line is fitted constrained to go through the origin, the resonance strength is obtained from the slope of the fitted line.

For this, the vertical injection mis-steering was changed from 0 mrad to -4 mrad in steps of -1 mrad to obtain different particle oscillation amplitudes. Figs. 6.3 to 6.7 show the normalised vertical oscillations over 1000 turns and the corresponding Fourier spectra for different injection mis-steering adjustments. For the first two settings, no resonance spectral lines are visible. The (0,-2) line starts appearing from -2 mrad injection mis-steering onwards. Then, as expected, the resonance line grows with the oscillation amplitude.

In Fig. 6.8 the normalised amplitude is plotted against the particle oscillation amplitude. From the slope of the fitted line, the resonance strength is obtained to:

- $|h_{0030}| = 8.6 \cdot 10^{-3} \text{ mm}^{-\frac{1}{2}}$.

One notes that even for a small number of measurements with different oscillation amplitudes, a similar result, in terms of resonance strength, for the bare machine was found.

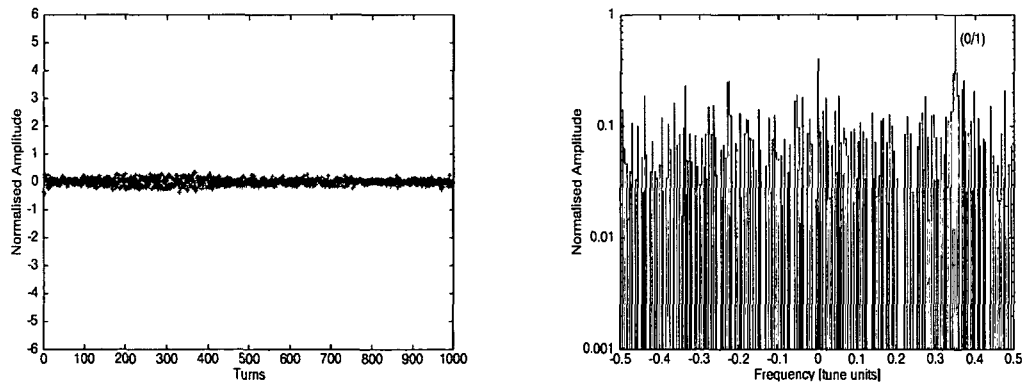


Figure 6.3: Normalised vertical beam position and corresponding Fourier spectrum without vertical injection mis-steering.

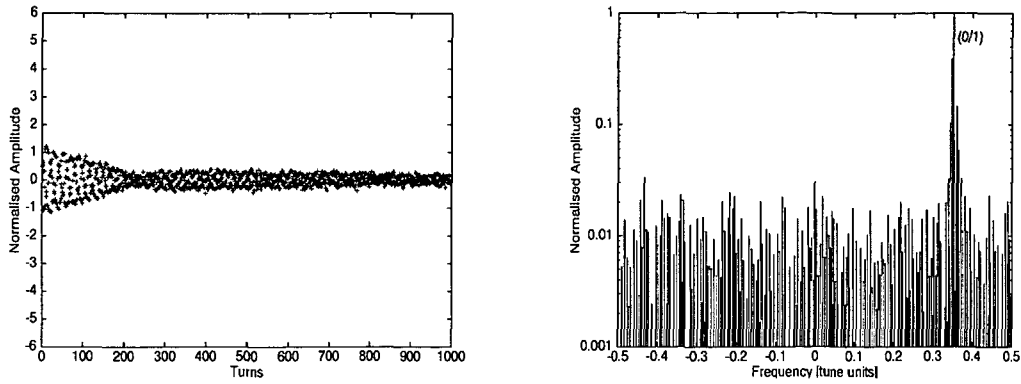


Figure 6.4: Normalised vertical beam position and corresponding Fourier spectrum for a vertical injection mis-steering of -1 mrad.

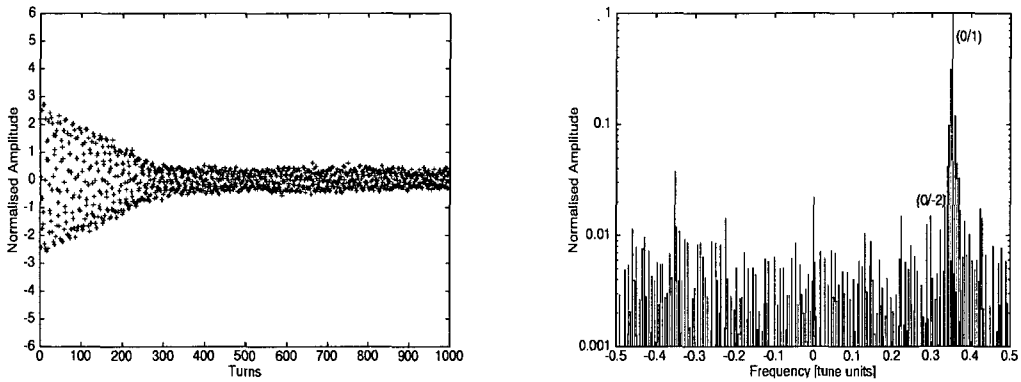


Figure 6.5: Normalised vertical beam position and corresponding Fourier spectrum for a vertical injection mis-steering of -2 mrad.

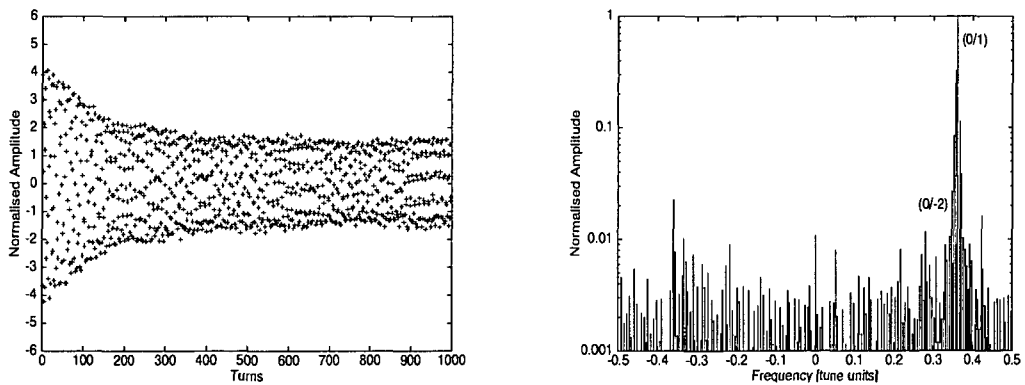


Figure 6.6: Normalised vertical beam position and corresponding Fourier spectrum for a vertical injection mis-steering of -3 mrad.

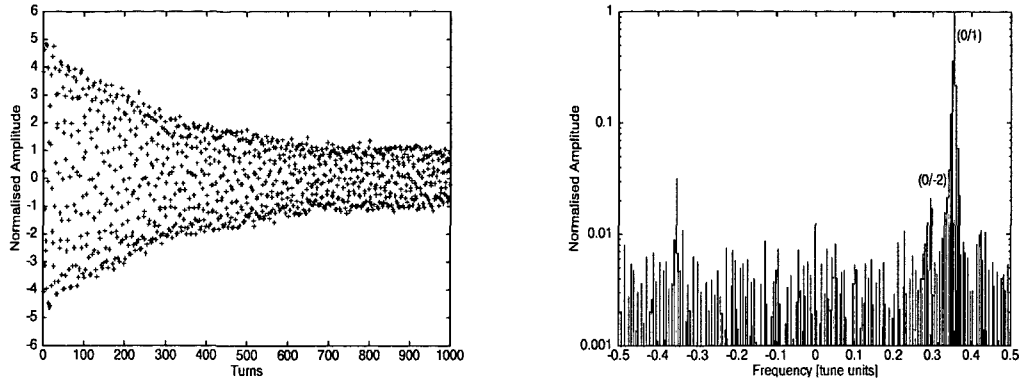


Figure 6.7: Normalised vertical beam position and corresponding Fourier spectrum for a vertical injection mis-steering of -4 mrad.

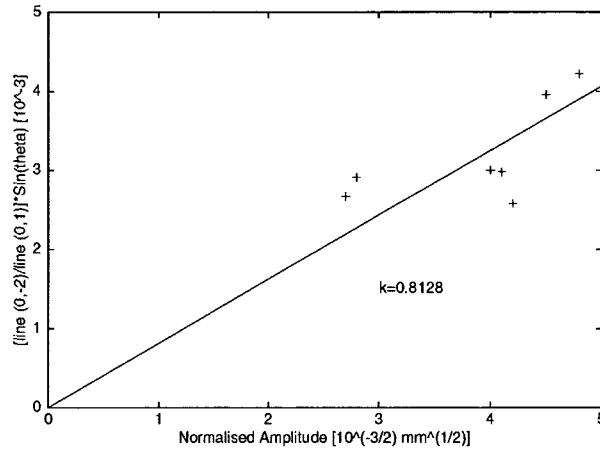


Figure 6.8: Normalised amplitude of the spectral line $(0,-2)$ versus the normalised vertical kick amplitude.

6.2.2 Reference measurements

The skew sextupole XSK2L4 is located in a high β_y region and therefore strongly excites the resonance. Tunes and chromaticity were adjusted as for the bare machine measurements. After subtraction of the bare machine component, Eqs. 6.3 and 6.4 yield for the defined excitation ($I_{XSK2L4} = -45$ A):

$$|h_{0030}| = 15.2 \pm 1.0 \cdot 10^{-3} \text{mm}^{-\frac{1}{2}} \quad \text{and} \quad \psi_{0030} = 157.2^\circ \pm 6.7^\circ.$$

Simulations with the single particle tracking code SixTrack [19] and SUSSIX [9] were performed to determine the resonance phase and strength of this skew sextupole w. r. t. the PU in period 5. Simulation gives:

$$|h_{0030}| = 14.3 \cdot 10^{-3} \text{mm}^{-\frac{1}{2}} \quad \text{and} \quad \psi_{0030} = 347.2^\circ.$$

Table 6.6 summarises the obtained results for the systematic resonance $3Q_y = 16$.

	Bare machine	Reference measurements	Simulation
$ h_{0030} $ [$\text{mm}^{-1/2}$]	$9.0 \pm 0.6 \cdot 10^{-3}$	$15.2 \pm 1.0 \cdot 10^{-3}$	$14.3 \cdot 10^{-3}$
ψ_{0030}	$-21.4^\circ \pm 13.9^\circ$	$157.2^\circ \pm 6.7^\circ$	347.2°

Table 6.6: Overview on resonance strengths and phases obtained for the bare machine and in case of excitation.

The comparison of the results obtained for the bare machine and the reference measurements shows that the strength of the bare machine excitation is comparable to $I_{XSK2L4} = 26.6$ A. This result underlines that a compensation of this resonance is mandatory for a satisfactory performance of the PSB.

The resonance strengths for the reference measurements and the simulation are similar, whereas the measured resonance phase is opposite to expectations, indicating an inversed polarity of the skew sextupole magnet. Taking into account the inversed polarity, measured and simulated resonance phase fit within ten degrees. Fig. 6.9 compares the normalised vertical phase spaces obtained from measurement and simulation ($I_{XSK2L4} = -45$ A, $Q_y = 5.341$). The triangular shape is opposed due to the inversed polarity.

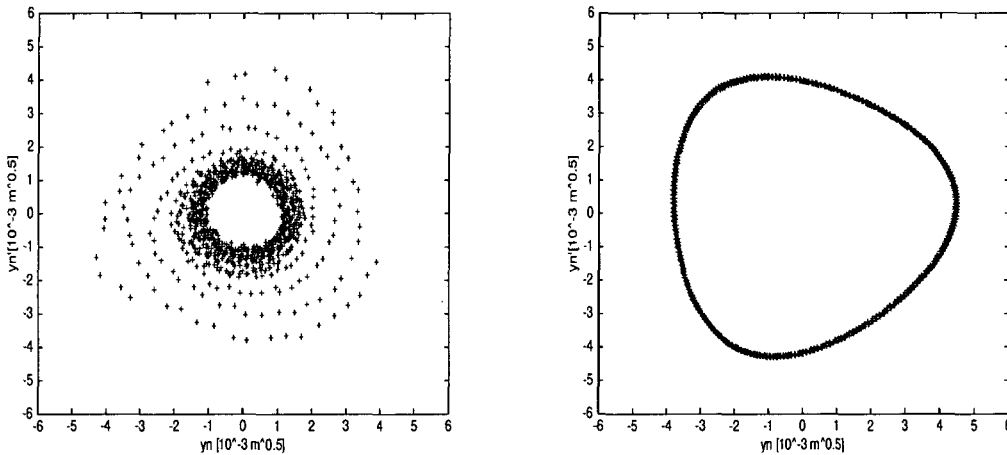


Figure 6.9: Normalised phase spaces obtained from measurement (left) and simulation (right).

6.2.3 Compensation of the resonance

With the knowledge of the bare machine excitation, the phases of the correction elements and the calibration factor, the compensation currents I_1 and I_2 of the two independent skew sextupoles are calculated with the modified Eq. 4.3,

$$\begin{pmatrix} I_1 \\ I_2 \end{pmatrix} = M^{-1} \cdot \begin{pmatrix} |h_{0030}| \cdot \cos \psi_{0030} \\ |h_{0030}| \cdot \sin \psi_{0030} \end{pmatrix}, \quad (6.6)$$

where,

$$M = -\frac{1}{48B\rho_0} \cdot \begin{pmatrix} \tilde{g}_{3(1)} \cdot l_{(1)} \cdot \beta_{z(1)}^{3/2} \cdot \cos \psi_{(1)} & \tilde{g}_{3(2)} \cdot l_{(2)} \cdot \beta_{z(2)}^{3/2} \cdot \cos \psi_{(2)} \\ \tilde{g}_{3(1)} \cdot l_{(1)} \cdot \beta_{z(1)}^{3/2} \cdot \sin \psi_{(1)} & \tilde{g}_{3(2)} \cdot l_{(2)} \cdot \beta_{z(2)}^{3/2} \cdot \sin \psi_{(2)} \end{pmatrix}. \quad (6.7)$$

The angles ψ are the resonance phases of the compensation elements w. r. t. the PU in period 5 obtained from simulations. The quantity \tilde{g}_3 represents the skew sextupole gradient per ampère, l is the length of the element and $B\rho_0$ is the magnetic rigidity.

The two skew sextupoles XSK2L4 and XSK9L1 were found suitable to compensate the $3Q_y = 16$ resonance. After two iterations the efficient compensation settings,

$$I_{XSK2L4} = -29.3A \quad \text{and} \quad I_{XSK9L1} = +15.3A$$

were calculated and subsequently successfully tested.

Fig. 6.10 shows the normalised vertical beam position over the first 1000 turns after injection into the machine and the corresponding normalised phase space when using the above mentioned compensation currents. After approximately 300 turns the vertical tune couples to the resonance. Contrary to the bare machine, the phase space appears “round” and is quasi free from perturbing higher order terms. The Fourier spectra and intensity curve (Fig. 6.11) also

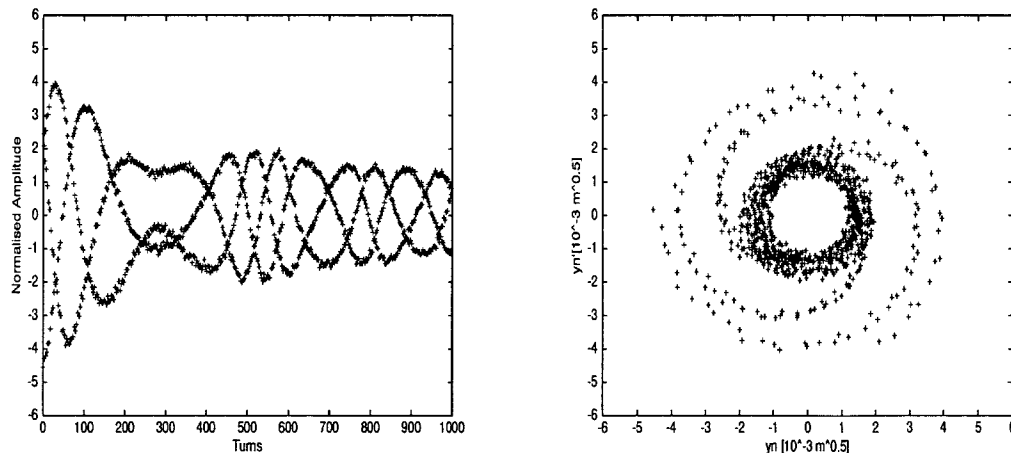


Figure 6.10: Normalised vertical beam position and corresponding phase space in case of compensation with Q_y close to the resonance condition.

demonstrate the effect of compensation. The (0,-2) spectral line disappeared and the former particle losses vanished.

Table 6.7 compares the skew sextupole currents used in standard operation¹ with those obtained from the measurements. Strength and phase of the h_{0030} driving term were calculated for both compensation settings. The results are quoted in Table 6.8.

¹SFTPRO, August 2003

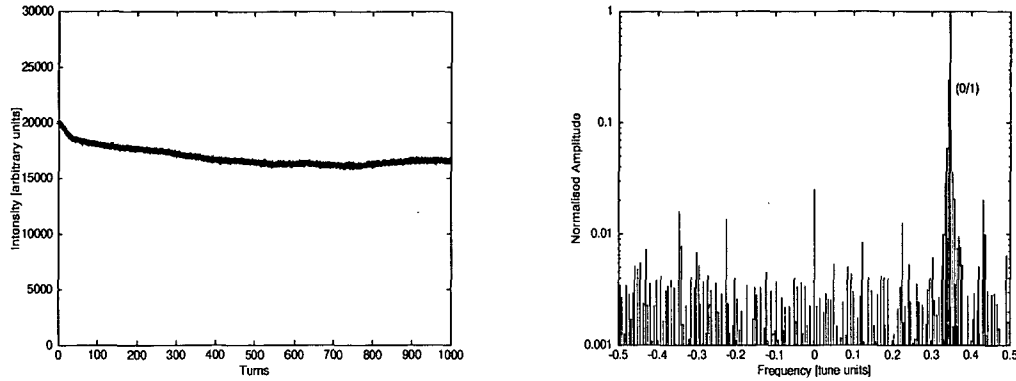


Figure 6.11: *Beam intensity and vertical Fourier spectrum in case of compensation.*

Compensation elements	Currents used in standard operation	Calculated currents
XSK2L4	-13.7 A	-29.3 A
XSK6L4	-17.6 A	—
XSK4L1	-19.0 A	—
XSK6L1	-14.9 A	—
XSK9L1	—	+15.3 A

Table 6.7: *Comparison of skew sextupole settings used in standard operation and the calculated currents.*

	Standard operation	Calculated currents
$ h_{0030} $ [$\text{mm}^{-1/2}$]	$9.4 \cdot 10^{-3}$	$9.7 \cdot 10^{-3}$
ψ_{0030}	169.6°	166.1°

Table 6.8: *Resonance strength and phase obtained for the currents presented in Table 6.7.*

The currents used in standard operation are different to those calculated from the measurements, but the resulting resonance strengths and phases are quasi identical, meaning that with both sets of currents, similar compensation vectors are obtained. It should be kept in mind, that the calculated currents excite the $2Q_x + Q_y = 14$ resonance. However, knowing the two-lens currents, the four-lens compensation settings to avoid an excitation of the coupling resonance are easily obtained [13, 14].

6.3 Third order coupling resonance driving terms

Table 6.9 gives an overview on the relevant third-order coupling resonances, the corresponding Hamiltonian terms and the spectral lines.

Resonance	Hamiltonian term	Horizontal line	Vertical line
$2Q_x + Q_y = 14$	h_{2010}	$(-1,-1)$	$(-2,0)$
$2Q_x - Q_y = 3$	h_{2001}	$(-1,1)$	$(2,0)$
$Q_x + 2Q_y = 15$	h_{1020}	$(0,-2)$	$(-1,-1)$

Table 6.9: Overview on third-order coupling resonances, the corresponding driving terms and spectral lines.

For the measurement of coupling resonances, the horizontal and vertical beam position signals are needed. Thus transverse signal decoherence in both planes should be avoided. As mentioned in Chapter 3.5, decoherence is caused by different particle tunes. The two main sources of tune spread are amplitude detuning and chromaticity. The detuning for particles with different amplitudes could not be analysed due to the lack of a proper kicker that is needed to vary the oscillation amplitudes. So the main objective was to reduce the chromaticities to reasonably low values in both planes. Eq. 3.88 shows how chromaticity affects the spectral lines. If the factor

$$\gamma_{(1-j+k),(m-l)} = [(1-j+k)Q'_x + (m-l)Q'_y]\sigma_s/Q_s$$

is zero, the corresponding spectral line is not interfered by chromaticity. This fact was used when determining the driving term of the difference resonance $2Q_x - Q_y = 3$. The corresponding horizontal spectral line $(-1,1)$ is not affected for equal chromaticities because $\gamma_{-1,1}$ becomes zero and the driving term can be measured. The vertical spectral line $(2,0)$ still suffers the influence of the horizontal chromaticity and appears reduced. For the sum resonances no proper chromaticity adjustment was found. The obtained results are presented in the following sections.

6.3.1 Difference coupling resonance $2Q_x - Q_y = 3$

For the analysis of the $2Q_x - Q_y = 3$ difference resonance, the tunes were set to $Q_x \approx 4.225$ and $Q_y \approx 5.415$. The chromaticities were adjusted to be equal in both planes. For this the chromaticity sextupoles were supplied with $I_{XNOH0} = -25$ A and $Q'_x \approx Q'_y \approx -5.3$ was obtained.

According to Tables 3.1 and 3.2, the strength and phase of the corresponding resonance driving term are related to the spectral lines as presented in Tables 6.10 and 6.11.

Driving Term		Horizontal Spectral Line
Line		$(-1, 1)$
Amplitude	$ h_{2001} $	$\sqrt{2I_x} \sqrt{2I_y} \frac{2 h_{2001} }{\sin(\hat{\phi})} = a_{x1}$
Phase	ψ_{2001}	$\psi_{2001} - \psi_{x_0} + \psi_{y_0} - \frac{\pi}{2} + \text{sgn}(\hat{\phi})\left(\frac{\pi}{2} - \hat{\phi} \right) = \phi_{x1}$
where $\hat{\phi} = \pi[2\nu_x - \nu_y]$		

Table 6.10: Relation between the $(-1,1)$ spectral line and the amplitude and phase of the h_{2001} Hamiltonian term.

Driving Term		Vertical Spectral Line
Line		$(2, 0)$
Amplitude	$ h_{0210} $	$2I_x \frac{ h_{0210} }{\sin(\hat{\phi})} = a_{y1}$
Phase	ψ_{0210}	$\psi_{0210} + 2\psi_{x_0} - \frac{\pi}{2} + \text{sgn}(\hat{\phi})\left(\frac{\pi}{2} - \hat{\phi} \right) = \phi_{y1}$
where $\hat{\phi} = \pi[-2\nu_y + \nu_x]$		

Table 6.11: Relation between the $(2,0)$ spectral line and the amplitude and phase of the h_{0210} Hamiltonian term.

From Tables 6.10 and 6.11 one obtains:

$$|h_{2001}| = \frac{1}{2} \frac{a_{x1}}{a_{x0}a_{y0}} \sin(|\hat{\phi}|), \quad (6.8)$$

$$|h_{0210}| = \frac{a_{y1}}{a_{x0}^2} \sin(|\hat{\phi}|), \quad (6.9)$$

$$\psi_{2001} = \phi_{x1} + \psi_{x_0} - \psi_{y_0} + \frac{\pi}{2} - \text{sgn}(\hat{\phi})\left(\frac{\pi}{2} - |\hat{\phi}|\right), \quad (6.10)$$

$$\psi_{0210} = \phi_{y1} - 2\psi_{x_0} + \frac{\pi}{2} - \text{sgn}(\hat{\phi})\left(\frac{\pi}{2} - |\hat{\phi}|\right), \quad (6.11)$$

where $a_{x0} = \sqrt{2I_x}$ and $a_{y0} = \sqrt{2I_y}$ are the amplitudes of the horizontal and the vertical tune line respectively. The driving term h_{0210} is the complex conjugate of h_{2001} and $\psi_{0210} = -\psi_{2001}$.

Measurement of the bare machine excitation

No particles are lost while crossing this resonance in bare machine condition (Fig. 5.2). This does however not imply that no resonance excitation is present. Particle motion and energy can be transferred from one transverse plane to the other without apparent losses.

Fig. 6.12 shows the normalised horizontal and vertical Fourier spectra obtained from bare machine measurements with tunes close to the resonance condition. In the horizontal spectrum

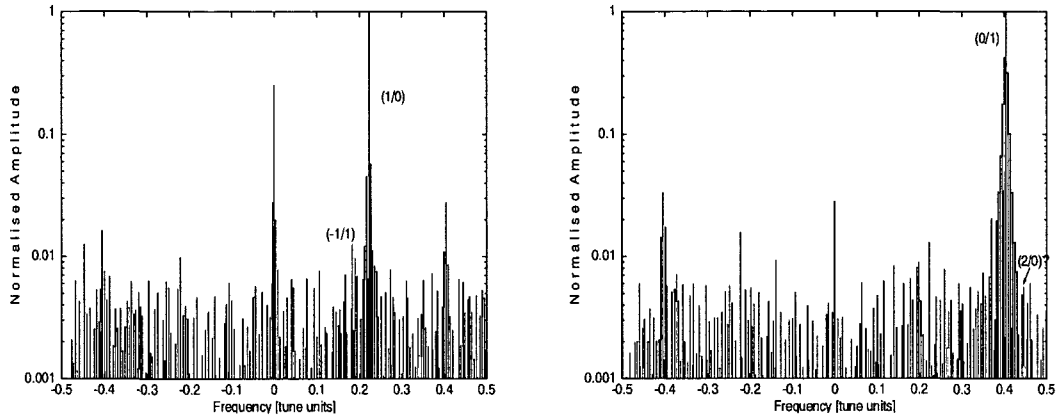


Figure 6.12: Horizontal and vertical Fourier spectrum for tunes close to the $2Q_x - Q_y = 3$ resonance condition.

the $(-1,1)$ resonance line is visible, whereas in the vertical spectrum the $(2,0)$ line is covered by the background. Therefore the horizontal resonance line was used to determine the driving term. Eqs. 6.8 and 6.10 yield for the strength and phase of the bare machine excitation:

- $|h_{2001}| = 6.8 \pm 1.5 \cdot 10^{-3} \text{ mm}^{-\frac{1}{2}}$
- $\psi_{2001} = -84.5^\circ \pm 7.0^\circ$

The excitation seems to be strong compared to the result for $|h_{0030}|$, the strength of the systematic resonance. This is because the resonance line is normalised to the tune lines which are influenced by chromaticity.

Reference measurement

The skew sextupole XSK2L4 was powered with $I_{XSK2L4} = -45 \text{ A}$ to excite the resonance. Tunes and chromaticities were adjusted as for the bare machine measurements. Fig. 6.13 shows the horizontal and vertical Fourier spectrum. Due to the strong excitation the corresponding resonance lines are visible in both spectra.

After subtraction of the bare machine contribution, Eqs. 6.8 and 6.10 give:

- $|h_{2001}| = 3.9 \pm 0.5 \cdot 10^{-2} \text{ mm}^{-\frac{1}{2}}$
- $\psi_{2001} = 181.9^\circ \pm 15.2^\circ$

The comparison of the results of the bare machine and skew sextupole excitation shows that the bare machine perturbation is equivalent to $I_{XSK2L4} = 7.8 \text{ A}$.

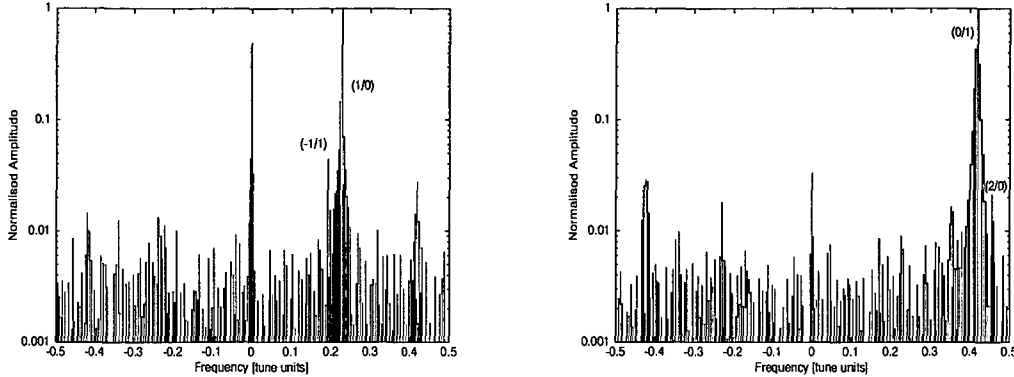


Figure 6.13: Horizontal and vertical Fourier spectrum in case of the reference measurements.

Simulations were performed to determine the resonance phase and strength of the XSK2L4 skew sextupole w. r. t. the location of the PU in period 5. Simulation yields:

$$|h_{2001}| = 1.9 \cdot 10^{-2} \text{mm}^{-\frac{1}{2}} \quad \text{and} \quad \psi_{2001} = 348.5^\circ.$$

One notes, that the amplitude of the measurement is twice the simulated one. This is explained by the fact that the measured tune lines are affected by chromaticity, the simulated not, leading to larger strength values obtained from the measurement. Furthermore the measured resonance phase is opposite to expectations, indicating an inversed polarity of the skew sextupole magnet. This fact was already discovered during the analysis of the systematic $3Q_y = 16$ resonance. Taking into account the inversed polarity, measured and simulated resonance phase agree within 15° .

Table 6.12 summarises the obtained results for the bare machine and reference measurements.

	Bare machine	Reference measurements	Simulation
$ h_{2001} $ [$\text{mm}^{-1/2}$]	$6.8 \pm 1.5 \cdot 10^{-3}$	$3.9 \pm 0.5 \cdot 10^{-2}$	$1.9 \cdot 10^{-2}$
ψ_{2001}	$-84.5^\circ \pm 7.0^\circ$	$181.9^\circ \pm 15.2^\circ$	348.5°

Table 6.12: Overview on resonance strengths and phases obtained for the bare machine and in case of excitation.

Compensation of the resonance

With the knowledge of the bare machine excitation, the phases of the correction elements and the calibration factor, the compensation currents of two independent skew sextupoles can be calculated with Eq. 4.3 to:

$$I_{XSK2L4} = -1.8 \pm 1.0\text{A} \quad \text{and} \quad I_{XSK4L1} = -18.9 \pm 4.3\text{A}.$$

These results were only obtained at the end of the run 2003. Since the PSB start-up in 2004 was done with a different working point (Chapter 7), these calculated compensation currents could not be verified experimentally.

6.3.2 Sum coupling resonance $2Q_x + Q_y = 14$

According to Tables 3.1 and 3.2 the strength $|h_{2010}|$ and phase ψ_{2010} of the resonance driving term are related to the corresponding spectral lines $(-1,-1)$ and $(-2,0)$ as presented in Tables 6.13 and 6.14.

Driving Term		Horizontal Spectral Line
Line		$(-1, -1)$
Amplitude	$ h_{2010} $	$\sqrt{2I_x}\sqrt{2I_y}\frac{2 h_{2010} }{\sin(\hat{\phi})} = a_{x1}$
Phase	ψ_{2010}	$\psi_{2010} - \psi_{x0} - \psi_{y0} - \frac{\pi}{2} + \text{sgn}(\hat{\phi})(\frac{\pi}{2} - \hat{\phi}) = \phi_{x1}$
where $\hat{\phi} = \pi[2\nu_x + \nu_y]$		

Table 6.13: Relation between the $(-1,-1)$ spectral line and the amplitude and phase of the h_{2010} Hamiltonian term.

Driving Term		Vertical Spectral Line
Line		$(-2, 0)$
Amplitude	$ h_{2010} $	$2I_x\frac{ h_{2010} }{\sin(\hat{\phi})} = a_{y1}$
Phase	ψ_{2010}	$\psi_{2010} - 2\psi_{x0} - \frac{\pi}{2} + \text{sgn}(\hat{\phi})(\frac{\pi}{2} - \hat{\phi}) = \phi_{y1}$
where $\hat{\phi} = \pi[2\nu_y + \nu_x]$		

Table 6.14: Relation between the $(-2,0)$ spectral line and the amplitude and phase of the h_{2010} Hamiltonian term.

Tables 6.13 and 6.14 yield for the strength and phase of the driving term:

$$|h_{2010}| = \frac{1}{2} \frac{a_{x1}}{a_{x0}a_{y0}} \sin(|\hat{\phi}|), \quad (6.12)$$

$$|h_{2010}| = \frac{a_{y1}}{a_{x0}^2} \sin(|\hat{\phi}|), \quad (6.13)$$

$$\psi_{2010} = \phi_{x1} + \psi_{x0} + \psi_{y0} + \frac{\pi}{2} - \text{sgn}(\hat{\phi})(\frac{\pi}{2} - |\hat{\phi}|), \quad (6.14)$$

$$\psi_{2010} = \phi_{y1} + 2\psi_{x0} + \frac{\pi}{2} - \text{sgn}(\hat{\phi})(\frac{\pi}{2} - |\hat{\phi}|), \quad (6.15)$$

where $a_{x0} = \sqrt{2I_x}$ and $a_{y0} = \sqrt{2I_y}$ are the amplitudes of the horizontal and the vertical tune line respectively.

For the analysis of this resonance, the tunes were set to $Q_x \approx 4.30$ and $Q_y \approx 5.45$. Compared to the difference resonance in the previous section, no proper chromaticity adjustment was found. An unaffected resonance line is only obtained when the horizontal chromaticity is zero. In this case the vertical line $(-2,0)$ is not disturbed. However, minimising the horizontal chromaticity has the detrimental effect of increasing the vertical one, leading to a fast signal decoherence in the vertical plane. This widens the tune peak and the mentioned resonance line is likely to be covered. Therefore the measurements were done with natural chromaticities.

Measurement of the bare machine excitation

Fig. 6.14 shows a continuous but rather small intensity drop throughout the cycle. The resonance is crossed within 100 ms starting 80 ms after injection. No additional losses occur during that period.

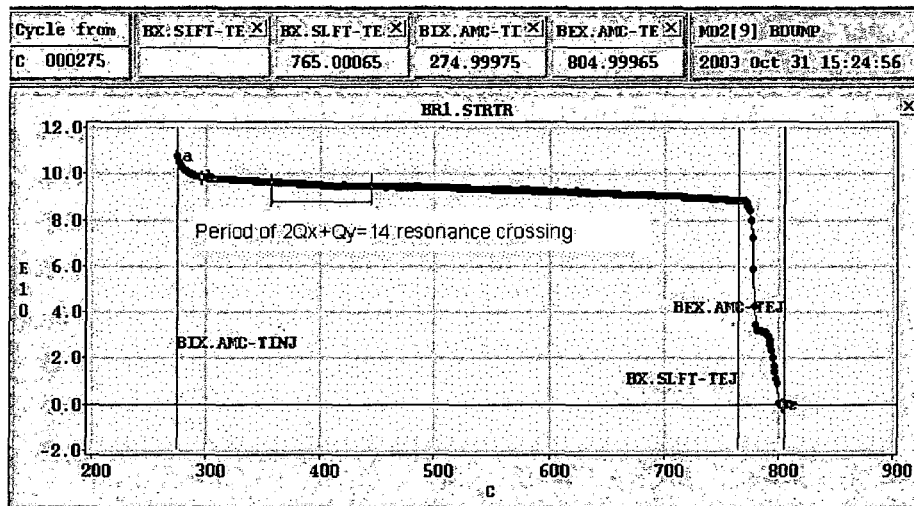


Figure 6.14: Beam intensity while crossing the $2Q_x + Q_y = 14$ resonance.

Measurements to determine the bare machine resonance driving term were carried out. The corresponding resonance lines could not be identified in the Fourier spectra. Either there is only a small bare machine excitation or the resonance lines are reduced due to the decoherence of the beam position signals and are covered by the background noise.

Reference measurements

Measurements with the skew sextupole XSK2L4 powered with -45 A were performed to investigate if resonance lines appear in case of strong excitation. Fig. 6.15 shows the horizontal and vertical beam position signals over 1000 turns. The normalised vertical oscillation amplitude is smaller than the horizontal one due to different injection mis-steering settings and different horizontal and vertical β functions. Additionally, the vertical signal decoheres faster because of a larger natural chromaticity in this plane. The tune spread due to chromaticity widens and lowers the tune peak, which is clearly visible in Fig. 6.16. Both spectra are normalised to the horizontal tune line to emphasise the effect of different oscillation amplitudes and signal decoherence on the spectra. Various spectral lines due to the skew sextupolar excitation are labelled in the spectra.

Table 6.15 gives an overview on the concerned skew sextupole resonances and the corresponding spectral lines.

Resonance	Horizontal line	Vertical line
$2Q_x + Q_y = 14$	(-1,-1)	(-2,0)
$2Q_x - Q_y = 3$	(-1,1)	(2,0)
$3Q_y = 16$	—	(0,-2)

Table 6.15: Overview on skew sextupole resonances and spectral lines.

The remarkable result is that all resonance spectral lines due to the skew sextupole excitation are visible in the measured Fourier spectra. Additional lines corresponding to integer resonance excitation are also indicated in the spectra and are summarised in Table 6.16. Only the (1,1) spectral line could not be identified.

Horizontal line	Vertical line
(1,-1)	(0,0)
(1,1)	(0,2)

Table 6.16: Spectral lines due to integer resonance excitation.

Further large spectral lines appear due to quadrupolar contributions. These lines are not marked and not discussed in this section.

To confirm the measurements, simulations with $I_{XSK2L4} = -45$ A were performed. The amplitudes were chosen equal to the starting amplitudes of the measurements (Fig. 6.17). Signal decoherence was not taken into account. All resonance lines in the Fourier spectra from the simulation are based on the powered skew sextupole. The spectra from the measurement and the simulation show the same resonance lines, with exception of the (1,1) integer line. Different amplitudes in the measured and simulated spectra are explained by the effect of chromaticity on the measured spectral lines.

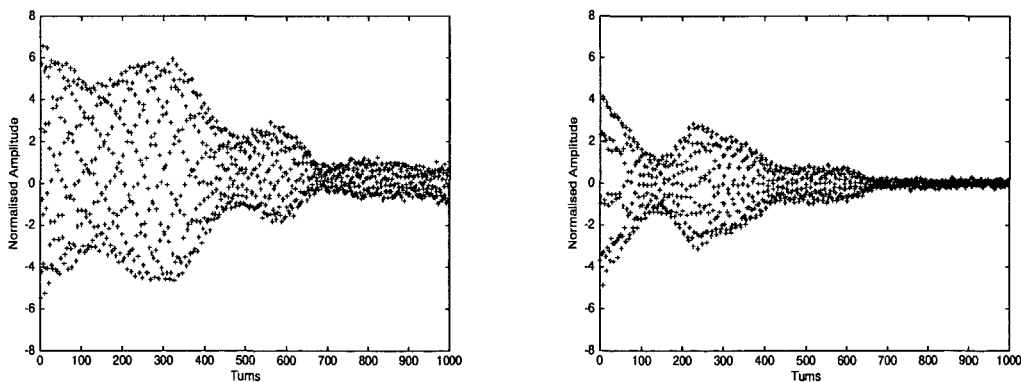


Figure 6.15: Normalised horizontal and vertical beam position (measurement).

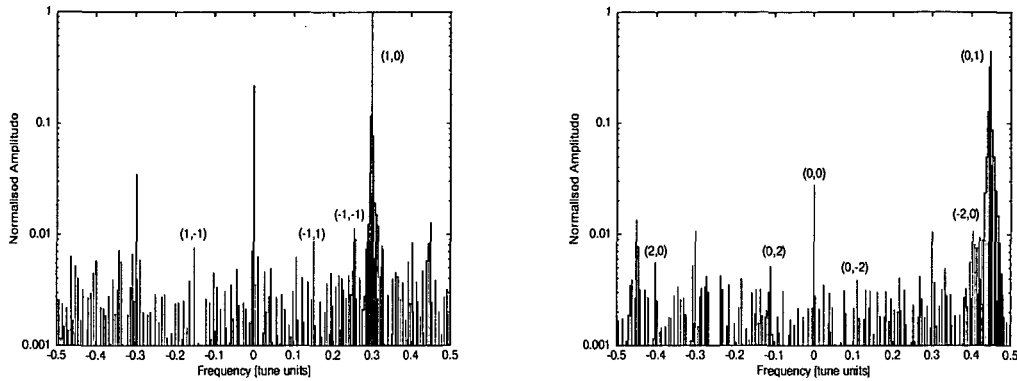


Figure 6.16: Horizontal and vertical Fourier spectra for tunes close to the $2Q_x + Q_y = 14$ resonance condition (measurement).

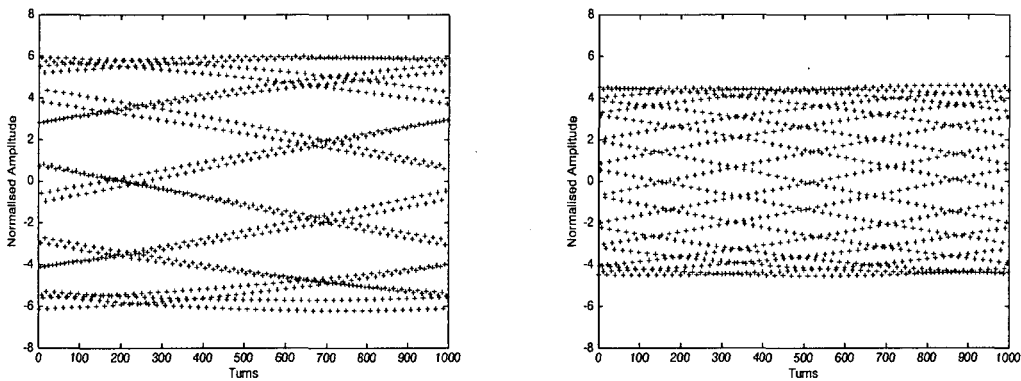


Figure 6.17: Normalised horizontal and vertical beam position (simulation).

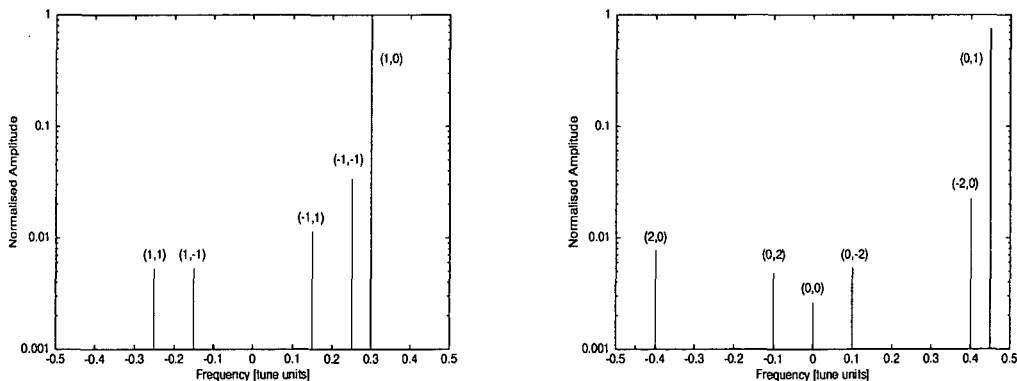


Figure 6.18: Horizontal and vertical Fourier spectra from for tunes close to the $2Q_x + Q_y = 14$ resonance condition (simulation).

6.3.3 Sum coupling resonance $Q_x + 2Q_y = 15$

According to Tables 3.1 and 3.2 the strength $|h_{1020}|$ and phase ψ_{1020} of the resonance driving term are related to the corresponding horizontal and vertical spectral line as presented in Tables 6.17 and 6.18.

Driving Term		Horizontal Spectral Line
Frequency		$(0, -2)$
Amplitude	$ h_{1020} $	$2I_y \frac{ h_{1020} }{\sin(\hat{\phi})} = a_{x1}$
Phase	ψ_{1020}	$\psi_{1020} - 2\psi_{y0} - \frac{\pi}{2} + \text{sgn}(\hat{\phi})(\frac{\pi}{2} - \hat{\phi}) = \phi_{x1}$
where $\hat{\phi} = \pi[\nu_x + 2\nu_y]$		

Table 6.17: Relation between the $(0,-2)$ spectral line and the amplitude and phase of the h_{1020} Hamiltonian term.

Driving Term		Vertical Spectral Line
Frequency		$(-1, -1)$
Amplitude	$ h_{1020} $	$\sqrt{2I_x} \sqrt{2I_y} \frac{2 h_{1020} }{\sin(\hat{\phi})} = a_{y1}$
Phase	ψ_{1020}	$\psi_{1020} - \psi_{x0} - \psi_{y0} - \frac{\pi}{2} + \text{sgn}(\hat{\phi})(\frac{\pi}{2} - \hat{\phi}) = \phi_{y1}$
where $\hat{\phi} = \pi[\nu_y + 2\nu_x]$		

Table 6.18: Relation between the $(-1,-1)$ spectral line and the amplitude and phase of the h_{1020} Hamiltonian term.

From Tables 6.17 and 6.18 one concludes:

$$|h_{1020}| = \frac{a_{x1}}{a_{y0}^2} \sin(|\hat{\phi}|), \quad (6.16)$$

$$|h_{1020}| = \frac{1}{2} \frac{a_{y1}}{a_{x0} a_{y0}} \sin(|\hat{\phi}|), \quad (6.17)$$

$$\psi_{1020} = \phi_{x1} + 2\psi_{y0} + \frac{\pi}{2} - \text{sgn}(\hat{\phi})(\frac{\pi}{2} - |\hat{\phi}|), \quad (6.18)$$

$$\psi_{1020} = \phi_{y1} + \psi_{x0} + \psi_{y0} + \frac{\pi}{2} - \text{sgn}(\hat{\phi})(\frac{\pi}{2} - |\hat{\phi}|), \quad (6.19)$$

where $a_{x0} = \sqrt{2I_x}$ and $a_{y0} = \sqrt{2I_y}$ are the amplitudes of the horizontal and the vertical tune line respectively.

For the analysis of this resonance, the tunes were set to $Q_x \approx 4.23$ and $Q_y \approx 5.40$. As for the skew sextupole sum resonance, chromaticities could not be adjusted properly. Furthermore the effect of the powered chromaticity sextupole family on this resonance would be difficult to estimate and the measurements were therefore done with natural chromaticities.

Measurement of the bare machine excitation

For standard machine operation this resonance has to be compensated. Fig. 6.19 shows the beam intensity when the resonance is slowly crossed within some 100 ms. More than two thirds of the beam is lost.

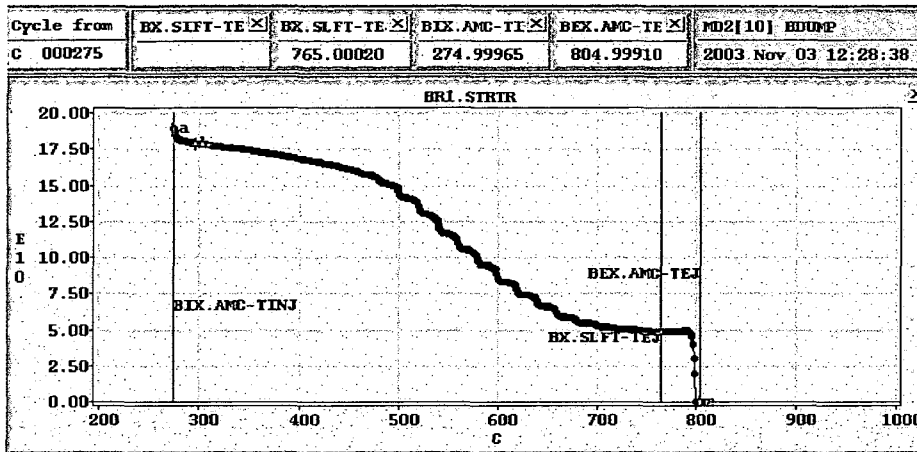


Figure 6.19: Beam intensity when the $Q_x + 2Q_y = 15$ resonance is crossed.

Fig. 6.20 shows the corresponding working line. The tune is moved from above to below the resonance.

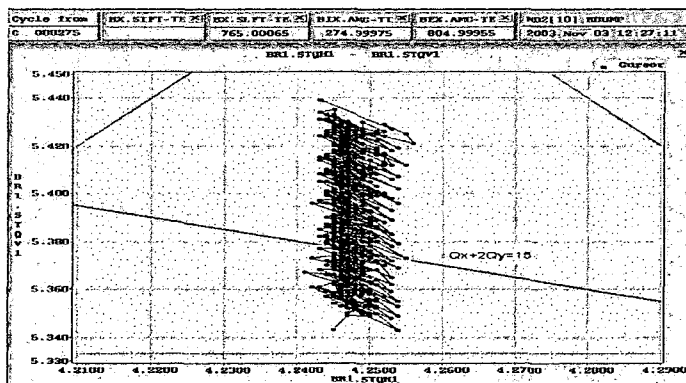


Figure 6.20: Tune line, the resonance is crossed from above to below.

Given the large beam loss one expects to find the appertaining resonance lines in the Fourier spectra. Measurements performed close to the resonance condition did not show these lines which can be explained with the decoherence of the beam position signals.

It is however interesting to present the corresponding normalised vertical phase space which shows a fivefold symmetry, indicating a decapole perturbation (Fig. 6.21). The vertical tune was measured to $Q_y \approx 5.40$ and therefore couples to the fifth order $5Q_y = 27$ resonance.

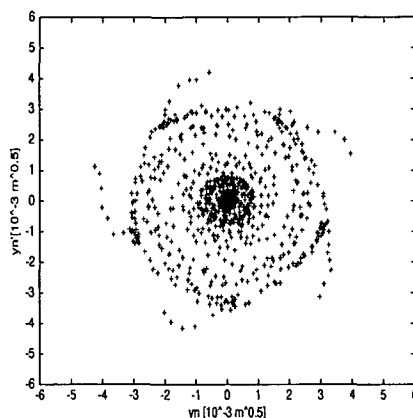


Figure 6.21: Fivefold symmetry of the normalised vertical phase space in vicinity to the fifth order $5Q_y = 27$ resonance.

Compensation of the resonance

Since the bare machine excitation could not be measured, no compensation currents were calculated. For standard operation, this resonance is compensated with two independent normal sextupoles. The currents are listed in Table 6.19².

Compensation element	Current
XNO4L1	2.9 A
XNO12L1	3.4 A

Table 6.19: Compensation currents used in standard operation.

²SFTPRO, August 2003

Chapter 7

Alternative working point for the PS Booster

At the end of the run 2003 a new, alternative working point for the PSB was tested to avoid the $3Q_y = 16$ systematic resonance and hereby potentially increase the beam intensity and brightness. This change of the working point was already proposed in 2001 [24]. The vertical tune was shifted one integer down to 4.23, thus only non-systematic resonances are present in the working area. Fig. 7.1 shows the tune diagram for the new working point.

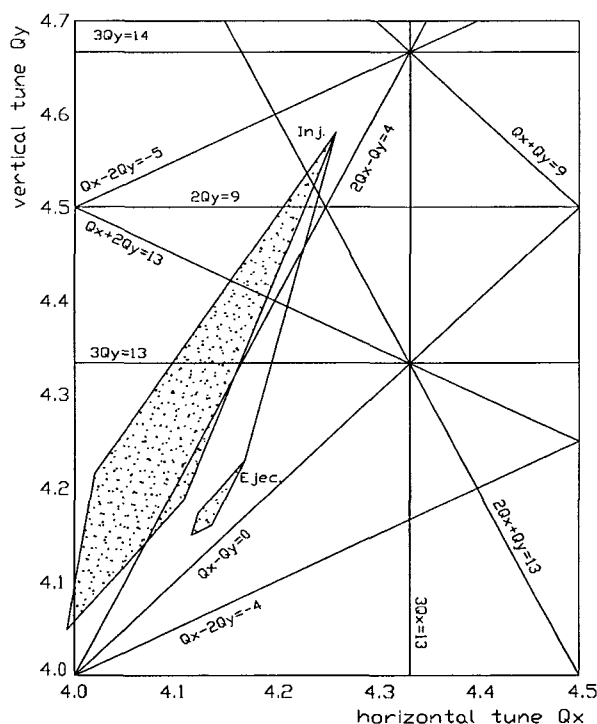


Figure 7.1: PSB tune diagram for the alternative working point for high intensity beams.

During a three-day measurement campaign, measurements of the bare machine resonance strengths ($|h_{0020}|$ and $|h_{0030}|$) for the most important resonances ($2Q_y = 9$ and $3Q_y = 13$) were made. Table 7.1 compares the measured resonance strength for the old and new working point for ring 1.

Driving Term	Old working point	New working point
h_{0020}	7.0 ± 0.4	3.2 ± 0.1
h_{0030}	$9.0 \pm 0.6 \text{ mm}^{-\frac{1}{2}}$	$2.2 \pm 0.4 \text{ mm}^{-\frac{1}{2}}$

Table 7.1: Measured resonance strengths in 10^{-3} for both working points (ring 1).

The significantly smaller intrinsic resonance excitation at the new working point was crucial for the decision to re-start the machine in 2004 within the new working area. Since the PSB was operated for the first time in this working area, a new compensation scheme had to be established. For rings 1 and 2 this was done as part of this thesis. Resonance driving term measurements were performed for the linear coupling resonance $Q_x - Q_y = 0$, the second order $2Q_y = 9$ and the third order $3Q_y = 13$ resonance. The obtained results were compared to the corresponding resonance measurements for the old working point.

For the sake of completeness the new β functions are presented in Fig. 7.2 and compared to those of the old working point. The vertical β function changes for the new vertical tune. The horizontal β function remains nearly constant.

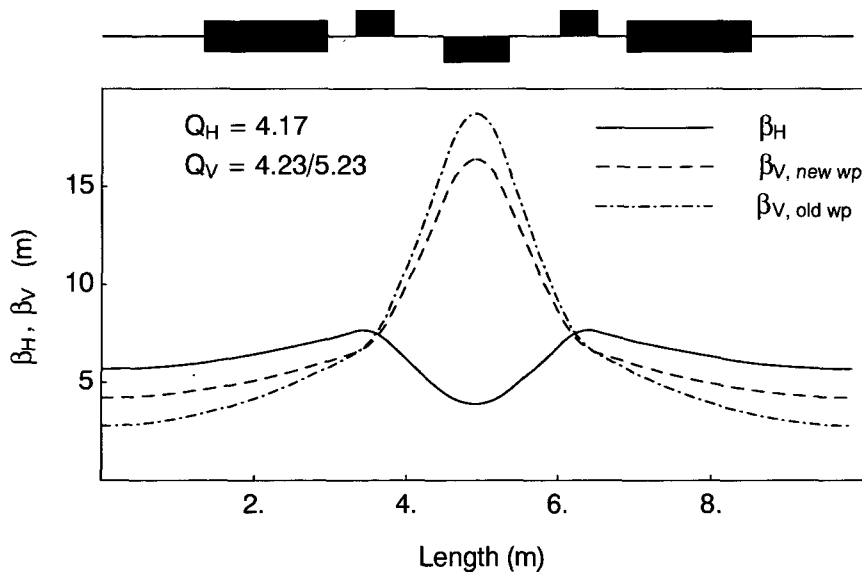


Figure 7.2: Comparison of β functions for old and new working point.

The natural chromaticities are different for the two working points as shown in Table 7.2.

Working point	Q'_x	Q'_y
old	-3.5	-9.3
new	-3.3	-6.7

Table 7.2: Comparison of natural chromaticities for both working points.

One notes that the vertical chromaticity decreased, whereas the horizontal remained nearly constant. Due to the smaller chromaticities, the determination of resonance driving terms is expected to be easier because of the reduced detuning.

7.1 Linear coupling

According to the tune diagram, the relevant linear coupling resonance is $Q_x - Q_y = 0$. Since the phase advance of this resonance is zero, only its strength is important for the compensation. The two skew quadrupole families QSK210L3 and QSK614L3 that were used for the linear coupling compensation at the old working point, cannot be used. The two quadrupoles of each family are powered in series with opposite polarity, therefore the compensation vectors of these elements vanish.

The compensation was therefore done with the zero harmonic skew quadrupole family QSKH0. To find the best compensation settings, the current range of ± 3.0 A was scanned in steps of 0.5 A and the measured resonance strength plotted against the skew quadrupole current (Figs. 7.3 and 7.4). A fit will then yield the proper compensation current. The bare machine excitation is found at $I_{QSKH0} = 0$ A. In both figures, the measurements are shifted compared to simulation, due to the bare machine contribution.

The strengths of the bare machine excitations were calculated to:

- Ring 1: $|h_{1001}| = 1.32 \cdot 10^{-2}$
- Ring 2: $|h_{1001}| = 1.06 \cdot 10^{-2}$

Both values are larger than the linear coupling strength measured at the old working point for $Q_x - Q_y = -1$ ($|h_{1001}| = 0.71 \cdot 10^{-2}$). An interesting fact is that no efficient compensation currents were found. The fits yield $I_{QSKH0} = -0.73$ A for ring 1 and $I_{QSKH0} = +0.30$ A for ring 2 as theoretical compensation values, but only a reduction of roughly 15% in resonance strength was obtained with these settings.

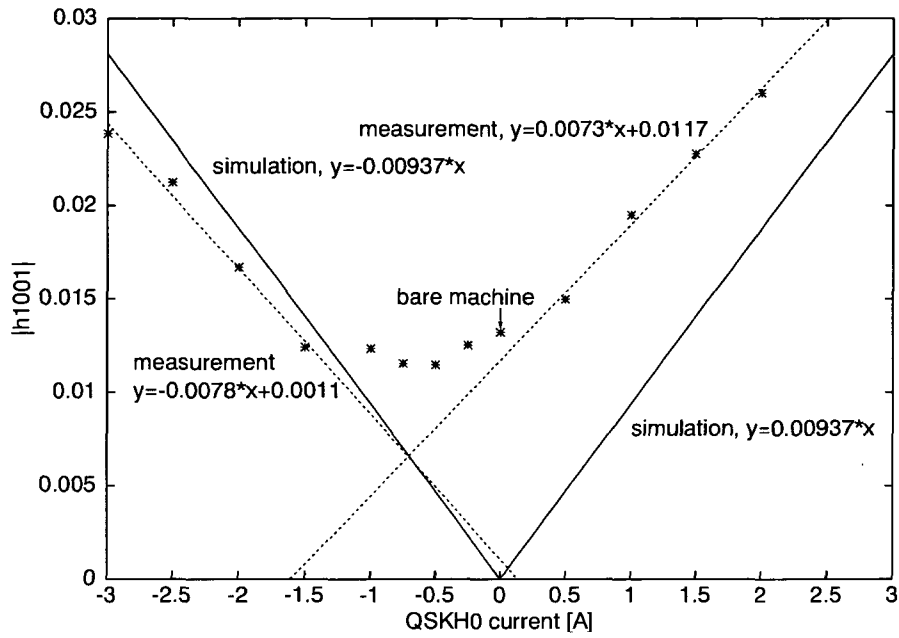


Figure 7.3: Linear coupling strength from measurements (dashed line) and simulations (solid line) over QSKH0 current for ring 1.

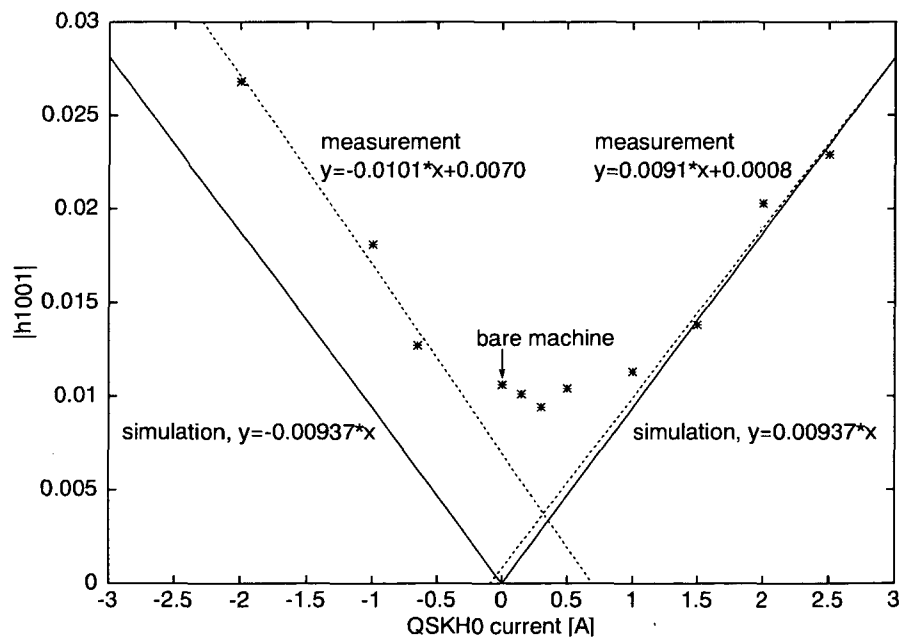


Figure 7.4: Linear coupling strength from measurements (dashed line) and simulations (solid line) over QSKH0 current for ring 2.

To gain a better understanding of the compensation efficiency, simulations were done with a deliberately powered skew quadrupole to model the bare machine excitation. The QSKH0 current was changed in between ± 3 A and the obtained strength plotted against the current (Fig. 7.5). Best compensation was achieved for $I_{QSKH0} = 1.02$ A. For this current the excitation was reduced to 16% of the initial value. A better compensation can not be obtained due to the fact that the measurements and simulations were done with tunes located at a certain distance to the resonance condition ($Q_x \approx 4.19$, $Q_y \approx 4.14$). Hence the resonance phase advance $Q_x - Q_y$ is not zero and a complete compensation with the QSKH0 quadrupoles only is therefore not possible. However, the discrepancy between the measured and simulated compensation efficiency remains to be discussed.

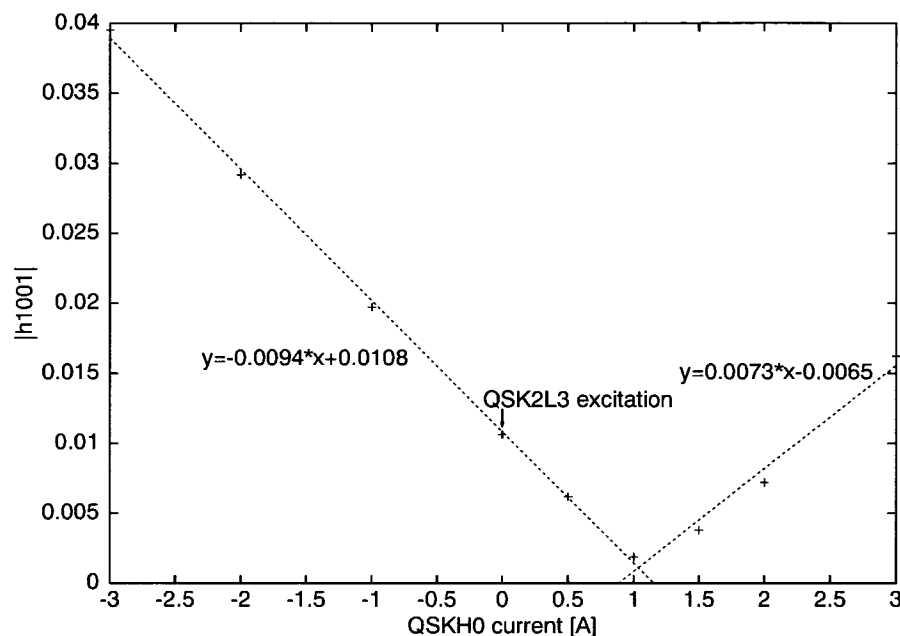


Figure 7.5: Simulation of the bare machine excitation with the skew quadrupole QSK2L3.

7.2 Second order resonance $2Q_y = 9$

Within the new working area the second order resonance $2Q_y = 9$ instead of $2Q_y = 11$ (see Section 5.3) has to be compensated. For the measurements the vertical tune was adjusted close to the resonance condition ($Q_y \approx 4.48$) and chromaticities were not corrected for the reasons already mentioned in Section 5.3.

7.2.1 Measurement of the bare machine excitation

Fig. 7.6 shows the beam intensity in rings 1 and 2 throughout the cycle. The vertical tune was raised 100 ms after injection from 4.46 to 4.54 within 100 ms and then moved back in the same time to 4.46. Thus the resonance was crossed twice. In ring 2 all particles are immediately lost when the tune approaches the resonance, whereas in ring 1 the intensity only reduces to approximately 75% of its initial value.

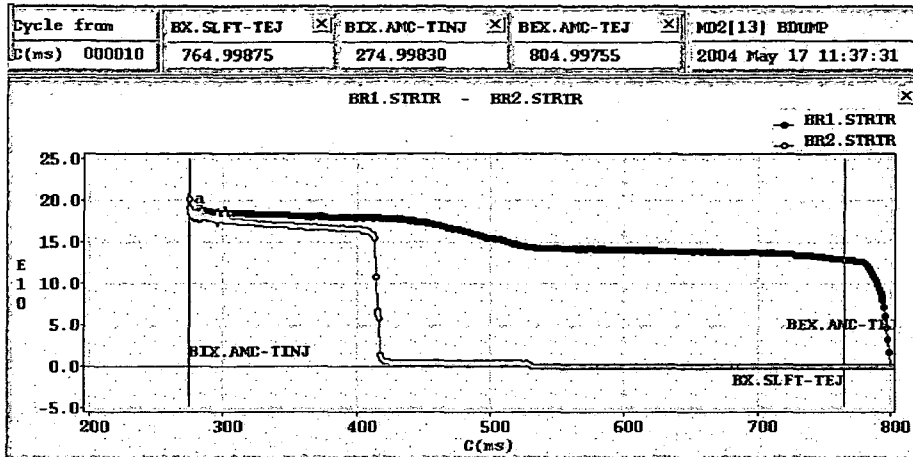


Figure 7.6: Beam intensity in rings 1 (black) and 2 (orange) when crossing the $2Q_y = 9$ resonance.

Resonance strength and phase were calculated with Eqs. 5.17 and 5.18 and yielded for the bare machine excitation:

- Ring 1: $|h_{0020}| = 2.9 \pm 0.2 \cdot 10^{-3}$, $\psi_{0020} = 76.7^\circ \pm 4.3^\circ$
- Ring 2: $|h_{0020}| = 4.9 \pm 0.2 \cdot 10^{-3}$, $\psi_{0020} = 63.8^\circ \pm 12.0^\circ$

The measured excitation of ring 2 is larger than the excitation of ring 1. For both rings, the driving terms are smaller than those observed for the old working point ($|h_{0020}| = 7.0 \pm 0.4 \cdot 10^{-3}$).

7.2.2 Compensation of the resonance

Ring 1

From the bare machine excitation, the compensation currents were calculated to:

- $I_{QNO412L3} = -0.8$ A, $I_{QNO816L3} = -2.5$ A

Fig. 7.7 shows the normalised vertical phase space and the corresponding Fourier spectrum when applying the compensation values. The normalised phase space is quasi free from perturbations and no resonance line was observed any longer in the Fourier spectrum. The beam intensity is shown in Fig. 7.8. Particle losses still exist and are comparable to those obtained for the bare machine. Since no resonance line is visible in the Fourier spectrum, further iterations could not be done. The final compensation currents were obtained by orthogonal search minimising beam losses. For $I_{QNO412L3} = -1.0$ A and $I_{QNO816L3} = -0.9$ A no particle losses occurred (Fig. 7.9).

The local compensation at the PU position is working well (no resonance line in the Fourier spectrum), but no global effect, meaning a reduction in particle losses, is achieved. The signs of the calculated and the final compensation currents are the same, but the discrepancy, especially of the current for the QNO816L3 quadrupole family is not evident.

Table 7.3 compares the calculated and the final compensation currents.

	$I_{QNO412L3}$	$I_{QNO816L3}$
calculated currents	-0.8 A	-2.5 A
final currents	-1.0 A	-0.9 A

Table 7.3: Comparison of the calculated and the final compensation currents.

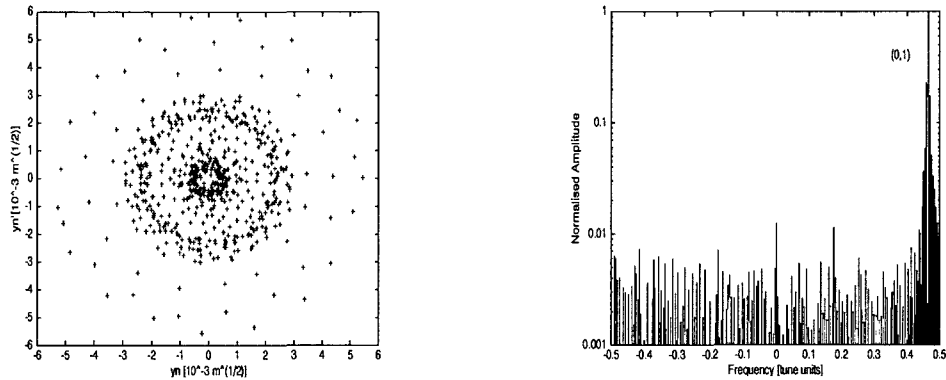


Figure 7.7: Normalised phase space and corresponding Fourier spectrum in case of compensation ($I_{QNO412L3} = -0.8$ A, $I_{QNO816L3} = -2.5$ A).

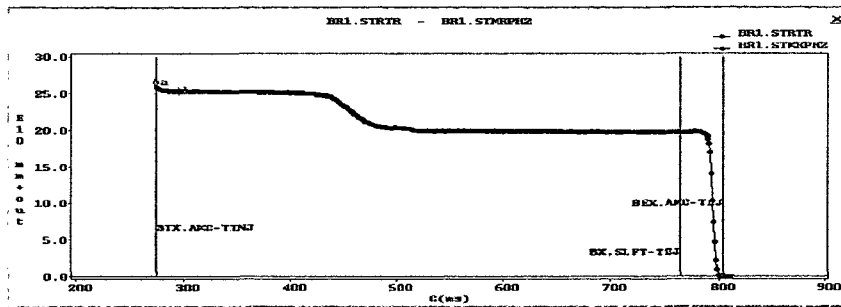


Figure 7.8: Beam intensity when the quadrupoles were powered with the calculated compensation currents ($I_{QNO412L3} = -0.8$ A, $I_{QNO816L3} = -2.5$ A).

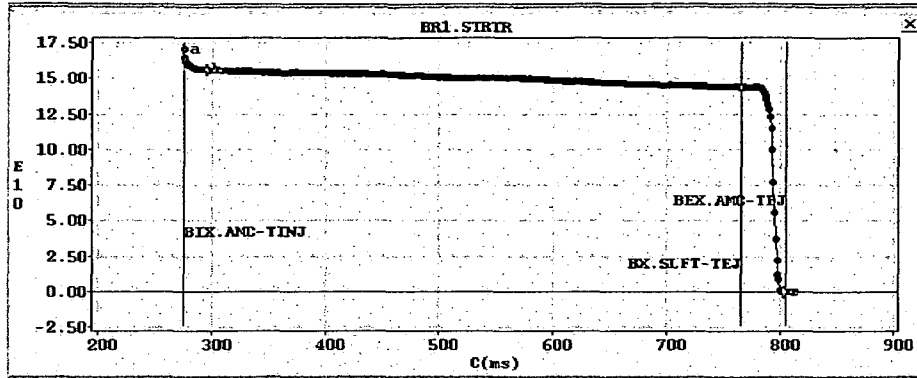


Figure 7.9: Beam intensity for the efficient compensation currents ($I_{QNO412L3} = -1.0$ A, $I_{QNO816L3} = -0.9$ A).

Ring 2

For ring 2 the following compensation currents were calculated and applied:

- $I_{QNO412L3} = -3.4$ A, $I_{QNO816L3} = -3.1$ A

Fig. 7.10 shows the beam intensity when the above mentioned currents were used. The resonance is crossed in the same way as for the bare machine. A steady intensity drop over the whole period is observed. No additional losses are present while the resonance is crossed twice. The compensation settings work well and the resonance strength was reduced down to $|h_{0020}| = 1.0 \pm 0.1 \cdot 10^{-3}$ or 20% of its initial value.

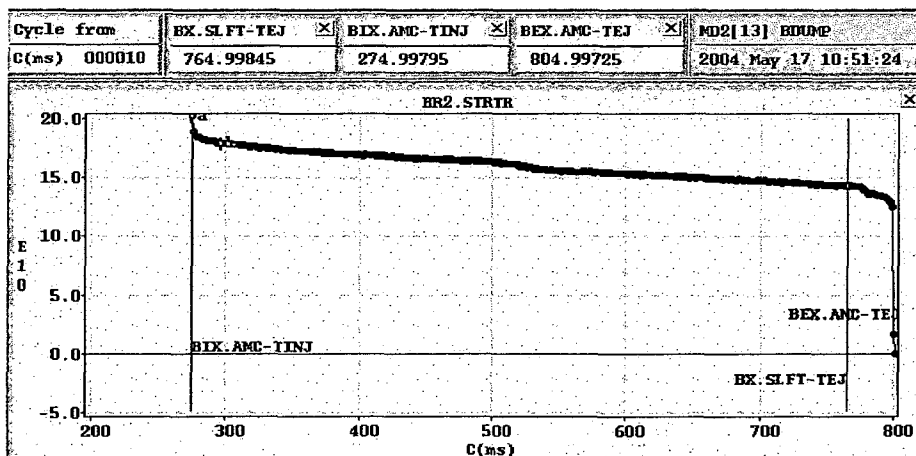


Figure 7.10: Beam intensity when the quadrupoles were powered with the calculated compensation currents.

It is important to point out that the measured resonance strength in both rings for the new working point is smaller than the one obtained for the old working point.

Table 7.4 summarises the bare machine excitation and the compensation currents for the h_{0020} resonance driving term.

	Old wp, ring 1	New wp, ring 1	New wp, ring 2
Strength	$7.0 \pm 0.4 \cdot 10^{-3}$	$2.9 \pm 0.2 \cdot 10^{-3}$	$4.9 \pm 0.2 \cdot 10^{-3}$
I_{QNO412L3}	+6.3 A	-1.0 A	-3.4 A
I_{QNO816L3}	-2.8 A	-0.9 A	-3.1 A

Table 7.4: Resonance strengths and efficient compensation currents for the old and new working point.

7.3 Third order resonance $3Q_y = 13$

The main motivation to change the working point was to avoid the $3Q_y = 16$ systematic resonance. Now the skew sextupole resonance $3Q_y = 13$ has to be considered. For the measurements the vertical tune was adjusted close to the resonance condition ($Q_y \approx 4.35$) and the vertical chromaticity was corrected to zero.

7.3.1 Measurement of the bare machine excitation

Fig. 7.11 shows the beam intensity in rings 1 and 2 throughout the cycle. The vertical tune was slowly changed from 4.37 to 4.30 within some 100 ms. One notes that the beam intensity remains stable for ring 2, whereas 20% of the particles are lost in ring 1.

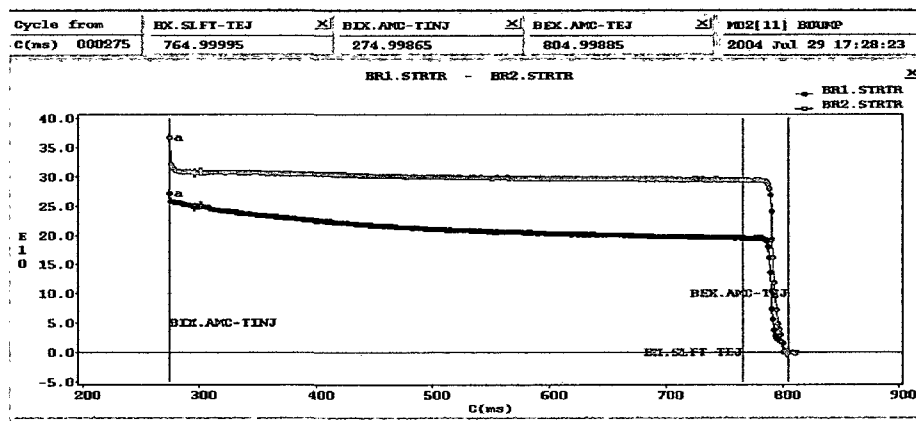


Figure 7.11: Beam intensity for rings 1 (black line) and 2 (orange line) when crossing the $3Q_y = 13$ resonance.

Only for ring 1 the corresponding (0,-2) resonance line was identified in the Fourier spectra. The strength and phase were calculated with Eqs. 6.3 and 6.4 and yielded for the bare machine excitation:

- $|h_{0030}| = 2.2 \pm 0.4 \cdot 10^{-3} \text{ mm}^{-\frac{1}{2}}, \psi_{0030} = 242.1^\circ \pm 17.3^\circ$

The measured excitation corresponds to approximately 25% of the one found for the old working point and therefore underlines the advantage of the new working area.

7.3.2 Compensation of the resonance

Only a single skew sextupole, located in a low β_y region, was used to compensate the resonance. From the analysis the current was calculated to:

$$I_{XSK9L1} = +31.0A$$

Fig. 7.12 shows the beam intensity in case of compensation for ring 1. Ring 2 is uncorrected. No particles are lost in both rings.

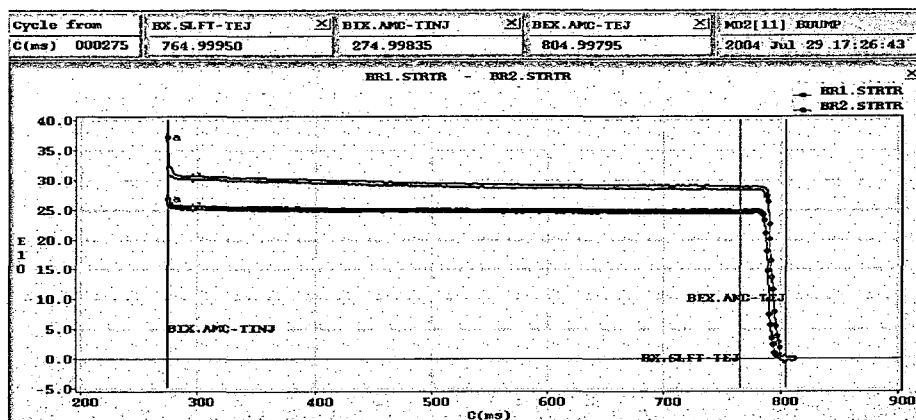


Figure 7.12: Beam intensity for rings 1 and 2. The $3Q_y = 13$ resonance has to be compensated only for ring 1.

Table 7.5 summarises the bare machine excitation and the calculated compensation currents for the h_{0030} resonance driving term for the old and the new working point.

	Old wp, ring 1	New wp, ring 1	New wp, ring 2
Strength [$\text{mm}^{-1/2}$]	$9.0 \pm 0.6 \cdot 10^{-3}$	$2.2 \pm 0.4 \cdot 10^{-3}$	no line found
I_{XSK2L4}	-29.3 A	0.0 A	—
I_{XSK9L1}	+15.3 A	+31.0 A	—

Table 7.5: Resonance strengths and compensation currents for the old and new working point.

7.4 Conclusions for the new working point

The obtained results for the new working point confirm clearly that from the resonance excitation point of view, the new working point is preferable to the one used so far in standard operation. The strengths of the most relevant resonance driving terms (h_{0020} and h_{0030}) are smaller in the new working area. Furthermore, all operational PSB beams showed at least identical performance in terms of beam quality (intensity, emittance) at the new working point.

Chapter 8

Conclusions

Although there is a wealth of theoretical knowledge on resonance driving terms backed by proof-of-principle experiments, the measurement and compensation of betatron resonances based on FFT analysis of multi-turn beam position data still remained to be demonstrated as a tool for standard operation. The thesis has made an original contribution to the field by implementing this method for an existing machine and by covering all aspects of resonance analysis and compensation relevant for routine operation.

Following a brief introduction to accelerator physics, the thesis gives an overview on the existing theory for resonance driving term analysis. Then all aspects of practical implementation of a measurement system, especially covering the available hardware and the specific operation conditions of the PS Booster are discussed in detail. This analysis was the basis for the specification and implementation of a turn-by-turn beam position measurement system including data treatment and FFT analysis, that served as basic tool for all measurements performed within the thesis work.

During a first measurement campaign in 2003, all second and third order resonances relevant for the operation were analysed for ring 1 of the PS Booster. Strength and phase of the bare machine driving terms for these resonances were evaluated, the effect of compensation multipoles was measured and compared to simulations. With the knowledge of the bare machine driving terms, compensation settings for all resonances were calculated and compared to the existing compensation scheme. Excellent agreement was found in all cases, on the one hand confirming the quality of the existing scheme and, on the other hand, underlining the validity and correctness of the new method.

The system allows the fast determination of driving terms and its usefulness was demonstrated during a short dedicated measurement campaign where a new, alternative working point was tested. It was found that the driving terms are explicitly smaller in this area of the tune diagram than for the standard working point. The obtained results have significantly influenced the decision to restart the PS Booster in 2004 with the new working point. The final part of the thesis was to establish the resonance compensation scheme in rings 1 and 2 for this new working point.

Bibliography

- [1] J. Bengtsson, *Non-linear transverse dynamics for storage rings with application to the low-energy antiproton ring(LEAR) at CERN*, CERN 88-05, 1988.
- [2] J. Rossbach, P. Schmüser, *Basic course on accelerator physics*, proceedings of CAS, CERN 94-01, Vol.I.
- [3] Courant E.D., Snyder H.S., *Theory of the Alternating Gradient Synchrotron*, Ann.Phys. (USA) 3, 1958.
- [4] P.J. Bryant, K. Johnsen, *The Principles of Circular Accelerators and Storage Rings*, 1993.
- [5] D. A. Edwards, M. J. Syphers, *An Introduction to the Physics of High Energy Accelerators*, SSC Laboratory Dallas, Texas, 1993.
- [6] G. Guignard, *A General Treatment of Resonances in Accelerators*, CERN, Geneva, 1978.
- [7] O. Bruning, *Non-linear Imperfections*, CAS Zeuthen, 2003.
- [8] A. Bazzani, E. Todesco, G. Turchetti, *A Normal Form Approach to the Theory of Nonlinear Betatronic Motion*, CERN 94-02.
- [9] R. Bartolini, F. Schmidt, *SUSSIX: A Computer Code for Frequency Analysis of Non-linear Betatron Motion*, CERN/SL/Note 98-017 (AP), update December 1999.
- [10] J. Bengtsson, J. Irwin, *Analytical Calculations of Smear and Tune Shift*, Superconducting Super Collider Laboratory, Dallas, SSC-232, 1990.
- [11] É. Forest, *Beam dynamics: A New Attitude and Framework*, Harwood Academic, pp. 168-171, 1998.
- [12] K. Schindl, *Space Charge*, CERN/PS 99-012 (DI)
- [13] K. Schindl, *Simultaneous dynamic compensation of stopbands and multipurpose location of correction lenses in the CERN PS Booster*, IEEE Transaction on Nuclear Science, Vol. NS-26, No. 3, June 1979.
- [14] K. Schindl, E. Troianov *Experiments on third-order resonances in the PSB*, CERN/PS/BR 78-16, 7 August 1978.
- [15] E. Wilson, *Non-linearities and resonances*, proceedings of CAS, CERN 94-01, Vol.I.
- [16] R. Bartolini, F. Schmidt, *Normal Form via tracking or Beam Data*, Part. Accel. 59, pp. 93-106, 1998.
- [17] M. E. Angoletta, A.-S. Müller, *A Multi-turn Measurement System for the CERN PS*, CERN/PS 2002-030 (AE).
- [18] M. E. Angoletta, *CaP User's manual*, October 2001.
- [19] F. Schmidt, *SixTrack, User's Reference Manual*, CERN/SL/94-56 (AP), Update March 2000.

- [20] R. Tomás, *Direct Measurements of Resonance Driving Terms in the Super Proton Synchrotron (SPS) of CERN using Beam Position Monitors*, Thesis, 01.2003.
- [21] P. J. Bryant, *A simple theory for weak betatron coupling*, proceedings of CAS, CERN 94-01, Vol.I.
- [22] J. Laskar, C. Froeschlé, A. Celletti, *The measure of chaos by the numerical analysis of the fundamental frequencies. Application to the standard mapping*, Physica D 56, pp. 253-269, 1992.
- [23] M. Q. Barton, *Beam extraction from synchrotrons*, Proceedings VIIIth Int. Conference on High Energy Accelerators, p.85-8, Geneva, 1971.
- [24] C. Carli, M. Chanel, G.Cyvoc, *Other Working Points for the PSB*, presentation at PPC meeting, CERN, 2001.
- [25] M. Benedikt, C.Carli, M. Chanel, F. Schmidt, P. Urschütz, *Betatron Resonance Studies at the CERN PS Booster by Harmonic Analysis of Turn-by-turn Beam Position Data*, EPAC 2004, Lucerne, Switzerland.
- [26] P. Urschütz, *Measurement and Compensation of Second and Third Order Resonances at the CERN PS Booster*, EPAC 2004, Lucerne, Switzerland.

Curriculum Vitae

Peter Urschütz

PERSONAL DATA

Name: Peter Urschütz
Date of Birth: 22 April 1975
Nationality: Austrian
Marital Status: Single
Military service: completed

CONTACT ADDRESS

Zangerlestr. 18
1230 Wien
Austria
email: peter.urschuetz@cern.ch

CURRENT POSITION

Oct. 2004 - present: Fellow (post doctoral position) at CERN, Accelerator & Beams
Department

EDUCATION

expected in Oct. 2004: Ph.D. in Physics at the Vienna University of Technology
Nov. 2001 - Sept. 2004: Doctoral Student at CERN, AB Department,
Thesis topic: *Measurement and Compensation of Betatron Resonances
at the CERN PS Booster Synchrotron.*
June 2000: Degree of Dipl. Ing. (Master of Science) in Physics with distinction,
Thesis topic: *Dosimetric Quality Assurance of a three dimensional
treatment Planning System (Helax-TMS): Actual Investigation and
Proposal for a QM-Strategy.*
1994 - 2000: Vienna University of Technology, Subject area: Technical Physics
1989 - 1994: Federal Secondary College of Engineering, Mödling, Austria
Subject area: Industrial Engineering; Graduation with distinction
1985 - 1989: Grammar School, Perchtoldsdorf, Austria

PART-TIME WORK

Jan. 1998 - Oct. 2000: The Austrian Sports Net, Inc., Vienna, Department of sports reporting
August 1998: Siemens, Inc., Vienna, Department of medical technology
August 1997: Siemens, Inc., Vienna, Department of software development
August 1996: Siemens, Inc., Vienna, Department of software development
August 1995: Hilti, Ltd., Vienna, Department of special spare parts production
August 1994: Hilti, Ltd., Vienna, Department of special spare parts production
July 1992: Plasser & Theurer, Ltd., Vienna, Department of technical drawings
July 1991: Hilti, Ltd., Vienna, Department of special spare parts production
July 1990: Hilti, Ltd., Vienna, Department of special spare parts production

STAYS ABROAD

July - Aug. 2000: Exchange program (IAESTE), State University of Campinas (SP), Brazil,
Chemistry Institute

LANGUAGES

German: native language
English: excellent
French: good

COMPUTER SKILLS

Operating Systems: MS Windows, Unix
Software and Languages: MS Office, Mathematica, AutoCAD, LabView, MAD, SixTrack,
Latex, html, basic knowledge in Fortran, C/C++

HOBBIES AND INTERESTS

football, skiing, climbing, hiking, running, traveling

LIST OF PUBLICATIONS

- P. Urschütz, *Measurement and Compensation of Betatron Resonances at the CERN PS Booster*, Ph.D. thesis, September 2004.
- P. Urschütz, *Measurement and Compensation of Second and Third Order Resonances at the CERN PS Booster*, EPAC 2004, Lucerne, Switzerland.
- M. Benedikt, C. Carli, M. Chanel, F. Schmidt, P. Urschütz, *Betatron Resonance Studies at the CERN PS Booster by Harmonic Analysis of Turn-by-turn Data*, EPAC 2004, Lucerne, Switzerland.
- M. Benedikt, A. Blas, C. Carli, M. Chanel, H. Fiebiger, A. Findlay, K. Hanke, J. L. Sanchez-Alvarez, J. Tan, P. Urschütz, *Study of a New Working Point for the CERN PS Booster*, AB-Note-2004-??? OP, to be published.
- P. Urschütz, *Betatron Resonance Studies at the PS Booster by Harmonic Analysis of Turn-by-turn Beam Position Data*, CERN, AB Note-2004-024 OP.
- P. Urschütz, U. Wolff, H. Aiginger, R. Pötter, *Dosimetric Quality Assurance of a three dimensional Treatment Planning System (Helax-TMS): Actual Investigation and Proposal for a QM-Strategy*, Abstract and poster at ÖPG (Austrian Physical Society) - Congress, Graz, Austria, 2000.
- P. Urschütz, *Dosimetrische Qualitätssicherung an einem 3D Planungssystem (Helax-TMS)*, Diploma thesis, May 2000.